Hot forging of the nickel-base superalloy ATI 718Plus®

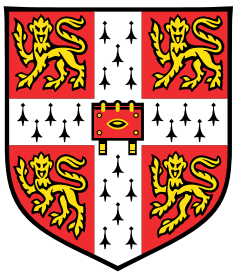

Christiane Kienl

Department of Material Science and Metallurgy
University of Cambridge

This dissertation is submitted for the degree of
Doctor of Philosophy

Emmanuel College August 2019

Declaration

This dissertation is submitted for the degree of Doctor of Philosophy at the University of Cambridge. It describes the research carried out in the Department of Materials Science and Metallurgy between October 2015 and October 2019 under the supervision of Professor Catherine M.F. Rae. Except where reference is made to the work of others, the contents of this dissertation are original and have not been the result of collaboration. No part of the work described here has been submitted for the purpose of gaining academic qualification at this or any other institute of higher learning. This dissertation does not exceed 60,000 words in length and has fewer than 150 figures.

Parts of this dissertation have been published in:
C. Kienl, A. Casanova, O. M. Messé, C Argyrakis, C. M. F. Rae, Characterization of the initial stages of dynamic recrystallization in ATI 718Plus®. *Proceedings of the 9th International Symposium on Superalloy 718 and Derivatives: Energy, Aerospace and Industrial Applications*, 405-420, 2018.

Christiane Kienl
August 2019

Acknowledgements

This thesis was generously funded by the EPSRC and Rolls-Royce plc. who made the work on this topic possible. I would like to thank my supervisor Cathie Rae for her patience with my impatience and making me question common beliefs. Countless hours of lively and silent discussions have formed this thesis and me as a person. Thanks to her I have now a thing for TEMs. On the part of Rolls-Royce I am beholden to my industrial supervisor Christos Argyrakis for the uncomplicated and supportive collaboration.

I am glad having had a number of crafty people around me to swiftly fix microscopes, computers and broken hearts. Hon Tong Pang and Sue Rhodes were the ones who kept our lab running and were continuously teaching me the black magic of sample preparation. Thanks to Simon Griggs and Chris Dolan for handling blown filaments and drifting samples. I also want to thank the workshop at the Department of Material Science and Metallurgy who machined my samples whenever needed. Big thanks to the members past and present of the Rolls-Royce UTC in Cambridge who helped me from technical questions to where to find the best pub. Without them, conference dinners would have been less melodic and guacamole not as eyeopening. I am also tremendously grateful for a special set of people who relentlessly ploughed their way through this thesis irrespective of the jungle of words they were facing.

I am thankful for the support from Emmanuel college, my tutor and the lilos in the Emma pool making my stay here the best it could be. My time in Cambridge would have been different without the friendships I formed on and off the Cam.

Ein spezieller Dank gebührt meinen Eltern, welche nie versuchten, mir meine Entscheidungen auszureden - ungeachtet dessen, wie absurd sie auch erschienen/waren.

Finally, a massive thank you to the one person who kept me going.

Abstract

Nickel-base superalloys are widely applied in the hot sections of aero engines due to their high temperature capabilities and excellent mechanical properties. For turbine discs, polycrystalline Ni-base superalloys are used where they experience temperatures up to 700°C and stresses as high as 1000 MPa. The manufacturing process, especially the forging and heat treatment, plays a pivotal role towards achieving the final microstructure and mechanical properties needed to withstand this harsh environment.

ATI® 718Plus™ (hereafter 718Plus) is a polycrystalline multi-phase strengthened nickel-base superalloy for turbine disc applications in aero engines. 718Plus was designed to fill in the gap between IN718 and Waspaloy. Its main strengthening phase is γ' but it was also found to precipitate the hexagonal η phase. This alloy is used to study the microstructural changes due to recrystallisation and deformation occurring during forging. The body of work includes the testing and characterisation of two distinct microstructures, one being γ-γ' and the other γ-η.

High temperature compression tests on cylindrical samples were performed in the temperature range between 850 and 1025°C for the γ-γ' and 950 to 975°C for the γ-η microstructure. Final strains of the tests varied from 0.4 to 1.2 and strain rates between 0.01 to $1s^{-1}$. To analyse the material's behaviour during post-deformation recrystallisation (meta-dynamic recrystallisation), a second set of samples was kept in the furnace for 120 s after the compression at high temperature before they were water-quenched. The microstructural changes were investigated using both scanning electron microscope (SEM) and transmission electron microscope (TEM) analysis.

Dynamic and meta-dynamic recrystallisation were analysed with respect to their sensitivity on the testing parameters. An increase in recrystallised fraction with strain rate was found, which is in line with reported values on 718Plus but in contrast to similar nickel-base superalloys such as IN718 or Waspaloy. A detailed analysis of TEM specimens revealed that the higher fraction in recrystallised area was due to meta-dynamic recrystallisation during the sample transfer time between deformation and quench. In the γ-η microstructure the same mechanism could be observed. In addition, lamellar packets of η phase were found to inhibit recrystallisation and promote a narrower grain size distribution.

The flow curves together with the recrystallised fraction were used to develop a basic material model for simulating the forging process. It could be shown, that the employed underlying framework was sensitive to minor fluctuations in the input parameters.

The deformation mechanisms of 718Plus at interrupted high temperature compression tests were analysed by an extensive TEM study. A large number of grains formed deformation twins. This mechanism is commonly found in alloys with a low stacking fault energy at low temperatures and/or high strain rates. Initial stages of twinning could be captured and allowed a detailed analysis of the underlying processes. In the γ-η microstructure the deformation characteristics of η were studied. η phase accommodated for the strain by breakage and realignment and also by severe bending.

Table of contents

List of figures

List of tables

Nomenclature

Roman Symbols

a	Lattice parameter [m]
ccp	cubic close-packed
APB	Anti-phase boundary
b	Burgers vector [m]
BF	Bright field
BSE	Back-scattered electrons
$cDRX$	Continuous dynamic recrystallisation
$cSRX$	Continuous static recrystallisation
$dDRX$	Discontinuous dynamic recrystallisation
DRV	Dynamic recovery
DRX	Dynamic recrystallisation
$dSRX$	Discontinuous static recrystallisation
$EBSD$	Electron back-scatter diffraction
EDX	Energy dispersive X-ray spectroscopy
FEM	Finite element modelling
G	Shear modulus [GPa]
$gDRX$	Geometric dynamic recrystallisation

HAADF High angle annular dark field

HAGB High angle grain boundary

heRX Heteroepitaxial recrystallisation

IPF Inverse pole figure

LAGB Low angle grain boundary

KAM Kernel average misorientation

MDRX Meta-dynamic recrystallisation

n Avrami coefficient

PSN Particle stimulated nucleation

Q Activation energy [kJ mol^{-1}]

R Universal gas constant [J mol^{-1} K^{-1}]

SEI Secondary electron imaging

SFE Stacking fault energy, γ_{SFE} [mJ m^{-2}]

SIBM Strain induced boundary migration

SRV Static recovery

SRX Static recrystallisation

STEM Scanning transmission electron microscopy

T Temperature [K]

T_m Melting temperature [K]

t Time [s]

TEM Transmission electron microscopy

TKD Transmission Kikuchi diffraction

R Universal gas constant [J mol^{-1} K^{-1}]

WBDF Weak beam dark field

X_{RX} Recrystallised fraction [%]

Z Zener-Hollomon parameter [s^{-1}]

Greek Symbols

$\dot{\varepsilon}$ Strain rate [s^{-1}]

ε Strain [-]

$\overline{\Theta_g}$ Mean orientation of grain g [°]

Θ_{gi} Orientation of point i in grain g [°]

Chapter 1

Introduction

1.1 The jet engine

The development of aeroplanes have increased human mobility significantly. This rapid uplift has been enabled by the advent of commercially successful jet engines. To keep aircrafts as a competitive transportation option, the engines are subject to demanding new design restrictions. The growing environmental awareness as well as the increase in fuel prices demands more efficient engines.

The efficiency of a jet engine is determined by its combustion temperature and therefore the temperature in the rear part of the engine, the turbine. A diagram of a jet engine from Rolls-Royce plc. is presented in Figure 1.1. The higher the turbine entry temperature (TET) the more economical and efficient the overall process. With the increasing temperature the overall pressure ratio rises, leading to a faster shaft rotation and higher stresses on the turbine parts. With these key requirements in mind the appropriate materials should have high temperature stability along with good stress resistance.

Nickel, titanium alloys as well as steel are all used in the jet engine but, for turbine components such as blades or discs, nickel-base superalloys are the material of choice owing to their excellent high temperature properties.

1.1.1 The turbine disc

The turbine disc connects the blades and the engine shaft. The blades are either joined directly onto the rim or fastened via a tongue and groove joint. Whereas turbine blades are exposed to the hot gas stream with temperatures approaching 1800°C the turbine disc faces very different but equally challenging conditions. The temperature at the outer part of the disc approaches ~650°C during service. Towards the bore the temperature reduces.

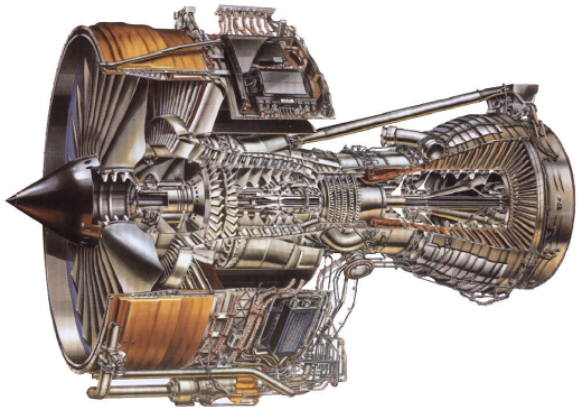

Fig. 1.1 Rolls-Royce Trent 800 jet engine [1]

The stresses reach their maximum at the inner diameter and are as high as 1000 MPa [2]. Figure 1.2 presents temperature and stress variation over a simplified disc cross-section. In line with the varying conditions along the radius different failure mechanisms will occur. While the rim is exposed to creep and oxidation the bore needs to withstand low cycle fatigue and very high stresses. Hence, the demands on the microstructure range from large grains in the creep endangered zones to a fine grain size in the area exposed to low cycle fatigue. These risks need to be managed appropriately as the disc is one of the most critical parts of the engine and a failure is a potential hazard to the plane and passengers. Controlling the microstructural evolution during processing of the turbine disc is key.

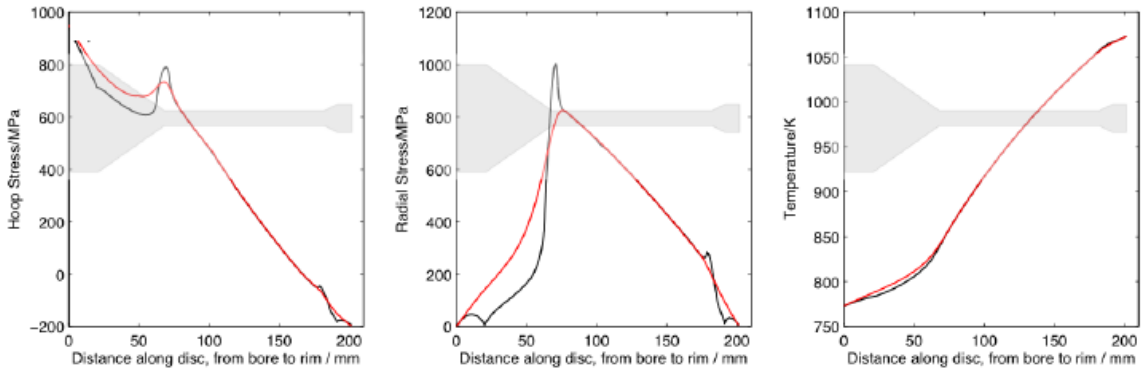

Fig. 1.2 Conditions turbine disc: hoop, radial stress and temperature [3]

1.1.2 Forging and heat treatment

The forging steps bring the material near to the net shape of the final component. For the production of a complex contour such as a turbine disc several stages are required.

The cavities of the dies need to be properly filled to guarantee a defect free component. Forging does not only define the shape of the component but also dictates the microstructure of the turbine disc. Temperature, strain and strain rate directly influence grain size and precipitation kinetics. During the forging of a nickel-base superalloy recrystallisation occurs, a phenomenon by which new grains grow to replace deformed ones. The final microstructure of the component in the engine is primarily formed during forging.

Following the forging, a heat treatment should (i) release stresses induced during manufacturing and (ii) trigger precipitation. Nickel-base superalloys show a variety of precipitates with different solvus temperatures. Depending on the forging temperature some types of precipitates can dissolve but are necessary for the strength of the material during service. Hence, subsequent heat treatments are needed to initiate precipitation and tailor their size and shape to give the optimum balance of mechanical properties.

1.2 Thesis outline

The aim of this thesis is the analysis of microstructural changes of a nickel-base superalloy during deformation. The focus will be on dynamic recrystallisation of a single- and two-phase microstructure. In addition, deformation mechanisms in the γ matrix as well as the secondary η phase will be studied.

The thesis is divided into six parts described as follows. The literature review addresses the material used and recent findings on dynamic recrystallisation in materials with low stacking fault energies. Chapter 3 describes the techniques used to analyse the samples from compression tests. Preparation routines as well as follow-up analyses are described. The general recrystallisation behaviour of the material is investigated in Chapter 4. The single and two-phase microstructure variants are characterised separately in terms of their response to the testing parameters. In the following Chapter 5 the results from the mechanical testing are evaluated, focusing on the flow curves obtained. This chapter also includes a section on the development of an empirical model for predicting recrystallisation in ATI® 718Plus™. A detailed study of the deformation mechanisms occurring during high temperature compression testing is presented in Chapter 6. The mechanisms are analysed in both the matrix as well as the precipitates. The final chapter includes a summary and discussion of the findings along with an outlook for future research.

Chapter 2

Literature review

2.1 Review on nickel-base superalloys

Nickel-base superalloys are the material of choice for high temperature applications. Nickel is used as a base material because of its crystallographic structure and benign interaction with other alloying elements. The cubic close-packed (ccp) crystal structure has tough and ductile properties. A further benefit of nickel is the low diffusion rate of the ccp structure. Thereby, the resistance against thermally activated creep is increased. An advantage of using nickel rather than iron is the absence of a phase transformation up to its melting point. Hence, thermal expansion or contraction, which attend such crystallographic changes, do not need to be considered during the design process. The alloying elements, together with nickel, form a system of a disordered matrix, γ, containing at least one ordered intermetallic phase (e.g. γ', γ'').

The above-mentioned microstructural stability combined with moderate cost and density explains the leading role of nickel as solvent for components in aero engines [2].

Strengthening phases

The γ' phase has an ordered $L1_2$ structure with the chemical composition Ni_3[Al,Nb,Ti]. γ' and γ form a coherent interface with an unstrained misfit defined by the alloy composition. Numerous single- and polycrystalline nickel-base superalloys rely on γ' as their primary strengthening phase. The second ordered phase which can form in nickel-base superalloys is γ'' which has a body centred tetragonal structure ($D0_{22}$, Ni_3[Nb,Ta]). This phase is known for an improved strengthening over γ'. The strengthening effect was attributed to higher shear stresses on the dislocations because of a coherency effect of the tetragonal nature of the particle [4]. However, γ'' is a meta-stable phase which transforms to δ phase at temperatures above ~650°C [2].

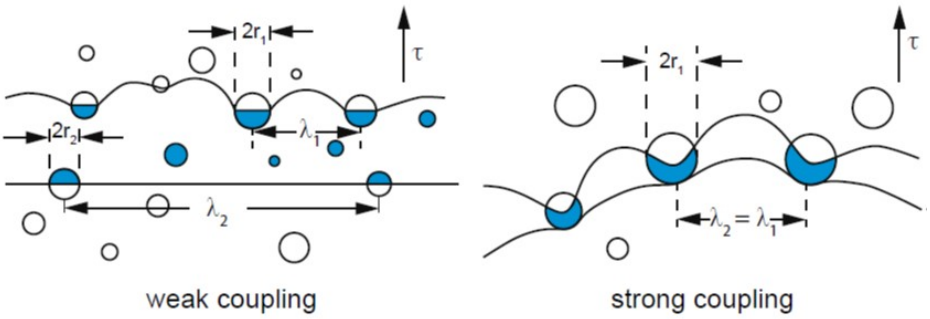

Fig. 2.1 Weak and strong coupling of dislocation pairs in a γ-γ' microstructure [2]

The γ matrix with the ordered precipitates give the material its characteristic strength and toughness at high temperatures.

Deformation mechanisms in nickel-base superalloys

The movement of dislocations guides the deformation of metals. A ccp crystal structure contains of four closed packed planes $\{111\}$ with six closed packed directions $\langle 110\rangle$. As each of these directions occurs on two planes the total number of slip systems sums up to 12. Dislocations can glide on the closed packed planes. If the shear stress on the dislocation exceeds its Peierls stress it starts moving through the crystal. For a given direction of impact on a randomly oriented crystal the individual stress on each plane differs. The Schmid factor determines the propensity of slip to occur on a certain plane.

The interaction between dislocations and the ordered phases is responsible for the strength in nickel-base superalloys. When a matrix dislocation, a/2$\langle\bar{1}10\rangle\{111\}$, enters a γ' precipitate it causes an anti phase boundary (APB) by disturbing the ordering of aluminium and nickel atoms. To remove the energy penalty due to the APB a second dislocation of the same Burgers vector is required to restore the atomic arrangement. The paired dislocation configuration is termed superdislocation with the each dislocation termed as superpartials [2]. For high γ' fractions the dislocations are strongly-coupled characterised by a small distance between them compared to the particle radius, whereas weak coupling occurs for a lower γ' fraction and the individual superpartials can even be in separate precipitates (see Figure 2.1). With increasing particle size the cutting mechanism transforms from weak to strong coupling and finally changes to Orowan looping. The optimal strength is achieved when weak coupling is superseded by strong coupling. Hence, a small particle size is beneficial where the dislocation spacing in the γ' is similar to half the diameter of the precipitates.

The mobile dislocations in γ are a/2$\langle\bar{1}10\rangle\{111\}$. The perfect a/2$\langle\bar{1}10\rangle\{111\}$ dislocations in ccp can reduce their energy by splitting into partial dislocations of type a/6$\langle\bar{1}2\bar{1}\rangle\{111\}$. Between the leading and trailing partial a stacking fault is formed and its energy penalty

depends on material and temperature. For low stacking fault energy (SFE) metals such as nickel-base superalloys the distance between the partials is larger than for high SFE materials. However, for a screw dislocation to cross-slip onto another plane the partials must rejoin and form a perfect matrix dislocation.

Apart from dislocation glide and cross-slip, an edge-type dislocation can climb onto a parallel slip plane to overcome obstacles. The diffusion of vacancies enables a dislocation to climb and continue its path on a plane without an impediment. As it is a diffusion based mechanism, climb is enhanced at higher temperatures.

Besides precipitates, grain size plays an important role in the overall performance of the material. Low cycle fatigue resistance at elevated temperatures is improved by a small and evenly distributed grain size distribution [5]. As η-phase pins the grain boundaries, hence determining the grain size, it is important to control its growth during forging and heat treatment.

Classification

There exist several approaches to classify nickel-base superalloys which can be based on their manufacturing process or microstructure. Alloys for turbine disc applications can be produced either by a cast-and-wrought routine or via powder processing. Waspaloy and Inconel 718 (hereafter IN718) are representatives of the first group whereas Udimet 720Li is a powder metallurgically produced alloy which can also be manufactured in a cast-and-wrought routine. On a microstructural scale, nickel-base superalloys can be distinguished by precipitating solely γ' or multiple phases. Considering only cast-and-wrought alloys, Waspaloy is an example for the γ/γ' group while IN718 is a representative of multi-phase strengthened alloys.

IN718 is a multi-phase (γ'' and δ) hardening alloy characterised by good hot forming properties and low costs. The main strengthening phase γ'' defines the maximum operating temperature of 649°C as it overages quickly and transforms into δ [6, 7]. Due to the morphology of the incoherent δ phase, strength and creep properties of IN718 drop rapidly. Waspaloy on the other hand is strengthened by γ' solely, and therefore shows enhanced temperature stability over IN718. The disadvantage of the composition of Waspaloy are the poor processability and high costs of the raw material.

Alloy ATI® 718Plus™ should fill the gap between the nickel-iron-base IN718 and the nickel-base Waspaloy. ATI® 718Plus™ (hereafter 718Plus) is a polycrystalline multi-phase strengthened nickel-base wrought alloy developed by ATI Speciality Materials, Ltd. USA [6]. Based on IN718 it was designed for operating temperatures of 704°C, 55°C above IN718 [8]. Its main strengthening phase γ' has an improved temperature stability over γ''. Due to the addition of niobium, 718Plus shows a superior behaviour during welding and forming to

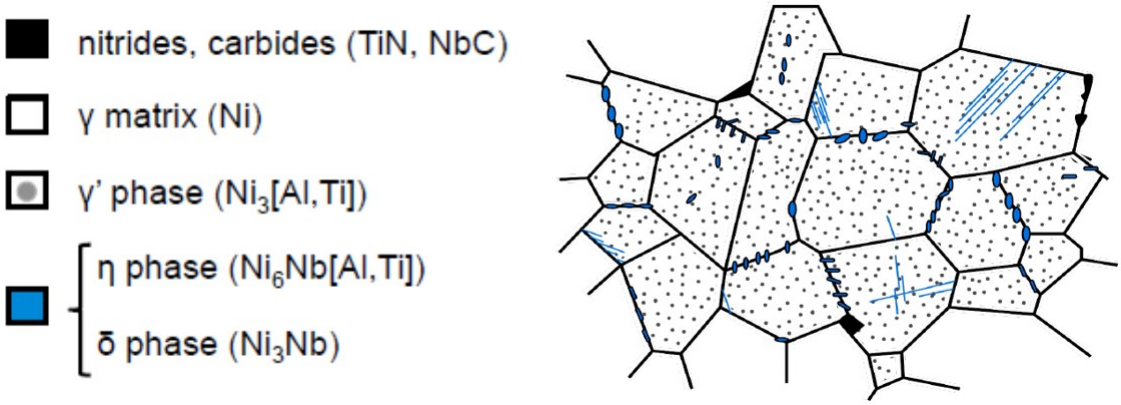

Fig. 2.2 Microstructural sketch of 718Plus.

that of Waspaloy. Niobium also causes the formation of a second precipitate, η/δ. A typical microstructure of 718Plus is sketched in Figure 2.2. This illustration shows γ' alongside two different appearances of η/δ, small bulky and long, thin. The microstructure does not necessarily consist of both morphologies simultaneously. In addition to the aforementioned material properties, the newly developed 718Plus maintains some of the cost advantage of IN718.

2.1.1 Chemistry 718Plus

The chemical composition of IN718 served as basis for the development of 718Plus (see Table 2.1). Three design targets were defined for 718Plus: higher temperature stability due to γ' precipitation, slow precipitation kinetics for better processability and reasonable material costs [8]. In the following section the reasons and consequences for the changes in the alloying elements will be discussed.

Aluminium and titanium are the most important elements to define the stability of γ'. The proportion Al/Ti as well as the overall content of Al+Ti regulate the precipitation of γ' and γ''. To obtain a γ' dominant alloy, Al+Ti was found to be greater than 3 at.% [9]. The ratio Al/Ti controlled the γ' growth rate as well as the matrix-precipitate misfit. Decreasing the Al/Ti ratio led to slower γ' growth but also to a lower misfit. The optimum mechanical properties were found for a total amount of Al+Ti of 4 at.% and an Al/Ti ratio of 2 at.% [9].

Additions of niobium lower the misfit by partitioning to the γ' and increase the overall precipitation volume fraction [9]. Niobium can trigger the formation of other precipitates such as δ and η. Antonov et al. [10] showed that, if the atomic ratio of Al/(Nb+Ta+Ti) is less than 0.85 the microstructure has a tendency to form δ and/or η (Figure 2.3a). 718Plus has a

calculated Al/(Nb+Ti) ratio of 0.733 and therefore would be in the η formation regime but close to the δ+η field (Figure 2.3b). Niobium also improves the processability of 718Plus. The reason is the low diffusion rate of niobium that directly influences the formation of γ'. As a result of the decreased precipitation kinetics the γ'-free processing window can be enlarged. These niobium containing alloys are unique in that the formation of γ' can be suppressed on cooling and have a very slow coarsening rate thereafter [11].

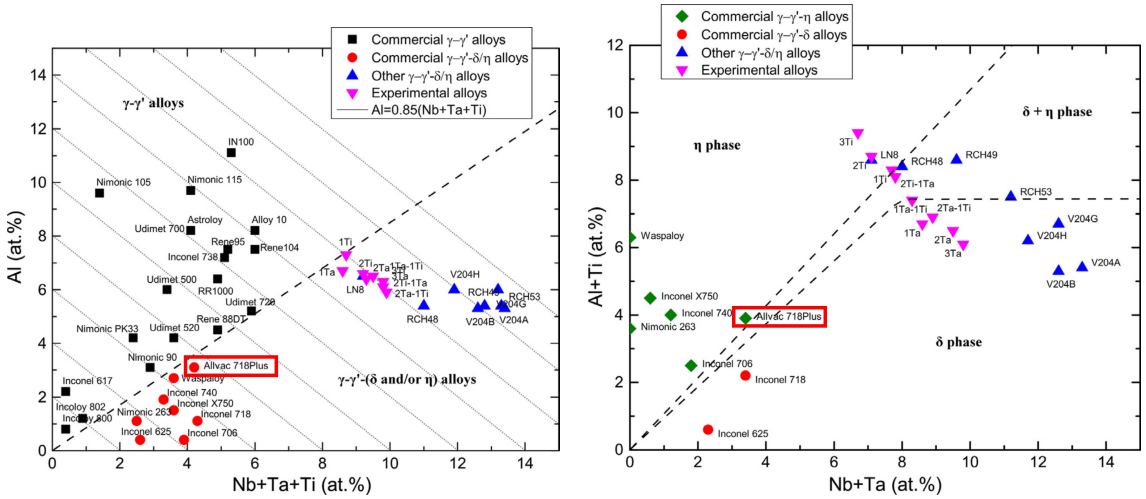

(a) (b)

Fig. 2.3 Elemental compositioning in nickel-base superalloys and their propensity to form (a) a single or multi-phase microstructure (b) η, δ or both [10]

The alloying element cobalt raises the γ' volume as it decreases the solubility of aluminium and titanium in the matrix [12]. Another effect of increasing the cobalt content is that it lowers the stacking-fault energy (SFE). Molybdenum and chromium have a similar effect on the SFE. Rising the amount of cobalt and reducing iron, the anti-phase boundary energy and the lattice misfit of γ' will be improved too, and therefore benefit high temperature stability [9]. Adding iron into a nickel-base superalloy lowers the price for the alloy but together with cobalt can cause the formation of topologically close-packed (TCP) phases.

Tungsten acts as a solid solution hardening element in the γ matrix and reduces the bulk diffusivity [9]. Due to the high atomic weight of tungsten the density of the overall material increases. Minor additions of phosphorus and boron improves the stress rupture life and creep rate as it increases the grain boundary strength [9].

Table 2.1 Chemical Composition of IN718, ATI® 718Plus™ and Waspaloy in wt.% [8]

	Ni	Cr	Mo	W	Co	Fe	Nb	Ti	Al	C	P	B
IN718	bal.	18.1	2.8	-	-	18.0	5.4	1.0	0.45	0.025	0.007	0.004
718Plus	bal.	18.0	2.75	1.0	9.0	10.0	5.45	0.7	1.45	0.020	0.014	0.004
Waspaloy	bal.	19.4	4.25	-	13.25	-	-	3.0	1.3	0.035	0.006	0.006

2.1.2 Microstructure 718Plus

718Plus is a multi-phase strengthening alloy where the various precipitates have different effects on manufacturing and mechanical properties. The γ matrix has a cubic-close packed crystal structure with a lattice parameter of a=3.596 Å at room temperature [13]. Its solidus temperature was measured to be 1258°C using differential scanning calorimetry (DSC) [14].

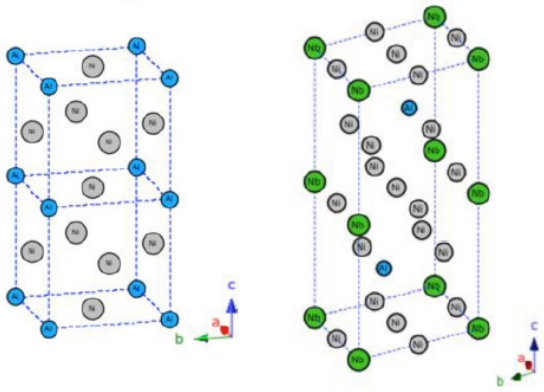

Fig. 2.4 Crystal structures γ' (left) and η (right) [15]

By adjusting the elemental fractions of IN718, γ' becomes the main hardening phase in 718Plus. The primary strengthening precipitate in 718Plus has a cubic ordered $L1_2$ crystal structure with a composition of Ni_3[Al,Nb,Ti] with the crystal structures shown on the left in Figure 2.4. The lattice parameter of γ' at room temperature was measured after the specimen was aged for 72 hr at 840°C to be a=3.608 Å [13]. Various solvus temperatures have been reported ranging from of 899°C [11] up to 967°C [16] but being mainly at around 960°C [14]. Due to the fact that γ' develops by an ordering mechanism from γ, its formation is difficult to suppress. However, decreasing the Al/Nb ratio reduces the size of secondary γ' precipitates [17]. Srinivasan et al. [11] showed evidence, that γ' in 718Plus could be suppressed completely by oil quenching.

ATI Speciality Metals recommends a two-step aging process after forging for the optimal precipitation of γ' [18]. This consists of 8 hr at 788°C followed by a furnace cool and a second heat treatment for 8 hr at 704°C. Typical γ' precipitates in 718Plus have a diameter

between 25 and 30nm [19]. The γ' volume fraction was modelled to range from 19.7% and 23.2% at 650°C [20]. Besides the size and fraction of γ', the lattice misfit between the γ and γ' phase is also of great significance. A small lattice misfit for coherent precipitation is associated with better strain hardening properties. It was measured to be -0.3%±0.2 using high resolution transmission electron microscopy [19]. The negative sign indicates that γ' is under tensile stress in the matrix.

The second precipitate found in 718Plus is η phase. The hexagonal η phase ($D0_{24}$) is an equilibrium precipitate with the indicative chemical composition Ni_6[Al,Ti]Nb (unit cell in Figure 2.4 on the right). The lattice parameters at room temperature are a=5.096Å and c=8.304Å [21]. Initial microstructural studies following the development of 718Plus misidentified η phase for δ phase (Ni_3Nb, $D0_a$, orthorhombic) [6, 22, 20]. The δ phase is often observed in IN718 as it is the equilibrium structure developing from the meta stable γ''. Even though Xie et al. [23] questioned the identification of δ in 718Plus it was Pickering et al. [21] who fully addressed the subject. They proved that the lamellar precipitate was the hexagonal η, consistent with the higher aluminium fraction [21]. A subsequent study of the microstructure revealed thin interlayers of δ and γ in the η phase which can be seen in Figure 2.5 [13]. The solvus temperature of the η/δ compound was determined to be $T_{\eta/\delta}$=1012°C and no difference could be made between η and δ [16]. For convenience reasons the η-δ-γ composite will be further referred to as 'η'. Ideal η should precipitate homogeneously in the form of thin rods at grain boundaries decreasing their mobility. Depending on the heat treatment and the thermo-mechanical history of the component these secondary particles can change morphology as well as preferred nucleation site [24]. The precipitates can lose the coherency with the γ matrix during sub-solvus forging. If followed by a heat treatment, η develops a coarse-plate morphology. In contrast, an η heat treatment on a strain-free material results in a fine lamellar morphology [25].

The body centred tetragonal γ'', the main strengthening phase in IN718, was detected to form in 718Plus by atom probe tomography and electron diffraction [26, 27]. It was only observed in very small quantities and was not considered of having a notable influence on the overall performance of the material. Niobium and titanium carbides, carbo-nitride eutectics as well as topologically close-packed (TCP) phases could be identified in the as-cast microstructure. The TCP phases observed in 718Plus are σ (D_{4h}^{14}) and C14 Laves ($D0_{24}$) both enriched in chromium, cobalt, iron, nickel and molybdenum [28]. The γ-η interface showed higher quantities of chromium, cobalt and iron which made these a preferred nucleation site for the C14 Laves and σ [29]. Metallographic analysis demonstrated a similar composition of the Laves eutectics and their lower frequency in 718Plus to IN718 [20].

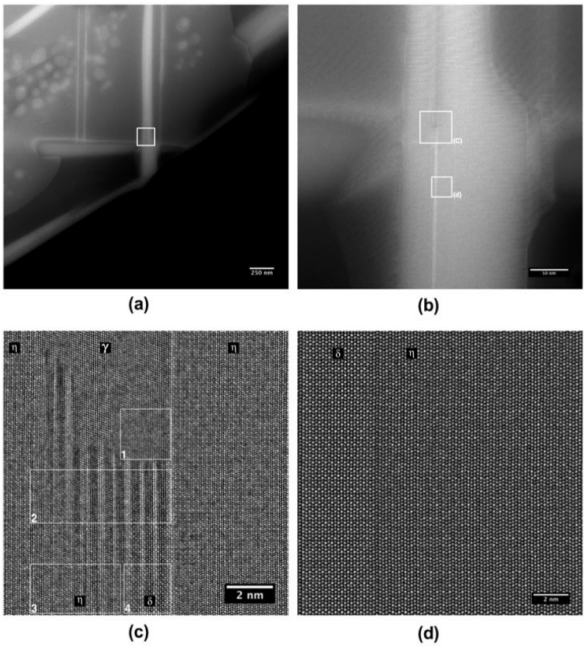

Fig. 2.5 High resolution transmission electron micrographs from the η precipitate with (b) being the close-up of (a) and (c) and (d) the respective areas highlighted in (b) [13]

2.2 Turbine disc manufacturing

The production of a disc from the raw material is a complex and expensive procedure. Knowledge of microstructural changes during each step are essential to tailor the whole process to the preferred final microstructure. It can be subdivided into two parts: the production of the billet material from the ingot and the following manufacturing steps to develop the final component.

2.2.1 Billet production

The billet material, used as initial material for the forging, requires a cast ingot to undergo a further melting step and a cogging procedure to refine the microstructure.

To ensure a high quality disc material the initial processing is crucial. The production of the ingot requires three process steps consisting of the primary melting and subsequent remelting procedures. For the primary stage vacuum induction melting (VIM) is used to produce an initial stock of material containing the desired chemical composition. However, impurities such as oxygen or trace elements are still present which leads to the need for a remelt. Electro-slag and vacuum arc remelting (ESR and VAR) are the procedures of choice to fabricate an ingot with the required chemical composition and homogeneity.

The as-cast ingot cross-section contains a coarse and highly heterogeneous microstructure owing to the temperature gradient from melt pool to furnace walls. In the cogging procedure this microstructure is converted into a finer and more homogeneous state by hot forging [30]. To accomplish this a series of open-die forging steps are performed. Between each compression step the ingot is rotated to achieve an even cross-section and microstructure. During the forging process recrystallisation and grain growth determine the final grain size of the billet [31]. Even though temperature and strain gradients from centre to rim give a non-uniform grain size throughout the entire cross-section, the mid-radius section shows a constant value. The final billet is then cut into smaller discs for the subsequent forging stage into near a net shape.

2.2.2 Disc manufacturing

The manufacturing of the disc from the billet requires a forging step followed by a heat treatment and final machining, outlined in Figure 2.6.

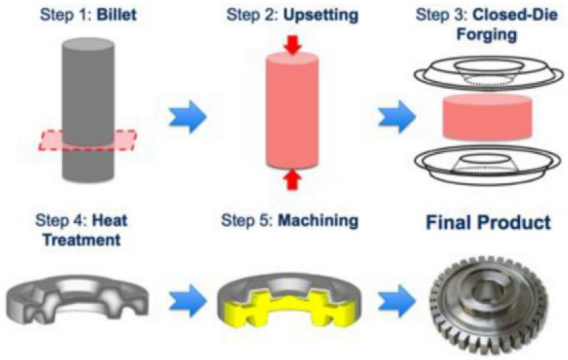

Fig. 2.6 Turbine disc manufacturing process steps [15]

The billet material obtained from the cogging procedure is forged close to the final shape through a closed die forging process. The final microstructure for the component is determined by this step and hence, detailed knowledge of this process is essential. Turbine discs are 'isothermally' forged with dies having a similar temperature to the pre-heated billet material. Several forging steps are required to obtain the desired shape. As during cogging, recrystallisation occurs producing a change in grain size. Along with dynamic recrystallisation, the shape of η precipitates is heavily influenced by this process. Residual strain from forging stimulates η precipitation at grain boundaries in the subsequent heat treatment [32]. It has also been found that η has a preferred alignment with the flow lines during the compression [24]. With η precipitates inhibiting grain growth, two forging routes have been established for 718Plus; η sub-solvus and super-solvus. In this respect, the η

phase solvus temperature of ~1000°C marks the threshold temperature. The lower bound value for the forging window is dictated by the γ' solvus temperature to reduce the resistance of the material against deformation.

The heat treatment of the forged turbine disc aims for a well-defined microstructure ready for service. An ideal distribution of precipitates as well as optimal grain size are the target of this process step. Figure 2.7 presents a typical microstructure of sub-solvus forged and heat treated 718Plus. η is of blocky shape and precipitates at the grain boundaries and the grain size is about 12 µm in diameter. ATI Specialty Materials Ltd. developed guidelines for the heat treatment of 718Plus [18]. Following the sub-solvus forging a two-step heat treatment should be carried out. A solution treatment between 954°C and 982°C attempts to stabilize size and fraction of η. The recommended subsequent ageing should be carried out at either 704°C or 788°C. Its main purpose is a controlled γ' distribution throughout the component.

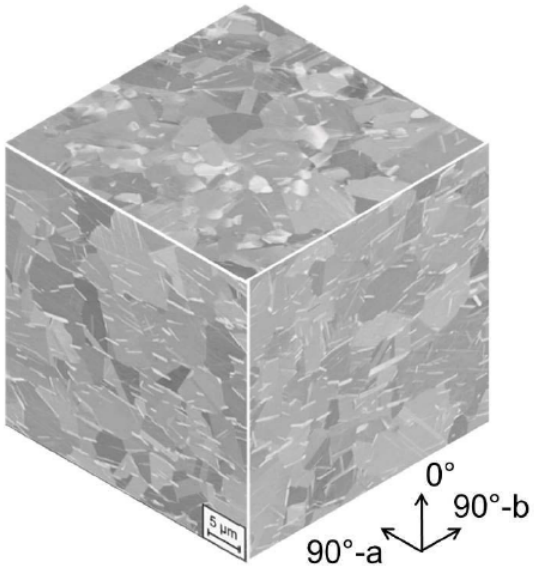

Fig. 2.7 Microstructure of 718Plus after subsolvus forging and standard heat treatment [33]

During the closed-die forging excess overhang or 'flash' occurs which shows a different microstructure due to higher temperatures and faster cooling rates. Therefore, the final manufacturing step is to turn the turbine disc on a lathe. To keep the costs of the product down the amount of machining is kept to a minimum as nickel-base superalloys are difficult to machine and tool life is short. The removed material can be recycled in a new ingot.

2.3 Microstructural changes during hot working

A key aspect of processing metallic alloys is a thorough understanding of restoration processes happening in the microstructure. These recover the ductility of the material and also define the grain structure after the forming process. During the hot working of an alloy, a number of microstructural mechanisms can take place. The deformation of a material is attended by an increase of the internal energy. This increase in energy in the workpiece destabilises the thermodynamic equilibrium of the microstructure. To rebuild the thermodynamic equilibrium and decrease the internal energy, restoration processes take place. The main mechanisms to diminish this energy are recovery, recrystallisation and grain growth.

2.3.1 Recovery

Recovery includes the rearrangement and annihilation of dislocations stored in the worked material. It is a thermally activated process and can occur during (dynamic recovery-DRV) or after deformation (static recovery-SRV). Recovery does not lead to a fully restored microstructure because significant dislocation structure will remain. Humphreys et al. [34] distinguish between three stages of recovery: dislocation annihilation, dislocation rearrangement and subgrain growth.

Dislocation annihilation and rearrangement involve glide, climb and cross-slip of dislocations. The thermal activation for climb is attributed to the motion of vacancies while for cross-slip the partial dislocations in low stacking fault materials need to recombine again before moving onto another plane (see Chapter 2.1.2). The lower the stacking fault energy (SFE), the further apart the partials can be and it needs a higher temperature to move them back together [35]. Dislocations can annihilate each other but can also decrease the overall energy by forming low angle grain boundaries. These low angle grain boundaries are formed during the process of polygonisation. Therefore the dislocations in the bent crystal form a number of polygons reducing the elastic strain in the lattice [36]. As the energy per dislocation decreases with increasing the boundary misorientation, the microstructure will tend to form higher misoriented boundaries with the progression of recovery [34].

Due to its underlying processes, recovery is thought to be the primary restoration mechanism in high-stacking fault materials such as aluminum or tungsten [34, 35, 37]. It is believed, that dynamic recovery is a mechanism competing with dynamic recrystallisation [38, 34, 37]. During recovery dislocations form cell walls which can further develop into mobile subboundaries [39]. The subcells within these boundaries can serve as a nucleus for a dynamically recrystallised grain [40]. On the one hand, recovery enables dynamic recrystallisation, but on the other hand, it decreases the stored energy available.

2.3.2 Recrystallisation

Recrystallisation is the development and growth of new grains in a deformed microstructure. Therefore, high angle grain boundaries need to form and migrate, diminishing the stored energy within the deformed grains. After recrystallisation, grain growth continues because grain boundaries are thermodynamically unstable. The driving force for this process is not the energy stored via dislocations but the reduction of the grain boundary area itself [41].

While material properties determine the response to external influences, forging parameters specify the energy introduced. The forging process defines strain, strain rate, temperature and time. Numerous studies have been carried out to increase the understanding between the interplay of these parameters and their effect on the work piece [42, 22, 43, 44].

Recrystallisation can be subdivided into two steps, viz., nucleation and growth. Various types of recrystallisation have been identified. Static recrystallisation (SRX) occurs during annealing processes following deformation. Dynamic recrystallisation (DRX) occurs during deformation when a critical strain is reached and at temperatures generally above of $0.5\,T_m$. Meta-dynamic recrystallisation (MDRX) is termed the further grain boundary migration after DRX due to the stored energy in form of dislocations. DRX and SRX can further be divided in continuous and discontinuous recrystallisation. Continuous recrystallisation is identified by a homogeneous grain size distribution and recrystallised fraction during the whole restoration process. If the microstructure shows localised recrystallisation as well as deformed grains the mechanism behind is termed discontinuous [37]. An overview of the recrystallisation mechanisms discussed is given in Table 2.2.

Table 2.2 Overview of the types of recrystallisation [37, 45–47]. The influence on the kinetics is marked with strong (+), medium (o) or weak (-)

	Recrystallisation					
	SRX		DRX			MDRX
	discontinuous	continuous	discontinuous	continuous	geometric	
Conditions						
$<\varepsilon_{DRX}$	<2	<2	<2	<2	>3	
appearance	after deformation		during deformation			after deformation
SFE	low	high	high	low to high	low	
Microstructure						
nucleation sites	grain boundaries	grain interior	grain boundaries	grain interior	grain interior	
nucleation mechanism	subgrain growth	subgrain growth	SIBM, subgrain growth	subgrain growth	subgrain growth, HAGB impingement	grain growth
Influence on kinetics						
T	+		+	-	o	o
ε				-	+	-
$\dot{\varepsilon}$	-		+	-	+	+
D_0			+	-	-	
Annealing behaviour	SRV	SRV	MDRX/dSRX	MDRX/dSRX	cSRX	

2.3.2.1 Static recrystallisation

Static recrystallisation (SRX) takes place during the annealing of a previously-deformed metal. The deformation has ceased before reaching the critical strain for the nucleation of dynamic recrystallisation. During annealing, low angle grain boundaries (LAGB) develop and transform into high angle grain boundaries (HAGB) of the newly recrystallised grains.

The evolution of SRX is driven mainly by temperature and strain, whereas strain rate plays a less important role [48]. It has been extensively studied for cold-rolled austenitic steels and can appear as a post-deformation mechanism [49, 50, 37]. However, its kinetics in 718Plus was found to be too slow to be significant after forging of 718Plus [22].

Discontinuous SRX (dSRX) is found in low stacking fault energy materials and the evolving microstructure shows recrystallisation nucleating along deformed grain boundaries. The subgrains start growing preferably at grain boundaries and merge, causing an imbalance at the boundary. This provokes the HAGB to bulge out forming a large subgrain. Subsequent merging events eventually lead to a grain bordered with a HAGB on every side.

Continuous SRX (cSRX) retains a homogeneous microstructure throughout the transformation of deformed to recrystallised grains. The terminology was used for at least two different observed phenomena of SRX. Firstly, for gradual subgrain growth with the development of high angle grain boundaries in the whole grain [37]. It has been observed in aluminium, a high stacking fault energy material [51]. A second mechanism was referred to as cSRX which occurred after the material has been deformed to large strains. The high deformation results in a microstructure with elongated grains and their HAGB almost intersecting. An annealing procedure triggers small movement of the boundaries leading to a fine-grained recrystallised microstructure [34]. These two very different definitions of cSRX can cause confusion when microstructural changes are attributed to a specific recrystallisation mechanism.

2.3.2.2 Dynamic recrystallisation

The microstructure of dynamically recrystallised metals differs significantly from those undergoing SRX. Dynamic recrystallisation (DRX) occurs during the deformation process at temperatures $T/T_m > 0.5$ [34]. At a certain threshold value of dislocation density, new grains can nucleate and grow. Due to the ongoing deformation, newly-recrystallised grains can gradually increase their dislocation density as-well. Hence, substructures are continuously formed and exist in the final microstructure.

Three different types of DRX have been observed: discontinuous, continuous and geometric DRX. Discontinuous DRX (dDRX) is characterised by a heterogeneous evolution

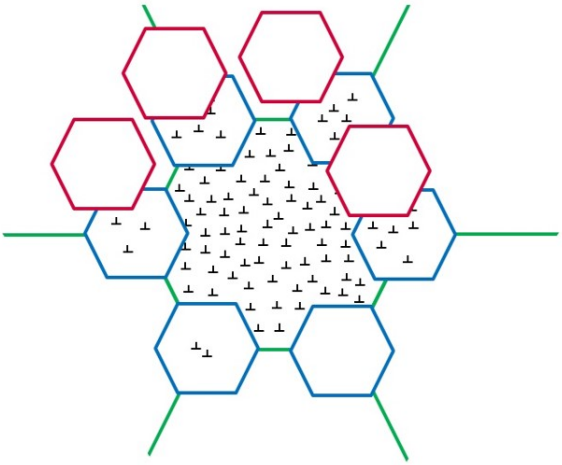

Fig. 2.8 Necklace structure of dDRX

of recrystallisation in the microstructure. It is usually reported in low stacking fault energy materials and low strains ε<2 [37]. Recrystallised grains are supposed to form primarily at grain boundaries via strain induced boundary migration (SIBM). This mechanism results in the characteristic 'necklace' structure which are small, recrystallised grains at the former boarders of larger, unrecrystallised ones. Figure 2.8 schematically pictures the stages of necklacing during DRX. During deformation of the initial grain with the green boundaries, the dislocation density increases. At a certain threshold, the nucleation of recrystallised grains (blue) is triggered at the grain boundaries. This is referred to the first necklace structure. With continuing deformation, the dislocation density in the recrystallised grains increases eventually recrystallising them (red grains).

Continuous DRX (cDRX) occurs for high stacking fault energy materials such as aluminium. In contrast to dDRX, cDRX is termed as the simultaneous recrystallisation of the whole microstructure. During cDRX all areas are at the same stage in the evolution of DRX and deformed areas should not exist alongside recrystallised regions. Subboundary migration takes place throughout the microstructure leading to an evenly-distributed grain orientation spread (Figure 2.9). Three different ways of converting low angle grain boundaries (LAGB) to HAGB have been reported [47]. At high temperatures a homogeneous increase of misorientation (HIM) is the first type illustrated at the top in Figure 2.9. The other two options are progressive lattice rotation near grain boundaries (LRGB) and via the evolution of microshear bands (MSB). cDRX is believed to have a slower kinetics than dDRX due to the formation of subgrains at high strains [37].

Geometric DRX (gDRX) develops in high SFE materials at large strains and is characterised by a strong geometric deformation of the grains. Figure 2.10 shows the stages of

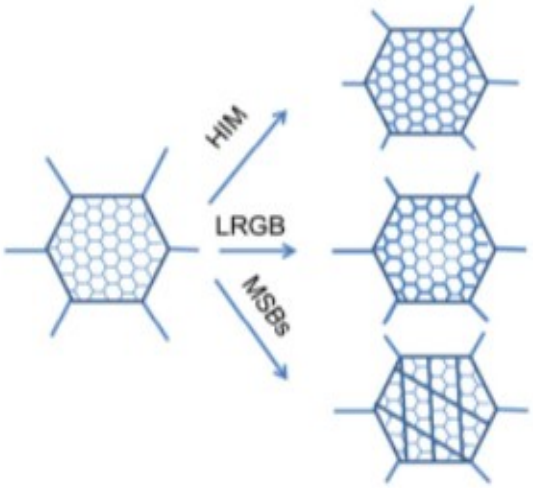

Fig. 2.9 Subgrain formation cDRX [47]

gDRX. Subgrains form in the interior of the grain (thin lines) which are bordered by HAGB (thick lines). During deformation at low strain rates serrated HAGB are generated. These boundaries move closer to each each other in the ongoing deformation, eventually coming into contact and nucleate recrystallised grains [52].

DRX is affected by microstructural constants as well as testing parameters. The stacking fault energy dictates how large the distance between a pair of partial dislocations can be. For materials with a high stacking fault energy (e.g. aluminium) the development of a stacking fault between the two partials is penalised with a large increase in the overall energy. Nickel-base superalloys as an example for low stacking fault energy materials suffer from a much lower energy penalty upon the splitting of a dislocation. Hence, partials in a low SFE material can glide through the microstructure with a bigger distance apart. The formation of subgrains requires the cross-slip or climb of dislocations which is only possible for a full dislocation. Therefore it is easier in systems where dislocations do not dissociate or can recombine again easily because of the short distance between the partials [47].

Another microstructural parameter affecting the recrystallisation rate is the initial grain size. As already pointed out, it can lead to single or several cycles of DRX [37, 53]. The grain boundaries also serve as a preferred nucleation site for recrystallised grains [34]. Larger grains lead to less recrystallisation, a fact incorporated in most DRX models [54, 55].

Temperature, strain and strain rate mainly affect the kinetics of dDRX [56, 34]. Temperature increases the grain boundary mobility and decreases the stacking fault energy. The recrystallised area becomes larger with temperature [57, 34]. The same is true for the influence of strain. The higher the strain, the more internal energy is available for DRX

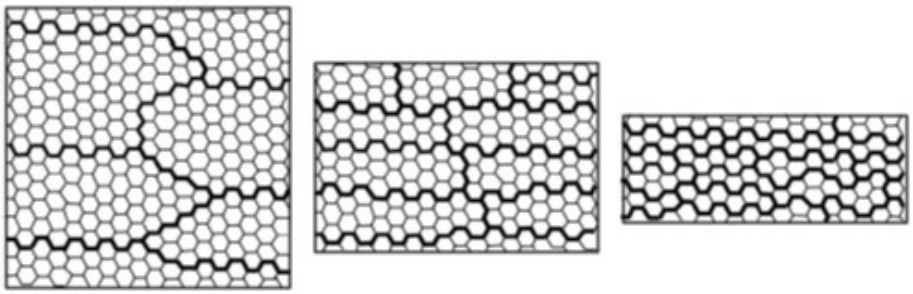

Fig. 2.10 High angle grain boundary coalescence during gDRX [47]

to evolve [58]. This pattern is less clear for the effect of strain rate on the microstructural changes during DRX. In low SFE materials the DRX fraction was reported to show a two-fold trend when plotted against the strain rate. At strain rates from 0.001 to $1s^{-1}$ the recrystallised area decreases with strain rate and then increases for higher values of strain rate [59, 60, 47]. Studies on IN718 confirmed the general observations [61]. This trend could not be reproduced in all materials. In a high-temperature compression test analysis for a powder metallurgically manufactured nickel-base superalloy, the DRX fraction increases between a strain rate of 0.01 to $1s^{-1}$ [62]. 718Plus likewise was reported to show this unusual behaviour [63, 64]. The general explanation brought forward in all of these studies was a change in DRX mechanism from cDRX to dDRX - and vice versa. Another commonality is the lack of microstructural evidence to confirm this statement. It could be suggested, that the nucleation mechanism shifts from subgrain formation to strain induced grain boundary bulging. However, dDRX contains both of these nucleation mechanism. A fact which is frequently overlooked. The occurrence of subgrains in a microstructure leads to the inaccurate conclusion that cDRX is operating. In addition, cDRX is defined to occur homogeneously within the whole grain and therefore by definition cannot produce a necklace structure.

During a high temperature compression test, the shape of the flow curve changes as a result of DRX. After the yield point is reached the dislocation density increases rapidly and the material undergoes work hardening. With the additional energy provided from the hot forming the mobility of grain boundaries and dislocations is enhanced compared to cold deformation. This thermal activation can trigger DRX. Hence, work hardening and DRX are competing processes which run in parallel. The critical strain or dislocation density can be extracted from the flow curves to determine the onset of recrystallisation [65]. DRX contains a nucleation stage and the softening effect on the flow curve is not obvious from the beginning. Only after the peak stress has been reached, the rate of recrystallisation exceeds the effect of work hardening and the flow curve drops. A steady state is reached when the flow curve stays horizontal. In this case, the rate of work hardening and recrystallisation are

balanced. The steady state flow stress depends on temperature and strain rate and so does the recrystallised grain size [47]. The softening stage of the flow curve can be marked either by a single peak or multiple peaks. It was found, that the transition from single to multi peak depends on the initial and steady state grain size [66]. Multiple peaks occur, if the steady state grain size is at least twice as big as the initial grain size.

Post-deformation mechanisms operating after DRX are meta-dynamic recrystallisation (MDRX) or dSRX. If the strains during deformation have reached the steady state of the flow curve, only MDRX occurs. For strains near the peak strain dSRX with a nucleation stage takes place. In the transition zone between peak strain and steady state both mechanisms might appear [22].

2.3.2.3 Meta-dynamic recrystallisation

Multi step forging involves intervals between the deformation steps. During these dwell times the component is kept at high temperatures, which activates recovery and recrystallisation processes. Static recovery (SRV), static recrystallisation and meta-dynamic recrystallisation are restoration mechanisms occurring after deformation has stopped. SRV only plays a minor part in the evolution of post-deformation microstructures [34]. SRX and MDRX mechanisms are in place if the preceding deformation has not reached steady state [45]. The key difference between these two processes is, that MDRX does not require a nucleation stage as only previously recrystallised grains grow by MDRX. Because of the technological importance of MDRX much attention has focused on its kinetics and dependencies on preceding DRX [67, 68, 58]. MDRX happens instantaneously after DRX without an incubation period [12]. In the post-deformation regime, nuclei formed during DRX continue to grow into the partially recrystallised matrix. While the kinetics of dDRX depends on temperature and strain, MDRX is principally affected by strain rate and is insensitive to strain [46]. As dDRX is strongly influenced by strain the flow curves can be easily distinguished from MDRX as a post-deformation softening.

The contribution of MDRX to the overall recrystallised area is difficult to measure due to the smooth transition between these two mechanisms. Two different testing methods have become established so far: the double-hit compression and the stress relaxation test [69, 48]. For the first approach, the deformation parameters are set in a way to achieve a fully dynamically recrystallised microstructure. After the first compression the sample is kept at high temperature at a set time to achieve MDRX. The second hit will then reveal the microstructural softening during the interpass time. A stress relaxation test logs the force after compression at a constant strain rate.

2.3.2.4 Nucleation

The nucleation of recrystallisation is still under debate as it is experimentally challenging to distinguish it from the growth stage. Various theories have been suggested for dynamic recrystallisation and the following five mechanisms will be discussed: classical nucleation, subgrain growth/coalescence, strain induced grain boundary migration, grain boundary ledge and particle-stimulated nucleation.

Classical nucleation theory

In the classical homogeneous nucleation theory random thermal fluctuations trigger the formation of a nucleus. The driving force for continuous growth is the difference in Gibbs energies between matrix and nucleus, ΔG. More prominent is heterogeneous nucleation at existing defects or precipitates. Classical nucleation theory is unlikely to happen during recrystallisation. The driving force provided by the dislocations is not high enough to provoke the necessary thermal fluctuations. In addition, the grain boundary energies involved in recrystallisation are larger than in classical nucleation [70]. With these facts in mind it is now widely accepted that classical nucleation theory does not apply to recrystallisation.

Subgrain growth and coalescence

Nucleation caused by low angle grain boundary migration, i.e. subgrain growth, was established in the 1950s by Cahn and Cottrell [36, 71]. A subgrain is formed by the polygonisation of dislocations. One subgrain continues growing at the expense of the surrounding smaller subgrains or cells. The driving force for this process is the energy reduction due to absorption and annihilation of dislocations. The individual subgrains need a progressive accumulation of misorientation to achieve a high angle boundary. As the individual dislocations marginallydistort the lattice in a certain area (i.e. generate the grain misorientation), twinning is a mechanism to quickly achieve a mobile HAGB within a short growth distance. The subgrains formed can twin several times to form mobile higher angle grain boundaries [72]. With the four twin variants in a CCP material the final microstructure can have a wide spread in grain orientation.

Subgrain coalescence describes a nucleation mechanism caused by rotation of two adjacent subgrains. One subgrain can rotate by the diffusion of atoms. The boundary between the two former subgrains vanishes after a successful rotation. Experiments as well as computer simulations have been carried out to verify this mechanism [73, 74]. Common to the studies to date is the importance of the grain boundary structure. A molecular dynamics simulation by Molodov et al. [74] suggests that only tilt boundaries are capable of the required dislocation annihilation.

Strain induced boundary migration

The nucleation process of strain induced boundary migration (SIBM) is frequently observed during DRX in nickel-base superalloys [75][76][77]. Figure 2.11 illustrates the steps required for a successful nucleation by SIBM. Serrated grain boundaries develop due to different dislocation densities in adjacent grains separated by subboundaries (a). For low strains grain boundary sliding occurs increasing the local strain (b). In the final nucleation stage parts of the corrugated boundaries bulge out leaving behind an area of low dislocation density (c). The bulging is assisted by subgrain formation or twinning. As there exists an orientation relationship between nuclei formed and the adjacent grain the recrystallised microstructure should be linked to the deformed [34]. It was suggested that the formation of twins might lead to numerous crystallographic orientations.

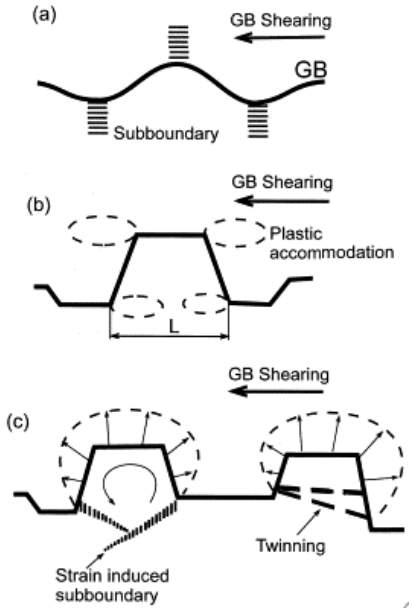

Fig. 2.11 Strain induced grain boundary migration; (a) subboundaries pomote GB serration optionally followed by (b) grain boundary sliding and finally (c) bulging with strain-induced subboundary formation or twinning [78]

With the formation process in mind, the twins developed during SIBM are categorised as annealing twins. Annealing twins evolve during grain boundary migration while deformation twins form under stress by the movement of partial dislocations [79]. The growth accident theory is based on the assumption that stacking errors at migrating grain boundaries leave behind twin boundaries.The mathematical description of the growth accident model is based on grain boundary migration distance and grain boundary migration velocity [80, 81]. Twins can enhance the mobility of the growing grain by a change in orientation. Multiple twins

are found in low stacking fault materials leading to a heterogeneous orientation in the recrystallised microstructure [82].

Besides the importance of twin formation during the nucleation, twins also play a vicarious role in the development of recrystallised grains. Twin boundaries can accelerate the nucleation and development of DRX grains [75, 77]. Twins act as an obstacle for dislocations and locally increase the stress concentration which further promotes grain nucleation.

Grain boundary ledge model

The grain boundary ledge model was developed for a uniformly deformed and unrecovered material [83]. In this microstructure no subgrains have formed and the dislocation density between neighbouring grains are identical. It was suggested, that a ledge forms at a grain boundary in accordance to a slip plane. To minimize the overall energy the grain boundary straightens and leaves a dislocation free area. The generated nucleus can then grow into the adjacent grain by boundary movement.

2.3.2.5 Multi-phase systems

Precipitates play an essential role to achieve the required mechanical properties of industrial alloys. Industries invest a tremendous amount of work and resources in the development of the right heat treatment for a specific alloy and application. Significant research has been dedicated understanding the interaction of second-phase particles with manufacturing routines. In the following section, the influence of precipitates on the recrystallisation mechanisms will be discussed

Second-phase particles can have multiple effects on the different stages of recrystallisation and have been discussed by Huang et al. [84]. They can affect the dislocation movement and subsequently the deformed state. The modification of the deformation structure can change the recrystallisation kinetics. In addition, the increase in stored energy within the material can lead to new precipitation. Second-phase particles also have a direct influence on recrystallisation such as grain nucleation, grain boundary pinning or the evolution of a recrystallisation texture.

Humphreys et al. [34] present a thorough review on the effect of second-phase particles on recrystallisation. In a multi-phase alloy the nucleation kinetics of recrystallised grains depends on the particle size. Small particles can have retardation effect while large particles were found to benefit nucleation via the so-called particle stimulated nucleation (PSN) [35]. The retardation effect of finely dispersed precipitates can be explained by the formation and growth of subgrains. Subgrains are formed in the vicinity of grain boundaries but the necessary growth and coarsening can be hindered by fine particles pinning these LAGB [34].

Particles can even disturb the formation of a subgrain boundary by acting as an obstacle for dislocation movement [84]. Another influence of small precipitates on the nucleation of recrystallisation is the homogenisation of the dislocation structure [85]. Recrystallisation by subgrain coarsening requires a certain orientation gradient for the transition of a LAGB to an HAGB. Particles can cause a more homogeneous dislocation structure compared to a single-phase microstructure resulting in a smaller recrystallised area. Besides the evidence of the retardation effect of fine particles on the nucleation of recrystallisation, some studies found an improved nucleation behaviour [86]. They claim, that the advantage or disadvantage of fine dispersoids in the matrix depends on volume fraction and particle radius [84].

The growth of recrystallised grains is in general impeded by the existence of small particles [35]. The interaction of a moving grain boundary with a particle was described by Smith and is known as 'Zener-pinning' [87]. The Zener-pressure is more effective on HAGB leading to a reduction in recrystallised fraction. In two cases the adverse pinning effect on recrystallisation is circumvented [84]. Firstly, if the dislocation density is high enough, the driving force for recrystallisation can overcome the Zener-pressure [88]. Secondly, if recrystallisation occurs in a supersaturated solid solution. The precipitation occurring simultaneously act as chemical driving force in addition to the dislocation density [35].

Particle stimulated nucleation

Particle stimulated nucleation (PSN) is a mechanism mainly observed for static recrystallisation [34]. During cold deformation, large undeformable particles cause a deformation zone around them with a high orientation gradient. Subgrain boundaries formed in this area can quickly transform into HAGB. The critical precipitate size to act as a nucleation site for PSN is typically 1 µm [34]. This value can be lowered by increasing the strain. For a successful contribution of PSN to the overall recrystallisation it is necessary, that the formed nucleus acquires a HAGB when it reaches the end of the deformation zone around the particle.

PSN during hot deformation can be difficult because of the temperature dependent nature of dislocations. A minimum critical strain rate is required for the formation of nuclei by PSN. The temperature at which the deformation happens needs to be within limits [34]. However, a number of studies seemed to observe PSN during high temperature deformation alongside DRX. The molybdenum-zirconium alloy MZ-17 is classified as a high-stacking fault energy material. Silva et al. [89] performed compression tests at temperatures ranging from 800°C to 1200°C. ZrO_2 particles were measured to be 1.3 µm. Even though the authors claimed to be able to detect dynamic recovery, dynamic recrystallisation and particle stimulated nucleation, the data presented does not provide enough evidence for this conclusion. In a study on Ni-30wt.%Fe alloy, a few recrystallised grains nucleated by PSN could be observed using EBSD and TEM techniques [90]. The effect of PSN on the overall recrystallised fraction was

concluded to be minor. The high temperature recrystallisation behaviour of Waspaloy was characterised with double-cone high temperature compression tests by Semiatin et al. [91]. The optical micrographs presented show evidence of localized recrystallisation around large carbides of ~10 µm in size. They observed faster recrystallisation kinetics than previously reported and ascribed this to the combined effect of PSN and DRX [91]. PSN during high temperature deformation has not only attracted attention for experimental studies but also modelling approaches. A cellular automata model was developed by Goetz [92] to reproduce the microstructural observations from Semiatin et al. One of the assumptions of the simulation was that particles automatically act as additional nucleation site without consideration of the dislocation kinetics. The model was used for a quantitative analysis on the changes in the Avrami-exponent during DRX rather than a qualitative study of the possibility of PSN. Nimonic 80A is a nickel-base superalloy studied with respect to the interaction between PSN and DRX. A study characterising Nimonic 80A during hot compression observes the presence of recrystallised grains around carbides [93]. The disagreement of this finding with a similar study [94] was explained by the effect of adiabatic heating during deformation. However, another reason might be influencing this work and could act as an explanation for the observed PSN during recrystallisation. The tests were designed to simulate the conditions in a screw press. As such, the samples were cooled in air after deformation. Due to the slow cooling from the test temperature, the sample could have been recrystallised by means of MDRX as well SRX. PSN is well known for taking place during SRX, hence the study by Pérez cannot prove PSN during DRX.

IN718 with δ phase is, in terms of precipitation morphology, the most similar multi-phase nickel-base superalloy to 718Plus with its η phase. The microstructural evolution during hot deformation can be assumed to be comparable to η-containing 718Plus. Numerous studies have investigated the interaction between dynamic recrystallisation and δ in IN718.

A high temperature deformation testing sequence analysing two different δ morphologies was published by Lalvani et al. [95]. The microstructure containing fine blocky δ in the grain interior and thin acicular δ at the grain boundaries recrystallised firstly at the grain boundaries, as expected for DRX. The volume fraction of δ was measured to be ~27%. They presented optical micrographs to show that recrystallisation happened in the denuded zones around grain boundary precipitates and that the general DRX behaviour was hindered by the precipitates. In the second morphology with 22% of long acicular δ recrystallisation occurred together with the alignment and dissolution of δ. Dissolution of δ was also observed by Wang et al. [96]. In addition, they found most of the recrystallised grains at or in the vicinity of δ. Even though this could indicate PSN, they came to the conclusion, that strain induced grain boundary migration was the main nucleation site of DRX. The phase boundaries between δ

and the γ matrix were identified as the primary nucleation mechanism for DRX in a further study [97]. As δ is a grain boundary precipitate and DRX usually starts at HAGB, it is difficult to distinguish PSN from other nucleation mechanisms known for DRX. Even more so when the precipitate partially dissolves or realigns during the deformation [98, 97]. The δ phase also seemed to be the reason for an increase in texture with strain rate in a γ-γ'-δ ternary eutectic nickel-base superalloy [99].

Heteroepitaxial recrystallisation

Heteroepitaxial recrystallisation (heRX) has first been reported in nickel-base superalloys by Charpagne et al. [100]. They describe a recrystallisation mechanism in René 65™ which involves the inverse precipitation from γ' to γ. During the cooling after a heat treatment, coherent γ shells form around primary γ' particles. In a subsequent high-temperature deformation step, these γ shells can continue to grow driven by the stored energy. This mechanism eventually leads to a microstructure with coherent primary γ' precipitates in the γ matrix [101]. HeRX is expected to occur for γ-γ' alloys with a low lattice mismatch and was also found in Udimet 720 [102]. It is stimulated by high strain rates and low temperatures and shows peak formation at strains ε=0.5.

Microstructures recrystallised by heRX show a recrystallised fraction of up to 13% for strains below ε=0.5. Hence, the nucleation barrier of heRX grains must be lower than for DRX grains. An analytical study derived the driving force for an heRX nucleus [103]. By treating the pre-existing γ' particle as a nucleus, the authors come to the conclusion, that the critical size for a γ nucleus is zero for small dislocation densities hence its stability at low strains. It could be assumed, that a main requirement for the appearance of heRX is the ability of the formation of a coherent particle-matrix interface. However, further alloy systems need to be analysed to fully explain the mechanism of heteroepitaxial recrystallisation.

2.3.3 Grain growth

The microstructure is not fully stable after the stored energy has been consumed by recrystallised grains. Hence, the grains continue to grow aiming for the smallest possible overall free energy. In comparison to recrystallisation, the driving force for grain growth is the overall grain boundary area [34]. Grain growth will be facilitated by either grain shrinkage or growth, depending on the initial grain shape: larger grains grow at the expense of the smaller, increasing the average grain size and reducing the driving force. Temperature and precipitates/particles have a major influence on the growth kinetics. High temperatures increase the grain boundary mobility while particles such as γ' act as obstacles and can pin the moving boundary [104].

A microstructure which has already experienced grain growth shows a smaller proportion of twin boundaries with respect to the initial recrystallised system [105]. Twinned recrystallised grains are absorbed by growing ones which themselves do not create new twins indicating that stacking errors are made more likely in heavily deformed microstructures.

Normal and abnormal grain growth can occur in a recrystallised structure. Normal grain growth is referred to as homogeneous grain growth without any distinct differences between individual grains. The opposite is true for abnormal grain growth where a bimodal grain size distribution is found in the microstructure leading to a few grains much larger than average.

2.4 Microstructural modelling of recrystallisation

Both researchers and industry aim to develop models which accurately predict the material response to external impacts. There are two main reasons for simulating the material behaviour. A material model can be used to diminish the number of expensive hardware tests as well as helping to understand fundamental theories about material behaviour. The variety of modelling techniques used on different length scales is evidence for its importance and need. Choosing an appropriate method for a given task requires a thorough understanding of its capabilities as well as weaknesses.

Figure 2.12 presents an overview of computational and experimental techniques available for different length and time scales. In this study EBSD and TEM will be used to analyse the data. On the same length and time scale discrete dislocation dynamics together with continuum models - analytical and numerical - can be used to verify the data and build additional knowledge.

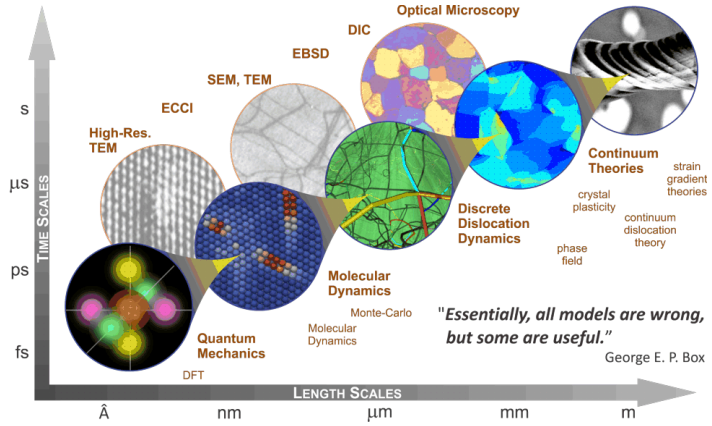

Fig. 2.12 Computational and experimental techniques for material characterisation [106]

Simulating recrystallisation demands a formalism for the nucleation stage and mobility data for the subsequent recrystallisation and grain growth. In addition to that, dynamic recrystallisation requires continuous information about the deformation conditions. Due to this complex system particular problems are approached on different length scales as outlined in Figure 2.12. Whereas for an overall prediction of, for example the recrystallised fraction, a constitutive model on a macroscale is sufficient, it might not be capable of reproducing local effects. In this respect, a more time consuming full-field approach could have some advantages.

2.4.1 Analytical continuum mechanical models

Constitutive equations are widely used for industrial applications. Their advantage is that they are time-efficient, clear and simple to implement into other numerical programs for example a finite element (FE) framework.

For an FE calculation the flow curve of a material is important to compute the evolving stress and strain field. To interpolate the flow stress between the tested conditions, the Zener-Hollomon parameter relates temperature and strain rate with stress:

$$Z = \dot{\varepsilon} \exp\left(\frac{Q}{RT}\right) = f(\sigma) \tag{2.1}$$

where $\dot{\varepsilon}$ is the plastic strain rate, Q the activation energy, R the gas constant and T the temperature [34]. The Zener-Hollomon parameter was initially developed for creep to describe the creep rate [107]. For this application, the activation energy represents the energy barrier for diffusion to occur. However, during dynamic recrystallisation two processes are active simultaneously: the nucleation of the grains by dislocation rearrangement and the growth grain via boundary movement. As these mechanisms require both, diffusion and dislocation glide the activation energy for the Zener-Hollomon parameter is more an empirical concept rather than a physical constant.

A recrystallization model should predict the fraction of the recrystallized material. By far the most common empirical descriptions of this microstructural characteristic is the Johnson-Mehl-Avrami-Kolmogorov (JMAK) equation. The JMAK model is used for the evaluation of the recrystallized fraction.

The JMAK formulation to determine the fraction of a phase transformation is given by:

$$\xi = 1 - \exp(-k \times t^n), \tag{2.2}$$

where k is the so-called Avrami coefficient, t the time and n the Avrami exponent. The initial assumptions are a constant rate in diminishing area by nucleation and growth of the grains. It enjoys great popularity amongst scientists due to its simple formulation [108–110]. However, in order to apply the model appropriately its assumptions should be pointed out [111]. Firstly, the nuclei are randomly distributed. Secondly, the nuclei formed have a constant growth rate. The last requirement is the constant growth rate of circular grains. During recrystallisation the ideal JMAK behaviour cannot be achieved due to numerous reasons such as recovery, variations in stored energy distribution, preferred nucleation sites and anisotropic grain growth [112]. With these restrictions in mind the equation was used for SRX [113], DRX [68] and MDRX [45]. The ongoing discussions about the value of the parameters show the necessity for physics-based models.

Physics-based formulations were developed for the nucleation process during recrystallization. The heterogeneous nucleation was modelled by a detailed description of microstructural events taking place [114, 115]. A critical dislocation density is calculated from the overall deformation conditions to determine the onset of nucleation. The nucleation rate for these models is assumed to be continuous rather than the site-saturated assumption of the JMAK equation [116]. Further growth of the nuclei is defined using an expression for the grain boundary velocity:

$$v = m \times p \tag{2.3}$$

with m being the grain boundary mobility and p the driving pressure [34]. The driving pressure p for a grain boundary is a function of the stored energy, capillary pressure, solute drag pressure and particle pinning [55]. The grain boundary mobility term includes temperature dependence and indirectly the crystallographic misorientation.

The disadvantage of these models is the lack of inclusion of crystallography and texture. Microstructural parameters such as grain size can only be accessed as an averaged value throughout the whole area. Therefore, the implementation of heterogeneous nucleation and grain growth cannot be done in a straight forward manner and, as such, the model loses its main benefit, efficiency.

2.4.2 Numerical continuum mechanical models

Even though constitutive equations describe the overall behaviour very well they are not capable of simulating localised events. Models with a higher resolution can handle heterogeneous events such as abnormal grain growth or site-dependent nucleation in a more efficient way. These mesoscale models can give insight into the complex phenomena during

recrystallisation. Various approaches were applied to recrystallisation processes at this length scale such as cellular automata [49, 117, 118], level set [119–121] and phase field [122, 123].

To perform cellular automata simulation the area of interest is discretised into a grid. The properties of each cell are characterised by state variables, e.g. dislocation density or crystallographic orientation. During the simulation the cell neighbourhood is analysed and may lead to an update of the cell. The governing evolution equations can be chosen without restraint and do not need to have a physical meaning. On account of the grid representing the structure there is no precise position of the boundary.

The level set approach directly tracks the interface of the evolving structure over time. A two-dimensional interface is expanded by a continuous function to a third dimension, being time not length scale. The shape of the interface at the current time step is defined by a plane, the level set, intersecting the three dimensional function. This gives a direct representation of the interface location. The driving forces can be user-defined and do not need to have a physical background. The level set method has a higher computational demand because of the direct interface tracking.

The phase field approach belongs to the class of diffuse-interface models in contrast to sharp-interface methods such as level set [124]. Diffuse interface models do not track the surface explicitly but rather have a smooth transition from one phase to the other. The underlying mathematical equations for the driving force are based on free energy definitions from thermodynamics. The diffuse interface causes an area which lacks in a clear allocation of the data points.

2.5 Summary

This chapter reviews the alloy system 718Plus which is used in this study. The microstructural changes during forging, primary recovery and recrystallisation were outlined as well as their applicability in low-stacking fault ccp alloys. A number of different recrystallisation mechanisms have been described alongside their application to relevant studies. Due to the lack of clear distinctions between the mechanism, interpretations and appropriate characterisation techniques, the field of recrystallisation suffers from contradictory observations. The influence of strain rate on dynamic recrystallisation is an example. Some materials, including 718Plus, were reported to show an increase in recrystallised fraction with strain rate, while the majority of alloys have an inverse behaviour of strain rate to recrystallised fraction. One part of the present work will address the difficulty of these recrystallisation concepts with the underlying mechanisms.

The role of second-phase particles on the recrystallisation of nickel-base superalloys has been analysed in IN718. Similar to DRX in single-phase alloys, the influence of precipitates is contradictory. Additionally, η phase in 718Plus has not been subject of investigation so far. High temperature compression tests on a multi-phase microstructure of 718Plus will focus on the recrystallisation mechanisms in the presence of a hard second phase.

In the light of imprecise usage of the different recrystallisation mechanisms the following definitions will be used for the upcoming analysis: static recrystallisation comprises the nucleation and growth of recrystallised grains after deformation; dynamic recrystallisation is the nucleation and growth of new grains during deformation; meta-dynamic recrystallisation labels the growth of previously recystallised grains after deformation due to stored energy in form of dislocations.

Chapter 3

Experimental methods

3.1 Material

The material used for analysing the initial stages of dynamic recrystallisation was as-received billet material from heat #M74M. It was produced by ATI Speciality Materials Ltd. through the triple melt process VIM-ESR-VAR and afterwards cogged to a constant circular cross-section of 229 mm. The chemical composition from the material received was analysed by the manufacturer ATI Speciality Materials Ltd. and given in Table 3.1.

These billets are identical to those used in disc forgings which makes them an ideal starting material for studying the process.

Part of this study was also to investigate the recrystallisation behaviour of 718Plus with η phase being present. Casanova et al. [16] published a time-temperature-transformation diagram on the precipitation kinetics of η for the wrought billet material similar to the one available for this study. The TTT diagram included information on the precipitation fraction depending on the sample location hence, the residual stresses, within the billet [16, 24]. The planned heat treatment was tailored to precipitate η above the γ' solvus temperature. From the TTT diagram the chosen heat treatment was 10 hours at 975°C followed by a water-quench to reach ~4 area% of η precipitation.

Table 3.1 Chemical Composition of 718Plus as-received billet material in wt%

	Ni	Cr	Mo	W	Co	Fe	Nb	Ti	Al	C	P	B
As-received billet	bal.	18.02	2.63	0.67	9.56	9.83	5.15	0.87	1.39	0.025	0.008	0.005

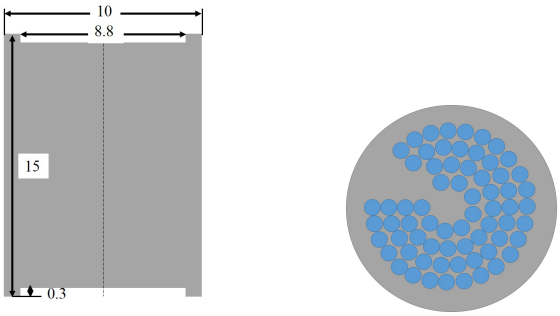

(a) (b)

Fig. 3.1 Rastegaev compression test samples: a) dimensions, b) extraction position billet.

3.2 Mechanical testing

Forging is simulated by uniaxial compression tests on Rastegaev samples. Cylindrical specimens with the dimensions 10x15 mm were machined with shallow pockets on the top and the bottom (Figure 3.1a). Their purpose is to fill them with glass lubricant to diminish the friction between sample and compression dies. The samples with the γ-η microstructure were tested without the recess. Subsequent validation of the test by shape determination proved to be within the limits set for a valid test (see Chapter 5 for details). Another sample geometry commonly used for compression tests are double-truncated cones. Double cone compression tests have the advantage that different strains and temperatures are reached within a single test. Therefore, the test matrix can be reduced. The disadvantage of a double cone specimen shape is the temperature and stress gradients in the cross-section. In contrast, a cylindrical sample has homogeneous testing conditions throughout the cross-section which helps in understanding recrystallisation parameters and the set up of a simulation model. Another issue of double cone tests are the flow curves obtained. Due to the heterogeneous distribution of the testing parameters in the cone as well as its shape, the flow curve is not representative of the microstructural changes associated with a single set of parameters.

The specimens for the Rastegaev compression tests were cut from the middle area of the billet cross-section as shown in Figure 3.1b. This area was analysed to have a homogeneous microstructure and is therefore an ideal section for testing [16].

The compression tests were carried out at the Advanced Forming Research Center at University of Strathclyde in Glasgow. The servo-hydraulic unit Zwick/Roell Amsler HA had a load capacity of 250kN and its flat compression dies were made of CMSX-4. Before the test, the dies were corrected to be parallel by compressing lead billets. The parallelism was adjusted so that the opposing platens were within a tolerance of ~0.04 mm. The machine was equipped with a three-zone furnace for high temperature tests. To ensure an isothermal testing

environment, the dies were heated to the same temperature as the sample. Three N-type thermocouples measured the furnace temperature to ± 5°C. Two were mounted in the top and bottom anvils and the third controlled the temperature of the test piece. It was attached close to the test piece at mid-height. The machine load train compliance was measured as a function of load at the temperatures: 850, 950 and 1025°C. Therefore, the dies were brought into contact and the load increased up to the estimated maximum testing value.

The specimen dimensions of each testpiece were measured before and after the test. With a caliper the initial diameter and height were taken with an inaccuracy of ± 0.02 mm. The measurement of the diameter consisted of four measurements in 45° intervals at the mid-height of the sample. The specimen height was measured four times between the recesses as well as three times at the total height. In the case of the cylinders without the pockets, only four measurements were taken in total. The same procedure was followed for acquiring post-deformation sample dimensions and all data given in Chapter 5 are average values.

Before the test, the compression dies were greased with boron nitride to decrease the friction between workpiece and plates. The samples for studying recrystallisation solely in the γ matrix which had the recesses machined at top and bottom received further lubrication. Delta Glaze Fb417 was filled into the pockets and left to solidify before testing.

A consistent test procedure was followed, outlined here. The sample was placed between the plates while the furnace was preheated to 650°C. At this temperature, the furnace was moved to the machine to encapsulate dies and specimen. The heating rate was 12°C min^{-1} to the desired temperature followed by a soaking time of 15 min. The strain rate was kept constant throughout the compression by the control software. After the test finished the sample was retrieved within a 5 s time window and quenched in cold water. A certain set of specimens received a 120 s hold time at the deformation temperature within the furnace before they were removed and quenched.

The purpose of the compression tests were to analyse dynamic recrystallisation during the forging process of a turbine disc. Hence, the temperatures considered for the tests are between 950 and 1025°C. These temperatures were slightly at and above the γ' solvus temperature. The forging window is preferred to be above the γ' solvus as the material is then softer and less load is required for the forge. Three strains and strain rates were chosen to investigate their influence on the recrystallisation. The selection was based on previous work conducted by Löhnert [14] on 718Plus. The compiled test matrix is listed in Table 3.2. Two different microstructures were tested, marked in the test matrix with 'x' for γ and 'o' for γ-η. In addition to the tests performed highlighting the DRX behaviour, some samples were kept in the furnace after the deformation for 120 s to analyse meta-dynamic recrystallisation.

Table 3.2 Test matrix compression tests with sample denomination for studying DRX

Strain [-]		0.4		0.8			1.2		
Strain rate [s^{-1}]		0.1	1	0.01	0.1	1	0.01	0.1	1
T [°C]	950		x o			x/x120 o	x/x120 o/o120	x o	x/x120 o/o120
	975	x	x	x/x120 o/o120	x	x/x120 o	x/x120 o/o120	x	x/x120 o/o120
	1000				x	x	x		
	1025			x			x		

These sample pairs are defined in the table with '*/*120' where the '*120'-sample had the additional anneal.

Three additional specimens were tested at 850°C with a γ-γ' microstructure with the strain rates of 0.01, 0.1 and 1s^{-1}. With the maximum available load of the testing equipment they were strained to ~0.65. The lower the temperatures the more strain is required to dynamically recrystallise a microstructure. Hence, compressing to only a strain of 0.4 at 850°C was expected to achieve hardly any recrystallisation. As the maximum strain did not reach any of the other two categories for analysing DRX (0.8 or 1.2), the tests were solely used for extracting mechanical properties.

Recrystallisation depends on the initial microstructure. Therefore it was essential, to characterise the microstructures before the compression. Three different samples were used to reproduce the pre-test conditions. Firstly, the as-received microstructure taken from one of the Rastegaev cylinders. Secondly, a sample from an η-heat treated cylinder. Thirdly, the microstructure obtained after the heating-up cycle of the compression test just before the deformation. To achieve this microstructure, one of the testing cylinders received the exact same heat treatment of the testing-cycle. The sample was placed in a furnace pre-heated to 650°C and then heated up to one of the testing temperatures, 975°C, with 12°C min^{-1}. Upon reaching 975°C, the sample was kept in the furnace for a 15 min dwell time before extracted and quenched in ice-water.

3.2.1 Sample preparation

The samples were characterised with various techniques in electron microscopes. Different microscopes and methods required specific sample preparation routines described in the following.

For the microstructural analysis in a scanning electron microscope (SEM) the samples were cut in half parallel to the deformation direction and mounted in conducting bakelite.

Subsequently they were grinded and polished to 0.25 µm and finished with a 1:5 solution of 0.05 µm colloidal silica in water as oxide polishing suspension. This surface quality was required to successfully analyse the samples with electron backscatter diffraction technique. To reveal the morphology of the η precipitates, some samples were electro-chemically etched using 10% orthophosphoric acid in distilled water and a voltage of 3V.

A sample for studies at the transmission electron microscope (TEM) needs to have a suitable thin area to allow electrons travelling through the specimen. Such thin specimens can be either produced by a technique using a focused ion beam (FIB) or by following an electro-polishing route. FIB is similar to scanning electron microscopy but using an ion rather than an electron beam. Where the ion beam hits the surface of a material, it sputters surface atoms hence, leaving a surface damage. This technique can be used to erode TEM specimens from bulk material. A TEM specimen produced by FIB has a constant sample thickness throughout the visible area and therefore excludes artifacts from thickness variations in the TEM. The second common option to make TEM specimens is to produce a transparent area in a thin disc by electro-polishing or ion milling. Both follow the principle to create a parabola on a slice of material eventually leaving a hole in the middle. The area around the hole is ideally thin enough to image it in TEM. In comparison to FIB samples, these specimens provide a bigger surface area to analyse. Hence, it is easier to determine if certain features are statistically significant or not. In consideration of the heterogeneity of partially recrystallised microstructures, the electro-polishing route was chosen for receiving TEM slices.

The electro-polishing technique required thin discs to be extracted from the bulk material. Two different sample orientations were cut from the deformed cylinders: one being parallel to the compression axis and the second being perpendicular to the axis. Circular samples with a diameter of 3 mm were spark eroded from slices with a thickness between 0.15 and 0.2 µm taken from the sample cross-section. Finally the specimens were electro-polished to create an area thin enough for electron transmission. A Tenupol-5 twin-jet electropolishing unit from Struers was used with 10% perchloric acid in methanol at ~-5°C with a voltage of ~18 V.

3.3 Microstructural analyses

The microstructures of the samples were examined by means of secondary and backscattered electrons, electron backscattered diffraction (EBSD) in an SEM and using a conventional transmission and scanning transmission electron microscope.

3.3.1 Secondary and backscattered electron imaging

Secondary electrons (SE) are created in a sample by inelastic scattering events of the incoming electron beam. The imaging contrast is related to the quantity of the electrons detected. An area facing the detector emits more electrons which reach the detector than a surface facing away from it. Hence, the imaging contrast is directly related to sample topography. For the same reason, only a small sub-surface volume contributes to the overall signal.

Elastic scattering of the incident beam produces backscattered electrons (BSE). These are high-energy electrons and stem from a larger volume of the bulk sample. After an elastic scattering event with a heavy element, the electron can travel further than if it hit a light element. Thus, the contrast of a BSE image represents the atomic number Z. Another way of forming an image in BSE mode is electron channeling contrast imaging (ECCI). This is formed by the electron density wave interacting with atoms and the spaces in between. Electrons can travel further into the sample when the Bragg condition between incoming beam and lattice plane is fulfilled and thus not contribute to the signal.

BSE images were used to quantify the η content within the microstructure to correlate them with EBSD scans at the exact same position and angle relative to the loading axis. Special care was taken to align the sample horizontally to the detector. As η contains more Nb which has a high atomic number, it was possible to distinguish it from the γ matrix. On the contrary, the heavily deformed samples showed complex orientation gradients due to the electron channeling contrast which made it impossible to use automatic indexing. The BSE images were printed out and the visible η precipitates redrawn by hand then being scanned in again. With these scans it was possible to use ImageJ software to post-process microscopy images [125]. The scanned images were converted into a binary format to set a threshold for the distinction between precipitate and matrix. After noise reduction and the removal of single pixels, the precipitates were automatically analysed in terms of their shape, size and angle.

SE and BSE imaging was carried out in a Gemini300 from Zeiss.

3.3.2 EBSD

EBSD offers an efficient way to analyse quantitative crystallographic orientations in a microstructure. It takes advantage of the formation of ‘Kikuchi-patterns’ from elastically scattered of electrons. These electrons can hit a lattice plane and fulfill the Bragg condition. Because they arrive from different directions, they span up a cone known as ‘Kossel cone’. A Kikuchi line is formed when the Kossel cone intersects with the EBSD-detector surface. A Kikuchi pattern is the sum of all Kikuchi lines, i.e planes, which is unique to each crystal

orientation. This crystallographic information is collected with the detector and further processed to index the orientation of a given sample. Large interaction volumes are needed to get a good signal-to-noise ratio. This is achieved by tilting the specimen.

The EBSD analysis of the γ specimens was carried out in a field emission gun scanning electron microscope (FEGSEM) XL30 from Philips. The acceleration voltage used was 25 keV, working distances varied between 10 and 15 mm and a 70° tilt. In order to examine a representative size of interest large area scans were conducted with a step size of 0.15 µm. The γ-η samples were analysed in a GeminiSEM 300 from Zeiss. Both microscopes were equipped with an EBSD detector from Oxford instruments and indexed with the AZtec software from Oxford Instruments.

EBSD on bulk samples suffer from a minimum spatial resolution due to beam scattering in the material. A method to circumvent this issue is transmission Kikuchi diffraction (TKD) [126]. Electron transparent samples, such as TEM-samples, are used with a conventional EBSD camera which collects the transmitted signal rather than the backscattered. The advantage of this technique is a decrease in the spread of the inelastically scattered electrons leading to a minimal spatial resolution of ~10 nm. The TEM-sample was mounted in a TKD-holder and tilted to 20°. The GeminiSEM 300 microscope was operated with 25 keV and the maximum working distance of the different samples was 2.6 mm.

Post-processing of the images gained from EBSD was carried out with Oxford Instruments' HKL Channel 5 Tango software and the MTEX toolbox for MATLAB [127]. For zero solutions a minimum of five neighbouring pixels were considered for the closest match. Separate grains were defined by a minimum of 10 pixels and a misorientation angle of 15°. For the grain size measurement twins were not considered as a grain boundary, hence only boundaries with a misorientation angle $>15°$ marked the circumference of a grain. The grain size was calculated by the area equivalent circle size [128]. Grain boundary (GB) angles were divided into three groups: low angle grain boundaries with $\alpha<15°$, high angle grain boundaries with angles $>15°$ and twin boundaries defined by a misorientation of 60° about the $\langle 111 \rangle$ axis with a tolerance of 8.66° following the Brandon criterion [129]. The boundaries were quantified measuring one point per boundary. This was toevaluate the twin formation conditions rather than their growth kinetics. With the different progress stages in recrystallisation, the average grain size between the samples changes hence the ratio of twin length to HAGB length. This issue can be circumvented by counting the amount of twins than its length.

The degree of recrystallisation was calculated with a routine built with the MTEX toolbox in MATLAB. Deformed grains contain of a high dislocation density to accommodate the stress. These geometrically necessary dislocations (GND) provoke a change in the

crystallographic orientation of the lattice. The grain orientation spread (GOS) was employed to define grains with a high amount of residual strain to distinguish them from recrystallised grains. The GOS is defined as

$$GOS = \sqrt{\frac{1}{N-1}\sum_{i=1}^{N}(\overline{\Theta_g} - \Theta_{gi})}, \tag{3.1}$$

with $\overline{\Theta_g}$ as the mean orientation of grain g, Θ_{gi} being the orientation of point i in grain g and N as the number of points in the grain. Hence, a high GOS value indicates a large orientation spread within the grain resulting from a high residual strain within the grain. Annealing twins form during recrystallisation cause a change in orientation and hence increase the GOS value. Therefore, the definition of a grain for calculating the recrystallised fraction considered twins along with high angle grain boundaries as grain borders.

The size of the analysed area was kept constant throughout the samples. Hence, microstructures with larger recrystallised grains have a higher standard deviation. As a result, recrystallised fraction within ~5% cannot be considered as significant changes.

3.3.3 TEM

A transmission electron microscope offers a higher resolution in comparison to an SEM because it typically operates at higher voltages between 80 and 200keV [130]. The higher voltages are needed for the electrons to travel through the sample and reach the detector. The image in the TEM is usually acquired from elastically scattered electrons of the direct beam. Imaging using the direct beam is termed bright-field (BF) and dark-field (DF) if a diffracted beam is chosen. For obtaining images in the TEM the intermediate lens focuses on the image plane of the objective lens while for obtaining diffraction patterns (DP) it focuses on the focal-plane.

The beam for conventional TEM is usually aligned to be parallel. In a scanning transmission electron microscope (STEM) the beam is focused to a small spot and then moves across the specimen. The detectors collect the diffracted electrons at different angles, for example the high angle annular dark field (HAADF) detector for angles more than 50 mrad [130].

Electrons from the incoming beam can also produce X-rays when they hit an electron from an inner atomic shell. This mechanism is utilised for a technique called energy dispersive X-ray spectrometry (EDS or EDX) to quantify elemental compositions in a specimen. The strength of the EDX signal is determined by the count rate which depends on the acceleration voltage. Within the X-ray spectrum, some elements have similar X-ray emission peaks

depending on the original shell the electron was knocked out. With these two limitations in mind, one must be careful when acquiring and interpreting EDX data.

In the present work, a JEOL 200CX field emission gun operated at 200kV was mainly used. For EDX data an Osiris (S)TEM from FEI was employed at 200kV.

Chapter 4

Dynamic and meta-dynamic recrystallisation in 718Plus

The microstructural evolution during forging is directly related to dynamic recrystallisation. Dynamic recrystallisation can lead to a partially recrystallised microstructure with small recrystallised grains alongside larger deformed ones. Such heterogeneous areas influence the local mechanical properties of a component. To generate more uniform microstructure, the parameters guiding dynamic recrystallisation in 718Plus need to be investigated.

The present chapter analyses the microstructural changes during dynamic and meta-dynamic recrystallisation of 718Plus. Two different microstructures were produced and tested: a γ and a γ-η. In the first section the initial state of the material before the tests will be quantified. A finite element (FE) study of the compression itself was performed to gain insight of the effective forging parameters in the samples. In the second part of the chapter the influence of the forging parameters on the kinetics of DRX and MDRX in the γ microstructure will be analysed. The final part discusses the results of recrystallisation in the γ-η samples.

4.1 Initial characterisation

An accurate characterisation of the initial microstructure is key to interpret its changes after testing. During the compression, the sample experiences local changes in temperature, strain and strain rate to the overall set testing parameters. These variations can be modelled with the FEM simulation tool DEFORM® 2D.

4.1.1 Pre-deformation microstructure

Each testing cycle included a heat-up and dwell time before the actual compression. As an example, the heating up to a test temperature of 975°C lasted 27 min (650°C to 975°C at 12°C/min) which was followed by a dwell time of 15 min adding up to 42 min at elevated temperature. To accommodate for any grain growth during this period a reference sample was produced. This sample was one out of the cylindrical samples prepared for the mechanical testing ensuring the same initial microstructure as the specimens tested. The specimen was given the exact same heat treatment as the testing cycle in a high temperature furnace. After the heat-up and dwell the specimen was removed from the furnace and water quenched.

The second microstructure to test was designed to contain η precipitates. As the as-received microstructure was η-free, a heat treatment was given according to a time-temperature-transformation (TTT) diagram for 718Plus [16]. A precipitation area fraction of 4 area% was chosen. Such a small area fraction of η makes it possible to compare local effects due to the presence of particles with precipitation-free area. The defined heat treatment was at 975°C for 10 hrs followed by a water quench. The η morphology depends on the thermo-mechanical history of the material and can range from small blocky to a longer and thinner lamellar structure. Lamellar η is expected to precipitate in areas which experienced lower strains in previous manufacturing steps while blocky particles are found at the outer rim of the billet [25]. Hence, the heat treatment of the specimens from the middle section was expected to be lamellar with few blocky η. A reference sample was produced from one of the testing cylinders to analyse the microstructural changes after the heat treatment and before the actual compression test.

Microstructural analysis of the reference samples

Figure 4.1 shows the microstructures of the as-received state on the top, the η-free reference sample for the test cycle left and the specimen after the η heat treatment on the right. The inverse pole figure (IPF) maps are from the out-of-plane direction from EBSD scans being perpendicular to the cylinder height. The backscattered electron (BSE) image of the η-containing microstructure is just below the IPF map of the corresponding sample. Grain boundaries with a misorientation angle $\alpha > 15^\circ$ are drawn in black lines and the first-order twin boundaries are in red.

Between the as-received material and the test-cycle heat treatment there are no signs of change in texture or grain boundary appearance visible. In contrast, the η heat treatment led to a more serrated grain boundary structure caused by the precipitation of η.

The η morphology achieved can be seen in the BSE image highlighted in orange. The contrast between precipitate and matrix was weak hence the particles were redrawn to

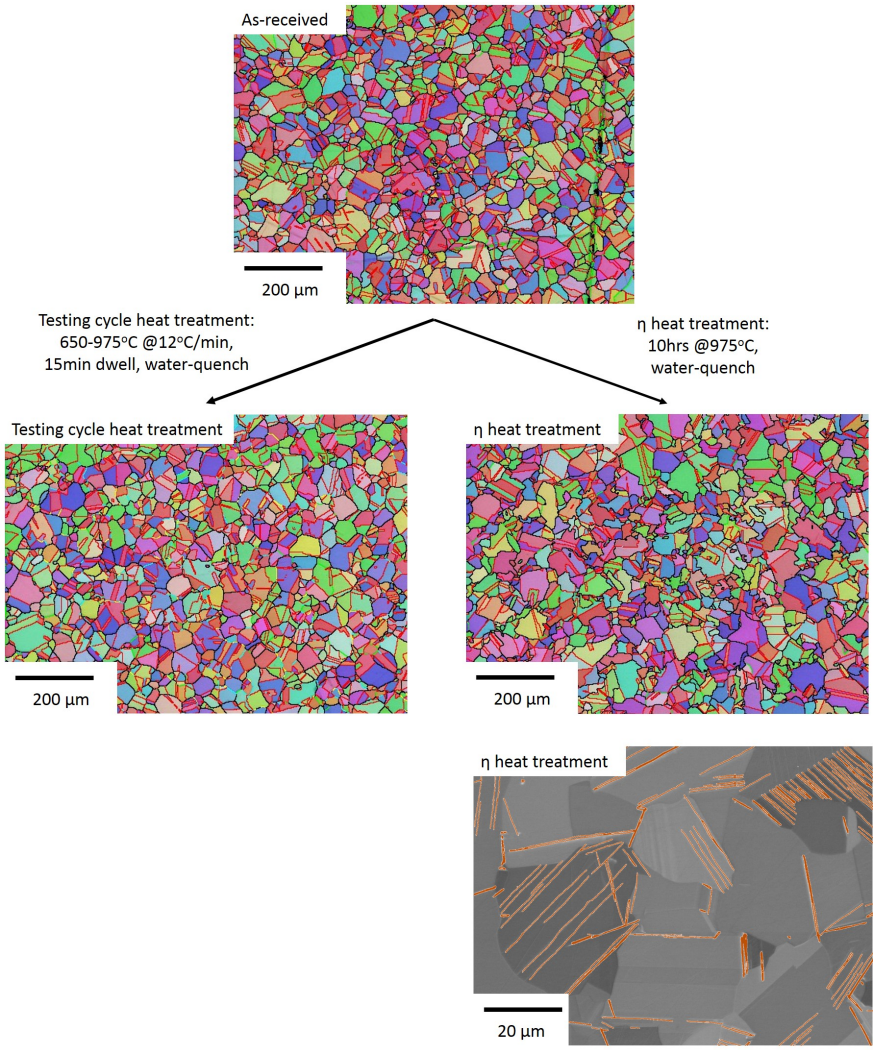

Fig. 4.1 Microstructures in the as-received condition, after the test cycle heat treatment and the η heat treatment

improve the visibility. As expected, η precipitated in long and thin lamellae with a few smaller ones at the grain boundaries. The percentage of precipitates in the matrix was calculated to be 5.0 area%.

The grain size of the as-received billet material was 41 µm and after the test-cycle heat treatment 43 µm. This slight growth of the grains is due to the lack of grain boundary pinning η precipitates. Based on the minor changes during the test-cycle heat treatment and the much longer η heat treatment, the influence of the testing cycle on the η-containing samples was considered to be negligible. The grain size after the 10 hr η heat treatment 36 µm. The shrinkage of the grains could be due to static recrystallisation of grains containing residual stressesfrom the manufacturing. The grain size of the as-received billet material was 41 µm

and after the test-cycle heat treatment 43 µm. This slight growth of the grains is due to the lack of grain boundary pinning η precipitates. Based on the minor changes during the test-cycle heat treatment and the much longer η heat treatment, the influence of the testing cycle on the η-containing samples was considered to be negligible. The grain size after the 10 hr η heat treatment 36 µm. The shrinkage of the grains could be due to static recrystallisation of grains containing residual stresses from the manufacturing.

4.1.2 Post-deformation microstructure

After the compression tests, only the samples deformed at 850°C maintained the γ' precipitates. In the samples tested at all other temperatures γ' dissolved completely and even upon quenching the γ matrix was the only detectable phase. This was expected because of the high Nb content in 718Plus [11]. Figure 4.2 shows the TEM diffraction patterns on the $\langle 110 \rangle$ zone axis of the polycrystalline RR1000 and 718Plus. Both patterns were kindly taken by R. Krakow. RR1000 clearly shows the expected γ' superlattice diffraction spots. In 718Plus on the other hand, the γ' diffraction spots after the compression tests were missing. The electro-chemical polishing of TEM slices can lead to a preferential etching of γ' leaving behind a γ microstructure with characteristic dents and a single-phase diffraction pattern. This effect could be observed in thin regions of TEM samples in the as-received state and tested at 850°C. However, specimens deformed at any higher temperature were clearly free from γ' which is assumed to have dissolved during the test and been suppressed from re-precipitation by the fast quench.

4.1.3 FEM modelling of the compression test

DEFORM® 2D is a process simulation software on the basis of finite element method [131]. It is a standard tool to model forming processes such as forging. The software was used to simulate the high temperature compression tests of the cylindrical samples.

Model set-up

An axisymmetric model of the test piece and the compression dies was generated. The anvils were considered to be rigid while the specimen was attributed temperature dependent elasto-plastic properties extracted from the ATI® 718Plus™ Data Sourcebook [132]. The friction coefficient between sample and dies was set to 0.22 according to the software recommendation for high temperature compression with a lubricant. The convection coefficient between components and environment was set to 0.02 $\frac{W}{s^3 K}$. Specimen, dies and environment were set to the respective test temperature. For the control of the strain rate various options

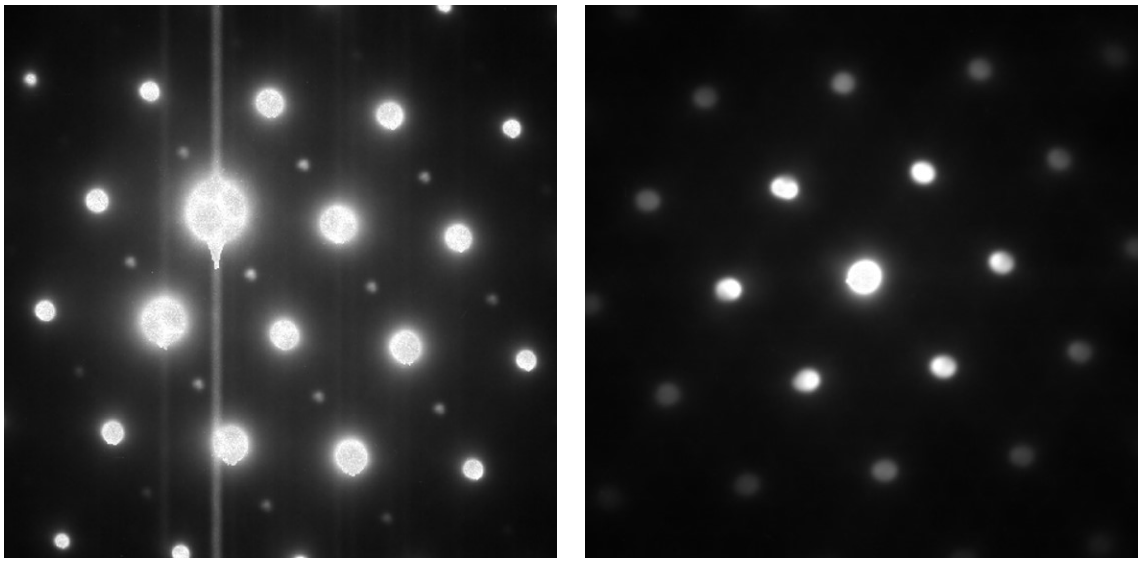

(a) (b)

Fig. 4.2 TEM diffraction pattern on the $\langle 110 \rangle$ zone axis of (a) RR1000 with γ' superlattice diffraction spots (b) 718Plus after deformation at 975°C. Image courtesy R. Krakow.

were tested and their influence on the final results. One of which was to use the actual die speed with lateral movement of the die recorded during the test. However, the difference between these results and a constant parameter were minor and did not justify the additional effort.

Results FEM simulation

Figure 4.3 presents the distribution of temperature, strain and strain rate at the final reduction for a specimen deformed at 975°C, 0.8 strain and $1s^{-1}$. The chosen strain rate is the highest one in the tests hence the results represent the upper extreme. At these conditions, the temperature in the centre increases from 975°C at the beginning by 155°C to 1130°C. Considering the strain rate in this area it reaches $3.3s^{-1}$ which is a three-fold increase of strain rate measured by the test equipment. Similarly to temperature and strain rate, the effective strain achieved in the middle of the sample is calculated to 1.3 which is a 60% increase. The dramatic rise in temperature can be attributed to adiabatic heating effects as well as the high strain rate achieved in the centre.

Besides the change to the set conditions of all three test parameters inside the specimen, a gradient of the values is visible throughout the sample. As an example, the distribution of strain varies from 1.3 in the middle to 0.5 at the rim. Based on these calculations special attention will be paid to take the EBSD scans from the same location to ensure a comparability of the results.

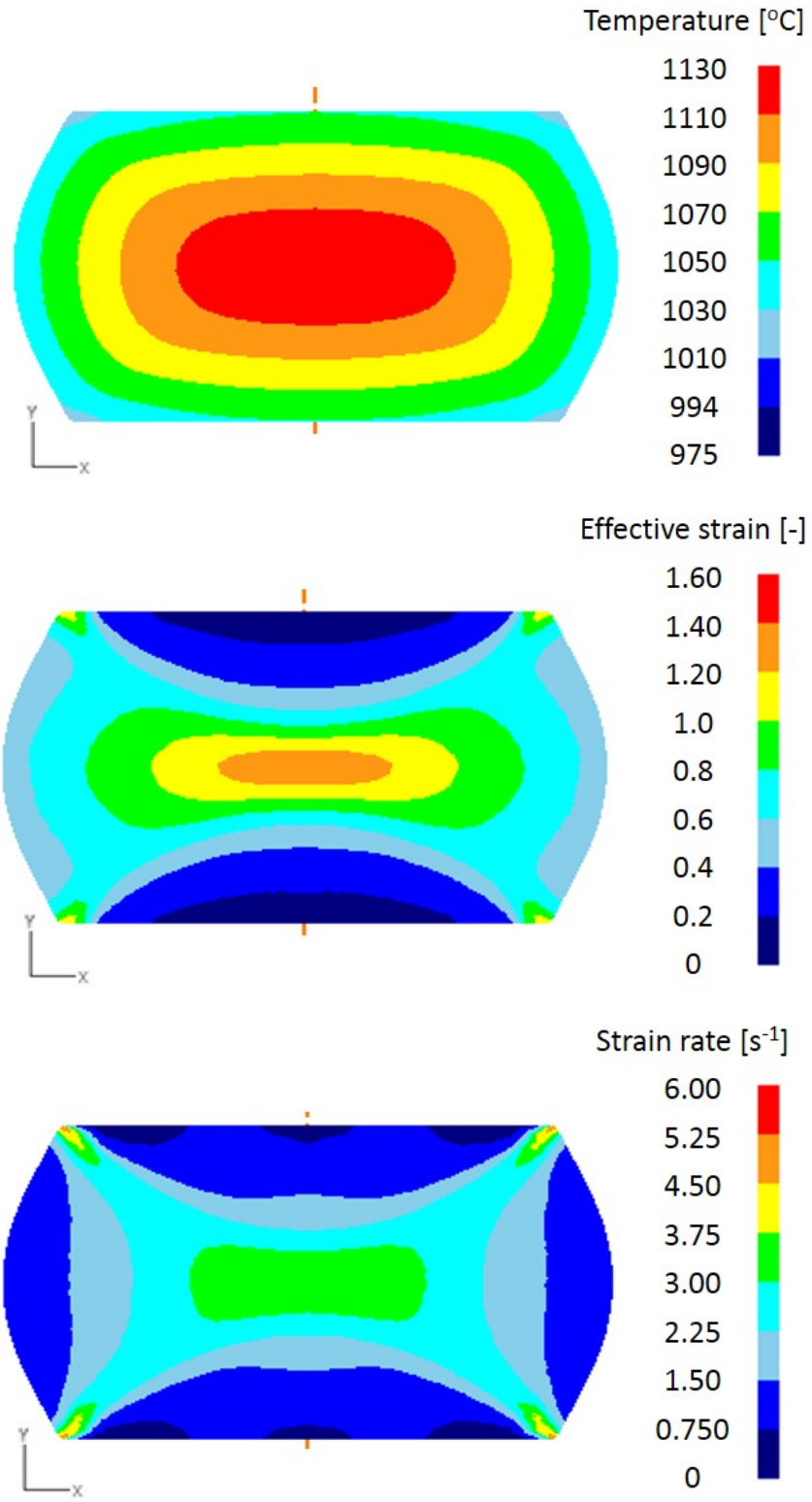

Fig. 4.3 FE analysis for a cylindrical sample compressed to a strain of 0.8 with $\dot{\varepsilon}$=1s^{-1} and at 975°C

The rise in temperature with strain and strain rate in the centre of the specimen are shown in Figure 4.4. Lower strain rates of 0.01 and $0.1s^{-1}$ lead to a core temperature in the sample of 977 and 1000°C. For the highest strain rate of $1s^{-1}$ the calculated temperature in the centre rose to 1130°C.

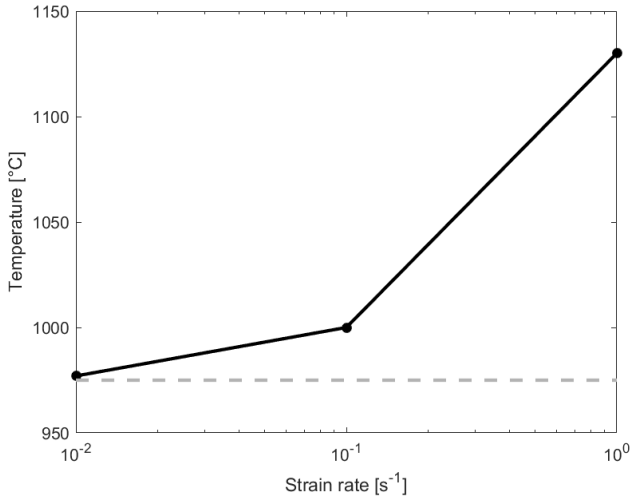

Fig. 4.4 FE-results of the temperature in cylinder core after compression at 975°C and a strain of 0.8 at all tested strain rates

In view of the results presented of the test values inside the specimen a few points should be made. Firstly, comparability with published studies are still valid. The equipment and procedure used is identical or similar to experimental methods of reports on dynamic recrystallisation [45, 43, 63]. Hence, the samples have experienced analogous conditions. Secondly, analysing the influence of a single parameter on recrystallisation can be performed. One of the main aims of this study is the individual impact of each forging parameter on microstructural changes. As great care will be taken in the selection of a representative area it is assured that the parameters which are are kept constant have the same value in the microstructure. Thirdly, the variation of the test values throughout the sample is less than for a double-cone sample geometry. Double-cone samples can achieve strain rates ranging from 0 to $25s^{-1}$ between rim and centre [93]. Hence, the overall material properties from the cylindrical specimens can be used for flow curve modelling.

The deformation parameters used throughout the thesis are the nominal values at which the samples were tested.

4.2 Recrystallisation of the η-free microstructure

Understanding the parameters governing dynamic and meta-dynamic recrystallisation of 718Plus is important to tailor the forging process for the required purpose. The results from the compression tests of the η-free microstructures will be presented in terms of the testing parameters and their influence on dynamic and meta-dynamic recrystallisation.

4.2.1 Dynamic recrystallisation

The recrystallised microstructure

Dynamic recrystallisation was studied in the samples which were removed from the furnace within 5 s after deformation. Figure 4.5a shows the inverse pole figure (IPF) maps in out-of-plane direction for the specimen tested at 975°C, ε=0.8 and $\dot{\varepsilon}$=1s^{-1}. The scan was taken parallel to the compression axis. The IPF map gives information about the crystallographic orientation of each pixel with respect to the normal direction. The colour key for this and all other IPF maps in this report are either found in the upper left or right corner of the image. In this example, the orientation varies within large grains indicated by the change in colour. An orientation gradient can only be achieved by dislocation accumulation, therefore this provides an indicator for high internal strains. In contrast, the smaller grains at the boundaries of the deformed grains mainly show a homogeneous orientation throughout. These grains exhibit fewer geometrically necessary dislocations as they have nucleated and grown at a later stage of the compression test.

Figure 4.5b presents grain boundary misorientation angles from the as-described sample. Black lines represent high angle grain boundaries (α>15°), green lines low angle grain boundaries (α<15°) and red lines highlight twin boundaries defined by a misorientation of 60° along the $\langle 111 \rangle$ axis with a tolerance of 8.66° according to the Brandon criterion [129]. The microstructure of the sample reveals the necklace structure typical for dynamic recrystallisation [34]. Different stages of recrystallisation can be detected in this sample keeping in mind that the actual microstructure is three dimensional and features presented could result from a sectioning effect. If after sectioning a grain boundary only reveals a single layer of recrystallised grains it does not necessarily have a single layer in 3D due to grain boundary curvature. However, some grain boundaries show several layers of recrystallised grains (red circle) while others only have a single layer (green circle). The black arrows indicate serrated grain boundaries formed by strain induced boundary motion (SIBM) as a nucleation mechanism. In the region circled in black the initial deformed grains have been fully consumed by recrystallised ones. The micrograph has a high density of annealing twins

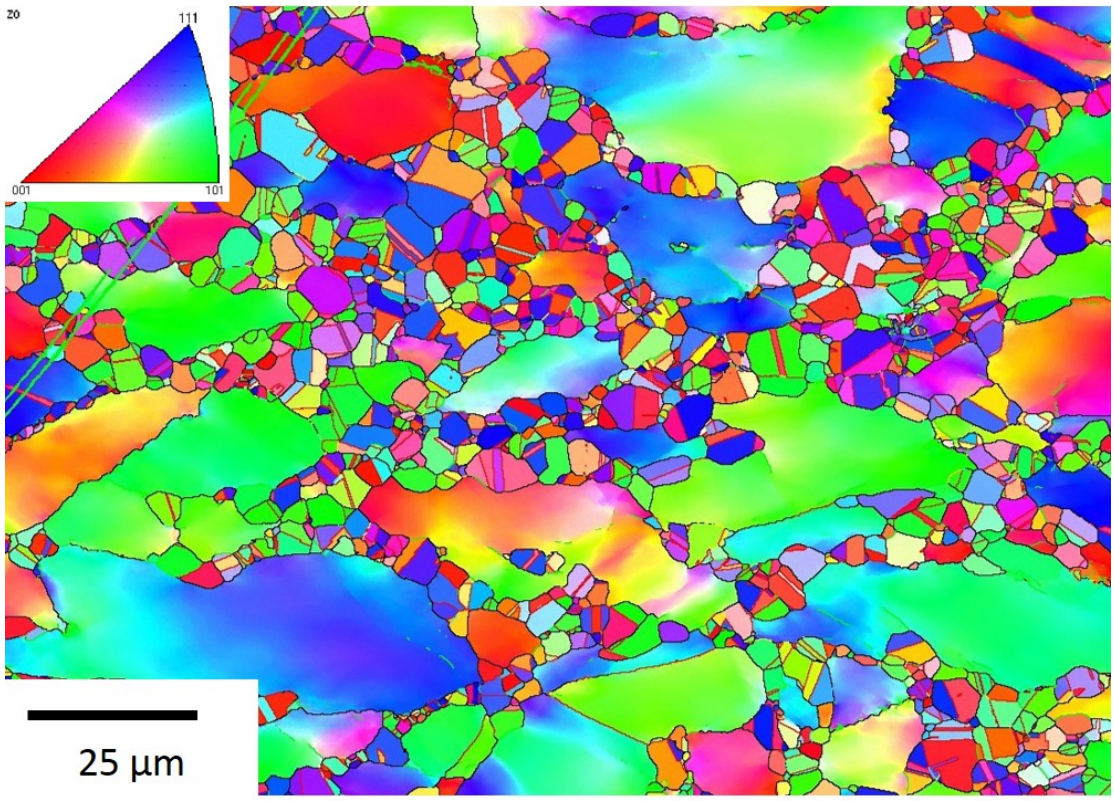

(a) Inverse pole figure in the perpendicular to the compression axis.

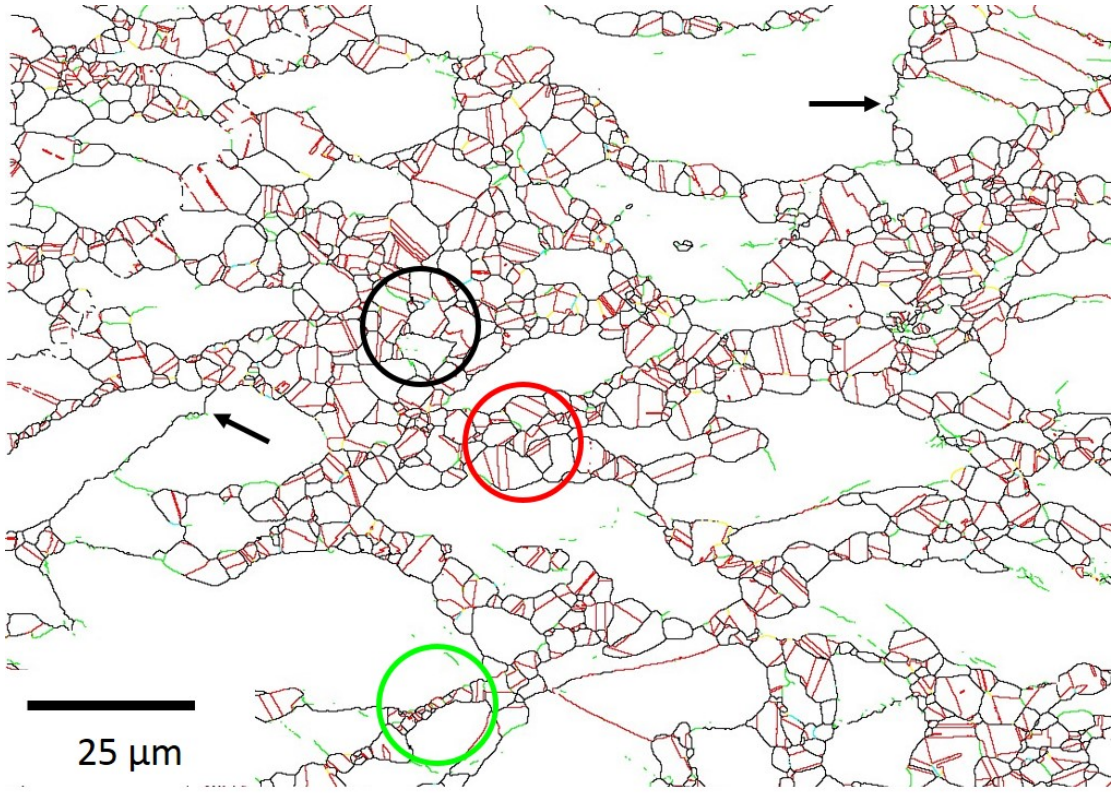

(b) Grain boundary misorientation map with HAGBs in black, LAGBs in green and twins marked in red. The areas in the circles refer to different stages during DRX. The arrows indicate grain boundary bulging.

Fig. 4.5 Partially recrystallised microstructure of a sample tested at 975°C, $1s^{-1}$and a strain of 0.8

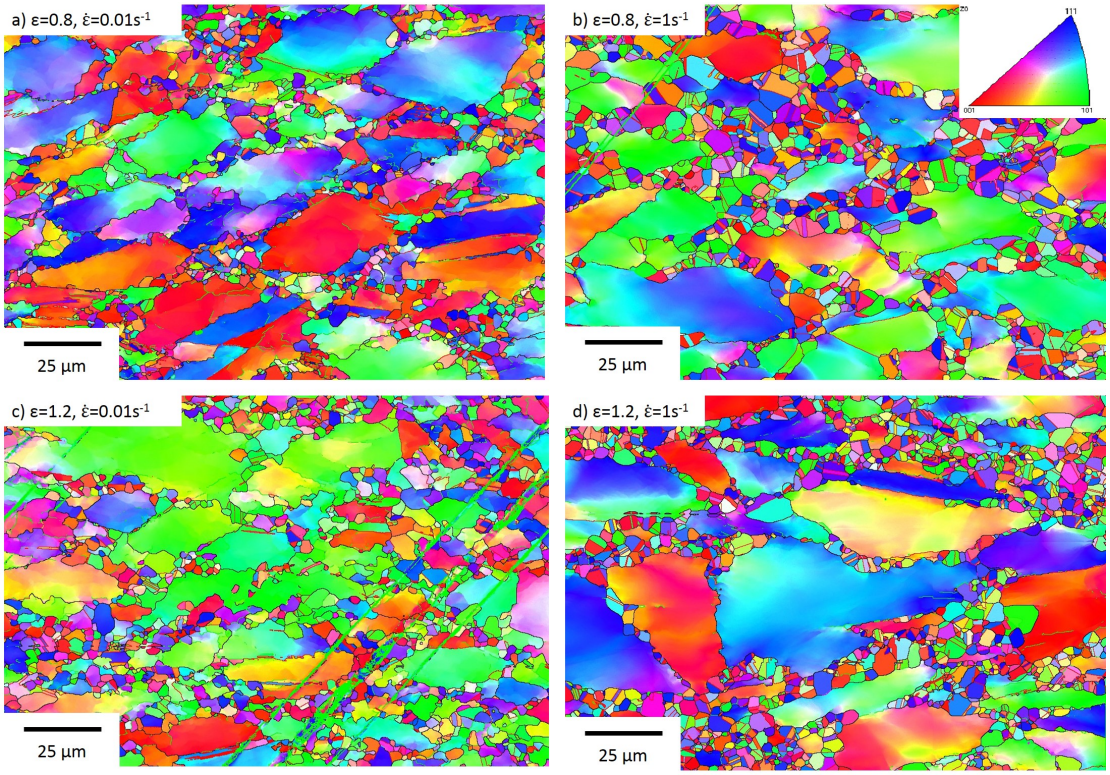

Fig. 4.6 IPF maps of samples deformed at 975°C at varying strains and strain rates.

within the recrystallised grains. In the partially recrystallised microstructure of the specimen the serrated grain boundaries are flanked with low angle grain boundaries, another indicator for the development of nuclei.

Recrystallisation fraction

The influence of forging parameters strain and strain rate on the microstructure is shown in Figure 4.6. The IPF maps were taken from samples deformed at 975°C at two strains and strain rates. Increasing the strain from 0.8 (top row) to 1.2 (bottom row) do not have a noticeable effect. However, the images in the left column appear to have different microstructural characteristics than those in the right column. The samples compressed with a strain rate of $0.01s^{-1}$(left column) have a wavy and serrated grain boundary structure. This effect can be seen for recrystallised as well as non-recrystallised grains. In contrast, the higher strain rate of $1s^{-1}$ results in recrystallised grains with smooth grain boundaries.

The orientation spread within a grain in the IPF map can be used to distinguish between recrystallised and deformed grains. The grain orientation spread (GOS) explained in Chapter 3.3.2 is employed to calculate the recrystallised fraction. Two different ways exist to use the GOS for determining if a grain is considered to have recrystallised. Firstly, with a

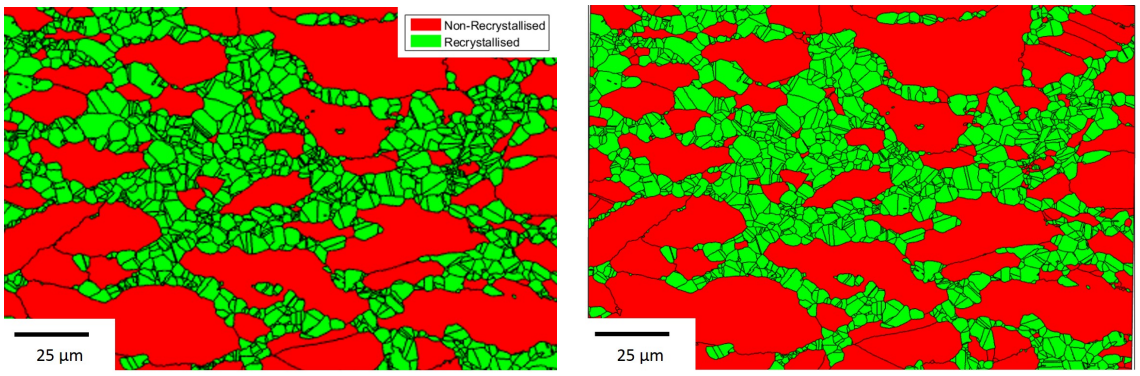

(a) Fixed GOS value 1.2° [108] (b) GOS acc. to Gazder [133]

Fig. 4.7 Partially recrystallised microstructure determined by different GOS values

fixed pre-defined threshold value for all micrographs. If the GOS value of a specific grain exceeds this value it is considered as recrystallised. An alternative to using a fixed GOS value for distinguishing between recrystallised and deformed grains was described by Gazder et al. [133]. Their threshold value changes with each microstructure and is based on the 'normalised cumulative misorientation distribution'. Therefore, the calculated GOS of each grain is plotted against its occurrence in the micrograph considered. The envelope of this distribution is drawn on to define the GOS value for this specific case. The misorientation at which the gradient of this curve reaches 1 is used as the threshold value for the GOS. This has the advantage of adjusting for varying amounts of stored energy due to alloy composition or processing [133]. For specimens in this study with a recrystallised fraction below 0.5 the GOS value after Gazder was ~0.8° while higher recrystallised samples had an average value of ~0.4°. The recrystallised fraction between the fixed GOS value of 1.2° [108] and the varying GOS calculation changed only slightly. In the samples analysed, the cut-off value estimated by the approach from Gazder was consistently below 0.9°. It was not used for further analysis because the difference in the calculated recrystallised fraction was well below 10%. Figure 4.7 presents the recrystallised area calculated with a fixed GOS and according to the method developed by Gazder et al. A comparison with values in the literature is an additional benefit of using a fixed GOS value. Hence, all further samples were analysed with a GOS value of 1.2°.

The recrystallised fraction X_{RX} for all samples tested, calculated with the constant GOS value of 1.2°, is listed in Table 4.1. The table consists of the values after immediate quench of the samples.

As mentioned in Chapter 3, the compression tests at 850°C are primarily used for evaluating the mechanical properties of a γ microstructure because of the low expected recrystallised fraction at these conditions. The assumption was found to hold true with

the cylinders deformed with strain rates of $0.01s^{-1}$ achieving an X_{RX} of 3%. At a strain rate of $1s^{-1}$ the cylinder experienced severe shearing making the test invalid (see details in Chapter 5). The effect of the shearing resulted in a highly heterogeneous microstructure with recrystallised fractions between 0 and 49%. Given all the reasons above, the specimens at 850°C will not be considered any further in their contribution to understanding DRX in 718Plus during forging.

The temperature of the compression tests was varied between 950 and 1025°C. For the samples deformed to a strain of 1.2 with $0.01s^{-1}$ the recrystallised fraction gradually increased with temperature from 14% at 950°C, 36% at 975°C, 46% at 1000°C and finally to 59% at 1025°C. A similar observation can be made at a higher strain rate of $1s^{-1}$ where the X_{RX} rises from 35% at 950°C to 55% at 975°C. The positive influence of temperature on the recrystallised fraction is consistent at all strains and strain rates.

The effect of strain on recrystallisation in 718Plus will be discussed on the specimens deformed at the intermediate strain rate of $1s^{-1}$ and at 975°C. For this condition all three strain levels 0.4, 0.8 and 1.2 were tested. A strain of 0.4 resulted in 15% of the area covered with recrystallised grains. Doubling the strain to 0.8 raised the recrystallised fraction to 44%. A further increase in strain to 1.2 left 55% of the full micrograph forming new grains. A similar pattern can be observed for other temperatures and strain rates, namely the increase of recrystallised fraction with strain.

Turning now to the influence of strain rate on recrystallisation, the picture is not as clear as for temperature and strain. Considering tests performed at 975°C and a strain of 1.2 the recrystallised area increases slightly from 36% at $0.01s^{-1}$ to 38% at $0.1s^{-1}$and 55% at $1s^{-1}$. The increase in recrystallised fraction with strain rate is consistent with testing at 950°C. However, at a temperature of 975°C and a strain of 0.8 the recrystallised fraction decreases between the strain rates of 0.01 and $0.1s^{-1}$. At $0.01s^{-1}$ it is 23%, but almost halves at $0.1s^{-1}$to 12%. Interestingly, a further increase in strain rate raises the recrystallised area to 44% this being even higher than at the starting strain rate. While the effect of strain rate on recrystallisation kinetics is ambiguous for lower strain rates, the highest strain rate of $1s^{-1}$ is consistently the peak value.

Grain size

The average grain size of the recrystallised grains in each sample is presented in the bottom half of Table 4.1. In general, the evolution of the grain size follows the recrystallized area, the grains growing larger with higher recrystallized fraction. However, the influence of strain rate has a different trend. The grain size of the specimes tested at $0.1s^{-1}$ is consistently smaller than at $0.01s^{-1}$. However, the recrystallised fraction for these samples increased with strain rate in two cases and decreased for one condition.

Table 4.1 Recrystallised fraction and average recrystallised grain size with standard deviation.

Strain [-]			0.4		0.8			1.2		
Strain rate [s^{-1}]			0.1	1	0.01	0.1	1	0.01	0.1	1
T [°C]	950	X_{RX} [%]		1.5			14	14	22	35
	975		3	15	23	12	44	36	38	55
	1000					27	52	46		
	1025				48			59		
	950	Grain size [µm]					1.5±0.8	1.2±0.5	1.1±0.5	1.6±0.9
	975		1±0.5	1.6±1.0	1.5±1	1.4±0.8	2.6±1.7	1.9±1.1	1.6±0.9	2.2±1.4
	1000					2.2±1.6	4.2±2.9	2.5±1.6		
	1025				3.2±2.4			3.1±2.1		

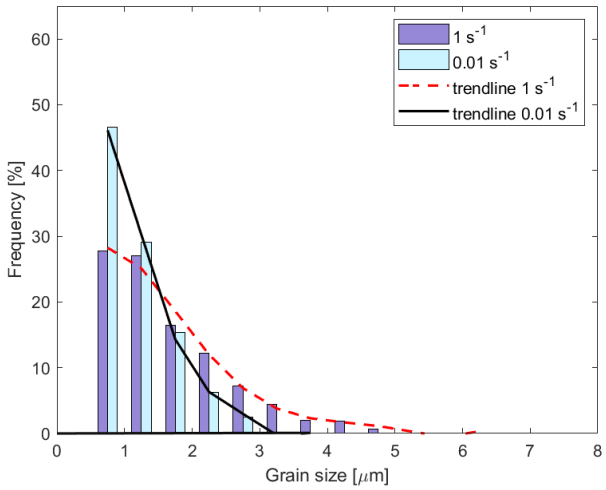

Fig. 4.8 Grain size distribution for recrystallized grains in samples tested at 950°C and a strain of 0.8

Figure 4.8 presents the grain size distribution for the recrystallized areas of specimens compressed at 975°C and a strain of 0.8 with two different strain rates. The purple bars depict the grain sizes at the higher strain rate of $1s^{-1}$ and the light blue bars the slower strain rate of $0.01s^{-1}$. Envelope curves are added for both distributions where red dotted line is for the high and the black continuous curve for the low strain rates. In both microstructures most of the recrystallised grains are smaller than 1 µm followed by a constant decrease in frequency tailing off at around 5 µm. In more detail, at the slower strain rate of $0.01s^{-1}$ the frequency of grains with a size smaller than 1 µm is two-thirds as high as for a strain rate of $1s^{-1}$. The majority of recrystallized grains at slow strain rates is less than 4 µm while the samples compressed faster have a broader scatter in grain area up to 6 µm.

Grain boundary characteristics

Investigating the micrographs in Figure 4.6 in detail, the new grains nucleated at slower strain rates show serrated and uneven boundaries. In contrast, the recrystallized grains in higher strain rate samples have straight boundaries. These specimens also show more twin boundaries than those tested at lower strain rates.

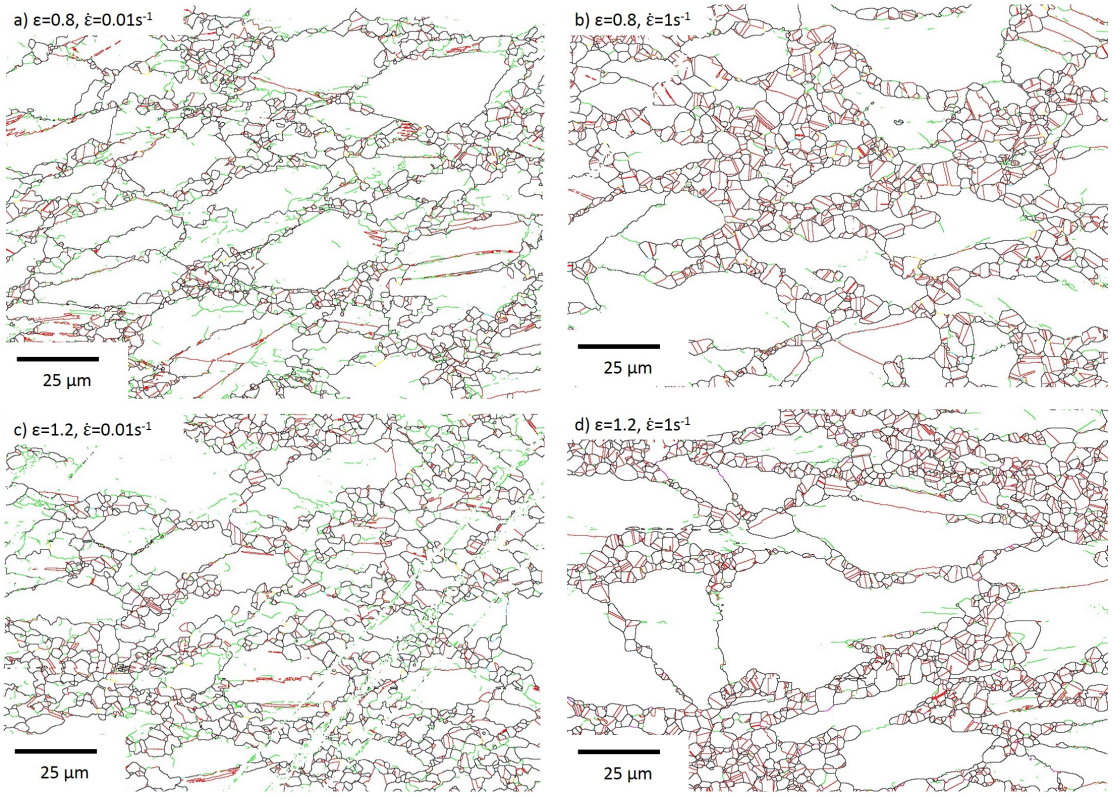

Fig. 4.9 Grain boundary misorientation maps of samples deformed at 975°C at varying strains and strain rates.

Figure 4.9 shows the grain boundary misorientation angles for the microstructures shown previously as IPF maps in Figure 4.6. Low angle (green, (α<15°)), high angle (black, (α>15°)) and twin boundaries (red, 60°⟨111⟩) are given in the images. At lower strain rates the micrographs show more LAGBs in unrecrystallised grains while recrystallised grains seem to consist of less twins. However, this observation can be misleading as the higher strain rate microstructures consist of larger DRX grains. Therefore, the evolution of the grain boundary misorientation angle will be quantified in the following analysis.

The grain boundary misorientation angle α within the recrystallized area was further analyzed. For this purpose boundaries were classified as high angle grain boundaries and twins. The occurrence of each category is presented in Figure 4.10. Higher order twins summed to less than 1% of the total number of twins and were therefore not considered further.

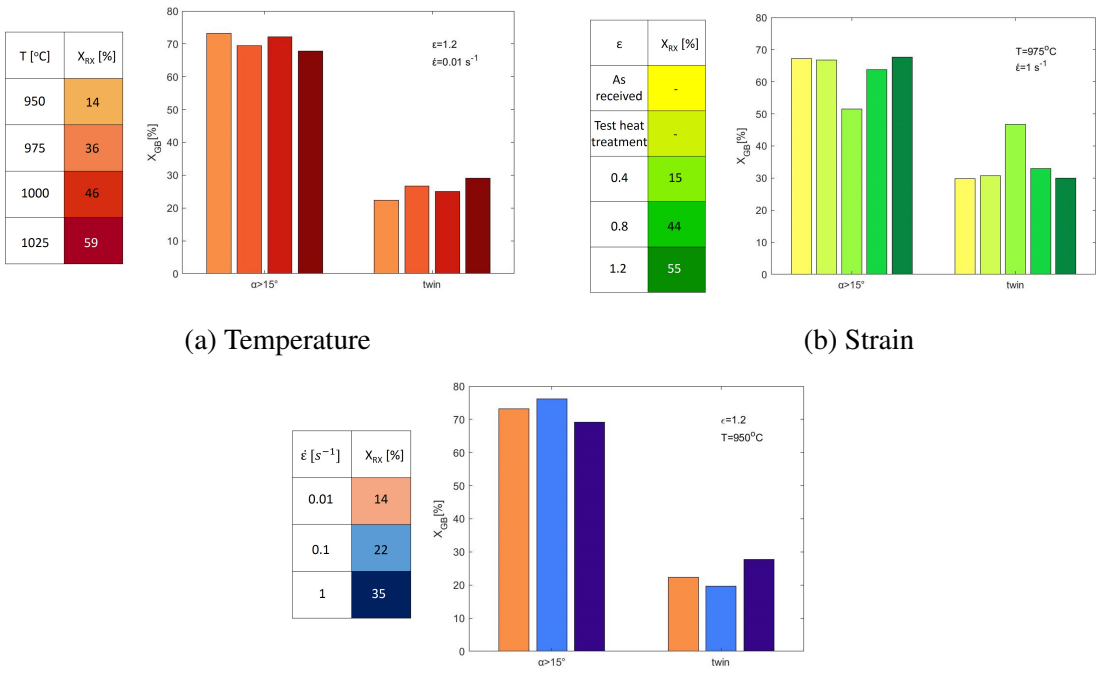

(a) Temperature

(b) Strain

(c) Strain rate

Fig. 4.10 Evolution of the grain boundary misorientation angle with the testing parameters during DRX.

The effect of temperature on the grain boundary misorientation angle is given in Figure 4.10a. Strain and strain rate are kept constant at 1.2 and 0.01s^{-1}respectively. The fraction of HAGBs in the recrystallised area decreases from 73% at 950°C to 69% at 975°C before slightly rising again to 72% at 1000°C and dropping to 68% at 1025°C. This zig-zag behaviour can also be observed for the twin boundaries. Besides the outlier at 1000°C the general trend is a decline in HAGB fraction and growth in twin boundaries numbers.

For the influence of strain on the grain boundary character, two initial microstructures were added in Figure 4.10b to represent un-strained samples. The yellow and light green bars are grain boundary (GB) ratios from the as-received state and after the test-cycle heat treatment. The microstructures of these two specimens were alike and there were no differences in the fraction of grain boundary misorientation angles. Analysing the impact of strain, the microstructure at the lowest strain of 0.4 has the highest fraction of twins and the least HAGBs. From that, the grain boundary fractions gradually align themselves with the as-received state when the strain, hence the recrystallised area, is increased.

The effect of strain rate was studied on specimens compressed to a strain of 1.2 at 950°C (see Figure 4.10c). Even though the recrystallised fraction increases for all three strain rates, the evolution of GB misorientation does not follow this trend. At the highest strain rate of

$1s^{-1}$ the most twin boundaries have formed while at $0.1s^{-1}$ the HAGB content peaked. The microstructure from the lowest strain rate shows an intermediate distribution of twins and HAGBs between the three strain rates.

Dislocation structures of the deformed state

The quantification of the recrystallisation kinetics in 718Plus plays an important part in generating a general overview of the underlying mechanisms. However, a detailed analysis of the dislocation structure formed during deformation can help understanding the effects on a smaller scale. Following EBSD scans, the dislocation structure within the recrystallized area was analyzed using a TEM.

Figure 4.11 illustrates typical microstructures found in the specimens. The specimen shown in Figure 4.11a was taken from a sample deformed at the highest strain rate of $1s^{-1}$. The white arrow marks a high angle grain boundary which divides the area into a recrystallised (left) and deformed (right) part. In the deformed grain itself two further parts can be distinguished: a section with a a high number of subgrains to the left of the red arrow and an area with a high dislocation density to the right. The red arrow marks a low angle grain boundary which shows up in a TEM as a broader and more diffuse line. A HAGB in comparison has a sharp interface without any signs of dislocations inside the boundary. From this image it is clear, that even samples deformed at the highest strain rate of $1s^{-1}$ develop a significant number of subgrains prior and/or in parallel to recrystallisation.

In Figure 4.11b a nucleation event could be captured in a specimen deformed at $0.01s^{-1}$. The area of interest is divided by a HAGB indicated with the white arrows. These point at two recrystallisation nuclei, one in white the other grey. The white nucleus is bordered with an array of dislocations which form a LAGB marked with the red arrow. This feature can be related to the strain induced boundary migration explained in Chapter 2.3.2.4. A bulge is formed at a HAGB due to an inbalance in dislocation content at the boundary. After bulging out, a low angle grain boundary forms to separate the nucleus from the parent grain.

A common assumption is that DRX at low strain rates forms by the subgrain growth while at high strain rates SIBM is the nucleation mechanism. In view of the microstructures shown, SIBM could be detected at a strain rate of $0.01s^{-1}$ and areas of severe subgrain formation at $1s^{-1}$. This indicates , that both mechanisms operate over a wide range of conditions.

Figure 4.12 presents a recrystallised grain within a deformed matrix. The grain shows dislocations which have been formed during the ongoing deformation which takes place in parallel to the grain growth. On the left side of the grain are a few rows of dislocation pile-ups. The dislocation density in this grain is typical for recrystallised grains observed in this study. Hence, it was chosen primarily as an example of dynamically recrystallised grains even though its shape is rather striking.

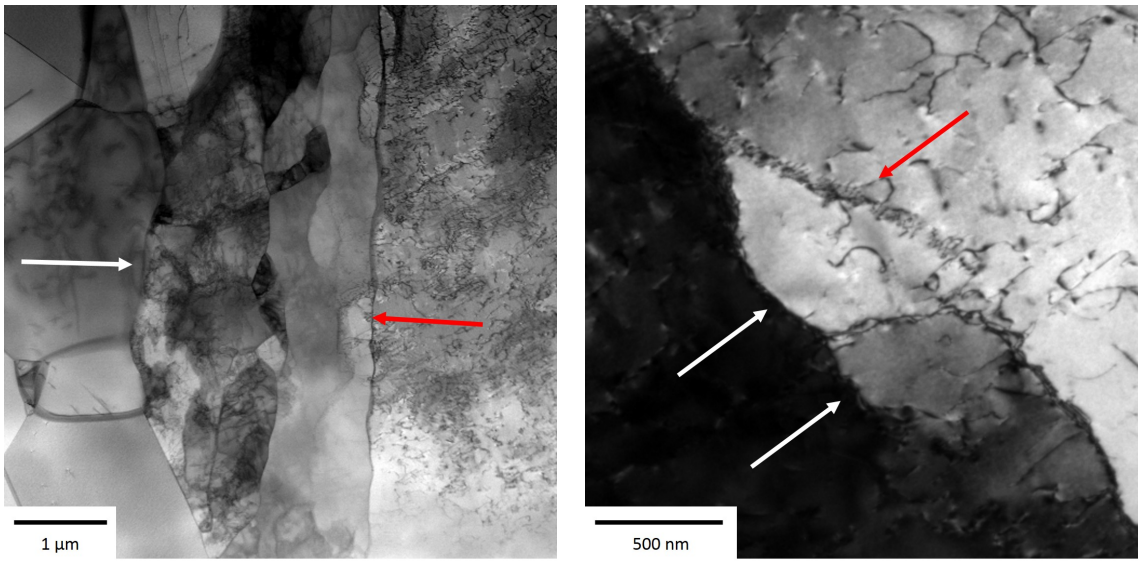

(a) (b)

Fig. 4.11 TEM micrographs of the formation of recrystallised grains deformed to a strain of 1.2. (a) Recrystallised area of a sample compressed at 950°C with $1s^{-1}$; (b) Grain boundary bulge in a specimen at 1025°C and $0.01s^{-1}$

4.2.2 Meta-dynamic recrystallisation

Samples for the characterisation of MDRX were kept in the furnace at the testing temperature after the compression test for 120 s before the water quench. In this section various microstructural characteristics and their changes due to MDRX are analysed.

Recrystallisation fraction and grain size

Figure 4.13 shows the microstructure of specimens with the 120 s dwell. The inverse pole figures and grain boundary misorientation maps are taken from specimens with the exact same testing parameters as those presented in the previous section in Figures 4.6 and 4.9 but with an additional 120 s hold in the furnace. The IPF images consist of a large fraction of recrystallised grains with a low misorientation gradient. Another significant difference to the DRX microstructure is that the recrystallised grains have grown in size.

The measured recrystallised fraction and grain size of the MDRX specimens is given in Table 4.2. The rise in temperature by 25°C from 950 to 975°C leads in all samples to a bigger area covered with recrystallised grains. Straining the samples from 0.8 to 1.2 at 950°C results in a slight decrease in the amount of recrystallised fraction. At 975°C and $0.01s^{-1}$ X_{RX} increases from 81 to 90% when compressing to the higher strain. The influence of strain at $1s^{-1}$ results however, in a diminution of recrystallisation from 99% at 0.8 to 95% at 1.2. Considering the changes with strain rate, the recrystallised fraction increases with faster strain

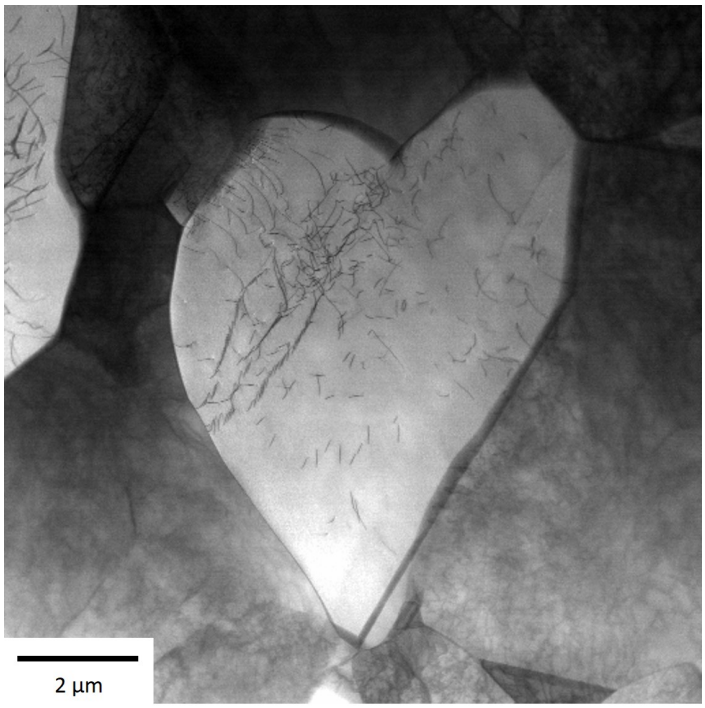

Fig. 4.12 Recrystallised grain in the specimen compressed at 1025°C at 0.01s^{-1} to 1.2.

rate for all of the three pairs. Given the fact that the kinetics of recrystallisation slows down with reaching a fully recrystallised microstructure and the high degree of recrystallisation achieved in these samples, effects of the forging parameters should only be deduced with great care. In addition, the difference between the recrystallised fractions is only minor and cannot be assumed to be significant.

The grain size of the recrystallised area is presented in the lower part of Table 4.2. Grains of all samples continued growing during the 120 s dwell. The influence of temperature on the grain size evolution is similar to the recrystallised fraction as grains are invariably larger at higher temperatures. Altering the strain from 0.8 to 1.2 resulted in various trends. For testing conditions at 950°C and 1s^{-1} the grain size stayed almost constant, at 975°C and 0.01s^{-1} the grains shrank and at 975°C and at 1s^{-1}, the grains grew from 5 to 5.6 µm. The rise in strain rate on grain size led to a growth for specimens tested at 975°C a strain of 1.2 and reduction in size at 0.8. However, the standard deviation of the grain size was large indicating a broad grain size distribution.

From the detailed analysis of the effect of forging parameters on recrystallised fraction and grain size no consistent trend can be distinguished for strain and strain rate. However, rising the temperature by 25°C produced an almost fully recrystallised microstructure and the largest grain sizes.

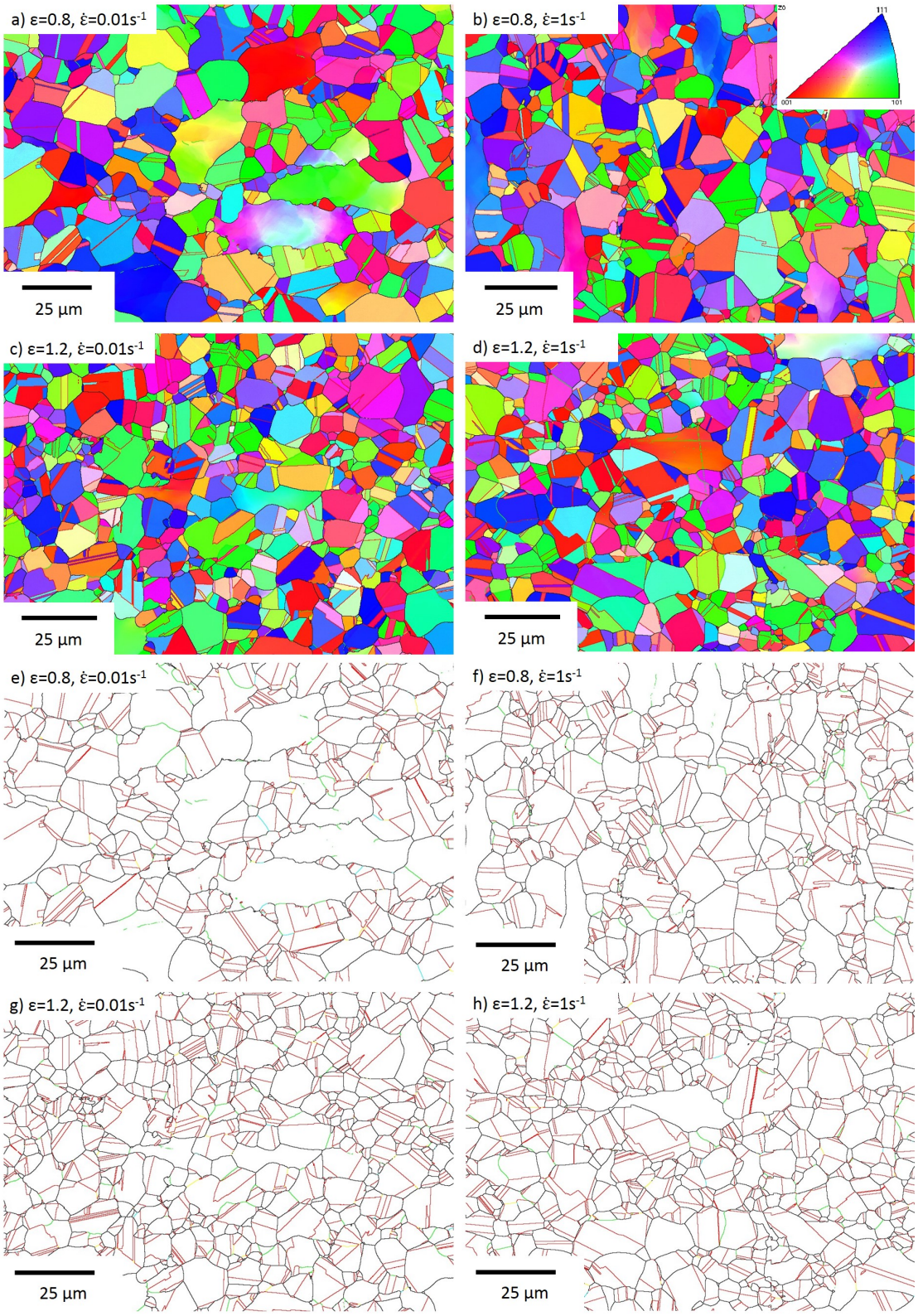

Fig. 4.13 IPF and grain boundary misorientation maps of MDRX samples deformed at 975°C at varying strains and strain rates kept in the furnace for 120 s.

Table 4.2 Recrystallised fraction and average recrystallised grain size with standard deviation for MDRX.

Strain [-]			0.8		1.2	
Strain rate [s^{-1}]			0.01	1	0.01	1
T [°C]	950	X_{RX} [%]		80	20	78
	975		81	99	90	95
	950	Grain		3.2±2.2	1.2±0.6	3.1±2.2
	975	size [µm]	5.9±4.6	5±3.5	4.7±4.1	5.6±4

Grain boundary characteristics

Figure 4.13 e to h presents the grain boundary orientation map with LAGBs in green, HAGBs in black and twins in red. A detailed breakdown of the actual numbers of GBs in the samples is presented in Figure 4.14. The graphs were deliberately designed to show changes from DRX to MDRX.

Starting with the effect of temperature on MDRX in Figure 4.14a. The darker bars (orange and red) represent DRX specimens and the lighter bars the equivalent samples after the 120 s dwell time. At both temperatures, MDRX generates less HAGB and more twins than DRX. Increasing the temperature results in less HAGB for both recrystallisation mechanisms.

Figure 4.14b presents the grain boundary misorientation fractions at varying strains for DRX and MDRX. At a constant strain the HAGB bars for MDRX (lighter coloured) are taller meaning more HAGBs in these microstructures. A rise in strain from 0.8 to 1.2 produces a higher fraction in HAGBs while the trend is reversed for twin boundaries. In general, this pattern is the opposite to what is found for the dependence of temperature.

Keeping the strain rate fixed in Figure 4.14c yields a decrease and an increase of HAGBs with dwell time. Whilst during DRX more twins grow with accelerating strain rate the opposite is found for the effect of strain rate on MDRX

Unfortunately, the as-described effects of the forging parameters on MDRX are inconclusive. The effects are small and inconsistent. A more detailed analysis is required to draw valid conclusions.

4.2.3 Discussion

In the previous section, the results of DRX and MDRX in an η-free microstructure were presented. In particular, the recrystallised parts were analysed for changes in recrystallised fraction, grain size and grain boundary character. The 120 s dwell in the MDRX specimens developed a higher degree of recrystallised fraction as expected. However, the detailed

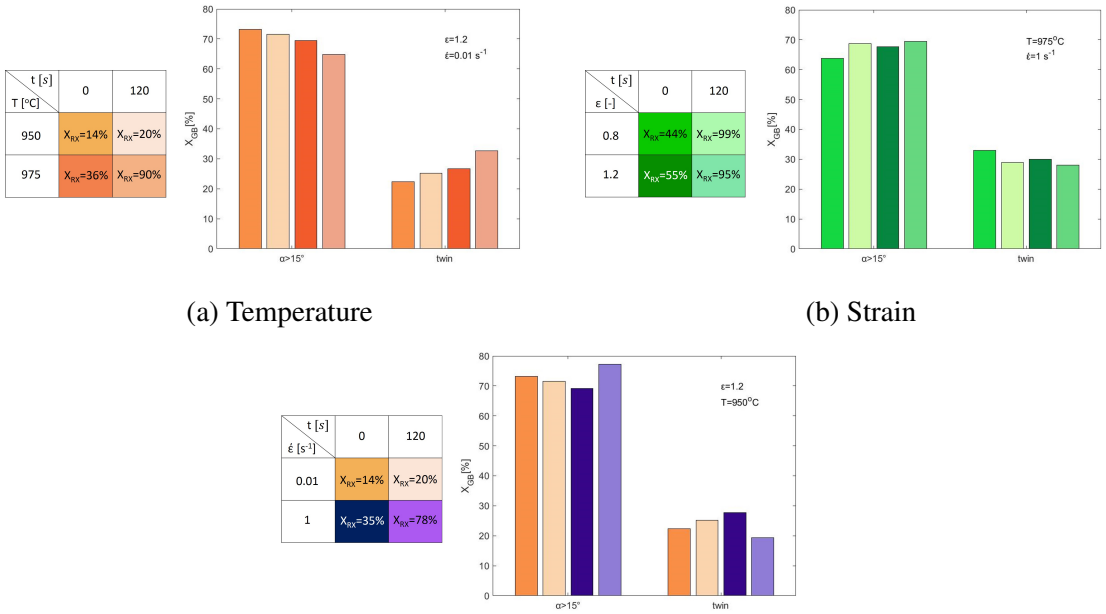

(a) Temperature

(b) Strain

(c) Strain rate

Fig. 4.14 Evolution of the grain boundary misorientation angle with the testing parameters for DRX and MDRX specimens.

analysis on the kinetics of MDRX was inconclusive. Thus, the discussion focuses on the influence of the forging parameters on DRX.

Effect of temperature and strain

The increase of temperature in 718Plus resulted in a larger recrystallized area. As the grain boundaries become more mobile with temperature, the grains can grow further after nucleation. Alongside the faster movement, stacking errors at the migrating grain boundary are more likely to occur which can result in the formation of twin boundaries [80]. This hypotheses suggests, that the higher the grain boundary mobility, the more twins are generated. Such a pattern was seen in the evolution of grain boundary misorientation angle in Figure 4.10a.

Deforming the sample to higher strains results in a greater density of dislocations in the material. The dislocations provide a source of stored energy for nucleation and growth. A higher dislocation density could be the source of errors and hence twinning. However, this could not be confirmed with the current analysis and requires further study.

Effect of strain rate

The literature describing similar forging simulations on 718Plus demonstrate a counter-intuitive rise in recrystallized area fraction with increasing strain rate [63, 64]. It is generally

argued, as in case of IN718 [134, 135], that the longer time involved in slower strain rate tests allows much more recrystallization to occur leading to a higher recrystallized volume fraction. The forging time for the various strain rates used in the current experiments deformed to the upper strain of 1.2, vary from 0.7 s for the $1s^{-1}$ strain rate to 70 s for the slowest strain rate of $0.01s^{-1}$. The experiments included a 5 s transfer time between the compression and the water quench. MDRX starts immediately after deformation is finished without any incubation period [37]. Figure 4.15 shows the evolution of DRX and MDRX in IN718 at 980°C. To investigate the DRX regime the samples were immediately quenched after deformation at varying strains up to 0.82. The recrystallized area increases with lower strain rate. However, the dwell time after deformation has a significant influence on recrystallization. After 3 s, the specimens compressed with a strain rate of $1.1s^{-1}$ show the second highest recrystallized fraction. The post-processing routines for EBSD scans used in the present work could not pick up the difference between DRX and MDRX. However, recent progress in this field allows to discrimination between these two mechanisms using a denoising filter [136]

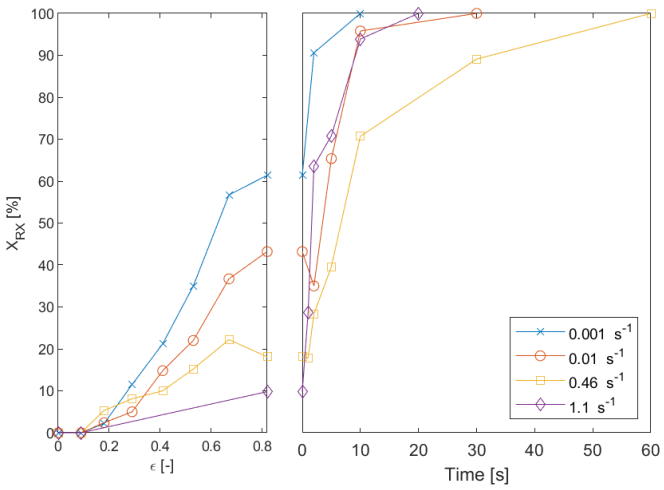

Fig. 4.15 Volume recrystallized of IN718 in dynamic and meta-dynamic regime at 980°C [12]

When the delay of 5 s in removing the sample from the furnace is added, it makes the meta-dynamic component of the high strain rate tests very significant in comparison to the deformation time but contributes relatively little at lower strain rates. In the TEM images in Figure 4.16a we see the effect of the meta-dynamic component in the recrystallized grains of the slow deformed sample. These contain a significant density of dislocations, albeit rather lower than the unrecrystallized grains, which show a well-developed sub-grain structure (marked SG in Figure 4.16a). In the case of the grains illustrated in Figure 4.16a, it can be observed that part of the grain is dislocation free with a distinct boundary between the

two areas. Such an observation suggests that the clear part of the grain recrystallized after the forging has ceased. In the case of the 0.01 s^{-1} strain rate the 5 seconds meta-dynamic component was 7% of the total exposure (dynamic+meta-dynamic) but nevertheless makes a significant contribution in some grains which grow the same distance during MDRX as they do in DRX. In the faster strain rate sample $1s^{-1}$, the deformed grains, constituting 45% of the sample, show a very high and relatively homogeneous dislocation density (Figure 4.16b). In contrast, most of the recrystallized grains are generally clear of dislocations, indicating that they formed during the meta-dynamic period of the deformation. However, some show significant densities of dislocations indicating that they formed during the 0.7 s of forging time. It is tempting to assume that the relative size of the meta-dynamic component of the recrystallization time in the high strain rate samples is the reason for the rise in recrystallized volume fraction with strain rate. Evenso, two other papers describe the same effect [63, 64]. The compression tests performed by Mitsche et al. [64] contain a transfer time of less than 0.5 s but the DRX volume fraction also increases with strain rate. Similar experiments with IN718 have been performed with delays in quenching of up to 3 s showing the expected behaviour of less DRX at lower strain rate [134].

What is clear is that the rate of recrystallization is dramatically increased by increasing the strain rate - what happens in 70 s at low strain rate happens in 0.7 s at higher strain rates. Not only is the nucleation very rapid, but the growth is phenomenally fast. Ignoring nucleation time and allowing growth throughout dynamic and meta-dynamic processing, growth rates are greater than 0.39 µm s^{-1} at 1 s^{-1} and 0.025 µm s^{-1} at 0.01 s^{-1} some 16 times faster at the high strain rate. It is hard to justify this difference on a simple driving force argument as the dislocation density, although lower through recovery at the low strain rate, is not 16 times lower. What is also interesting is that there are many more smaller grains in the lower strain rate, Figure 4.8 - the grain coverage is similar with roughly the same number of boundaries showing no or very few nuclei. This suggests that nucleation at the slow strain rates happens readily, but that the grains do not grow. A possibility is that the recovery gives locally high dislocation levels able to initiate the grain bulging but that as the grains grow they encounter the lower density of subgrain interior and cease to grow.

The observed substructures are commonly used to distinguish between continuous (cDRX) and discontinuous DRX (dDRX) [42, 63]. While cDRX is described as a progressive strain-induced subgrain rotation, dDRX is referred as the bulging mechanism of pre-existing high angle grain boundaries. These two mechanisms are meant to progress on different time-scales, explaining the strain rate dependency of the recrystallized fraction. Even though cDRX is thought to be the rotation of subgrains, computer simulations as well as experiments were only able to confirm this for a few well defined grain bound-

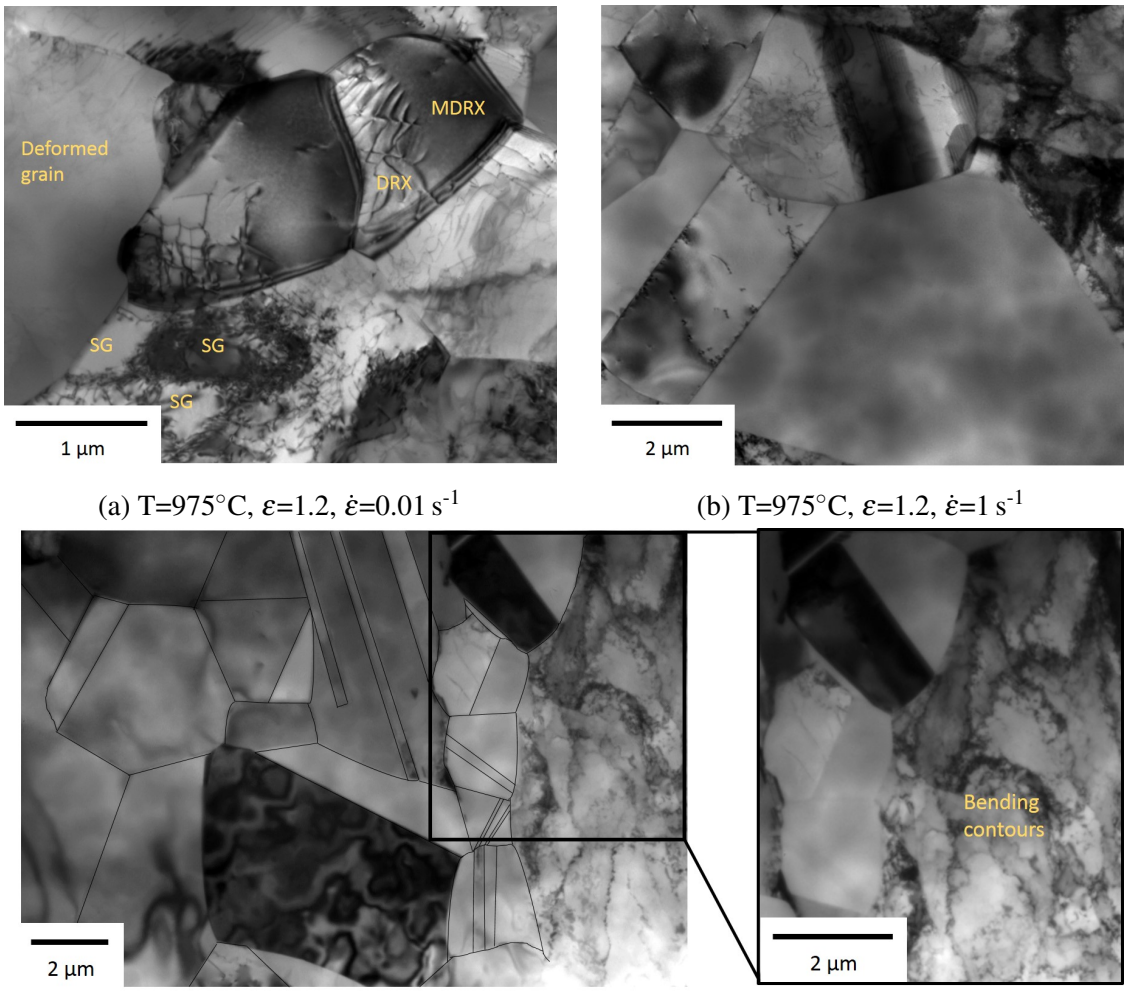

(a) T=975°C, ε=1.2, $\dot{\varepsilon}$=0.01 s^{-1}

(b) T=975°C, ε=1.2, $\dot{\varepsilon}$=1 s^{-1}

(c) T=950°C, ε=1.2, $\dot{\varepsilon}$=1 s^{-1}, 120 s dwell

Fig. 4.16 TEM analysis of microstructures with different strain rates and post-deformation dwell times

aries [74, 73]. It is more helpful to think of cDRX as a progressive subgrain growth where a subgrain consumes the adjacent substructures leading to a continuous increase in grain boundary misorientation angle. However, the formation of the bulges in dDRX also requires the arrangement of subgrain boundaries [39] which weakens the assumption that subgrain development causes the time delay.

The consistent trend in 718Plus to increase the recrystallized fraction with increasing strain rate is opposite to the trend observed in IN718. Yet the flow curves of the two alloys deformed in the same series of experiments reported by Momeni et al. [63] are remarkably similar, in particular the rate of softening is much the same. Momeni et al. interpret this as change from dDRX at high strain rates characterized by high flow stress and rapid softening

from recrystallization to a flatter curve with little softening characterized by a recovery at a rate able to keep up with the strain rate. They highlight the potential change in stacking fault energy (SFE) produced by the increase in cobalt in 718Plus but there is little evidence of the change in behavior from the flow curves. It could be possible that 718Plus has a recovery rate fast enough to prevent the rapid recrystallization but not sharp enough to give such well-defined subgrains that produce a recrystallized structure.

The strain rate also seems to have a distinct influence on the evolution of twin boundaries. Samples at slow strain rates develop fewer twins than at faster strain rates. This is a sign that a higher degree of recovery takes place at low strain rates [137]. The decrease in twin boundaries can be explained by the growth accident model published by Gleiter et al. [80]. This theory assumes that twins form at migrating boundaries due to a stacking error. The higher the grain boundary mobility, the more twins are generated. If the microstructure recovers before the onset of recrystallization the grain boundary migration rate is lower and therefore fewer twins are formed.

4.3 Recrystallisation of the η microstructure

Secondary phases can act as additional nucleation sites for recrystallisation. Particle stimulated nucleation (PSN) and heteroepitaxial recrystallisation (heRX) in nickel-base superalloys are two mechanism which require the presence of precipitates [34, 100]. Hence, the influence of η phase on the kinetics of dynamic and meta-dynamic recrystallisation will be analysed.

4.3.1 Dynamic recrystallisation

Microstructure and η content

Figures 4.17 a and b show the IPF maps in the out-of-plane direction from EBSD scans for the samples compressed at 975°C to 0.8 with a strain rate of 0.01 and 1 s^{-1}. The higher strained samples are in e and f. Below the IPF maps are the corresponding back-scattered electron (BSE) images of the area with the secondary precipitates highlighted in read. The η precipitates were too thin to be successfully identified by EBSD thus the Z (atomic number)-contrast from BSE images were used to distinguish η.

The recrystallised grain structure alters between the low strain rate on the left and the high strain rate on the right. Similarly to the η-free microstructure, the boundaries at $0.01s^{-1}$ are more serrated than at $1s^{-1}$. Hence these observations are inherent to recrystallisation and are independent of the phases present in the microstructure.

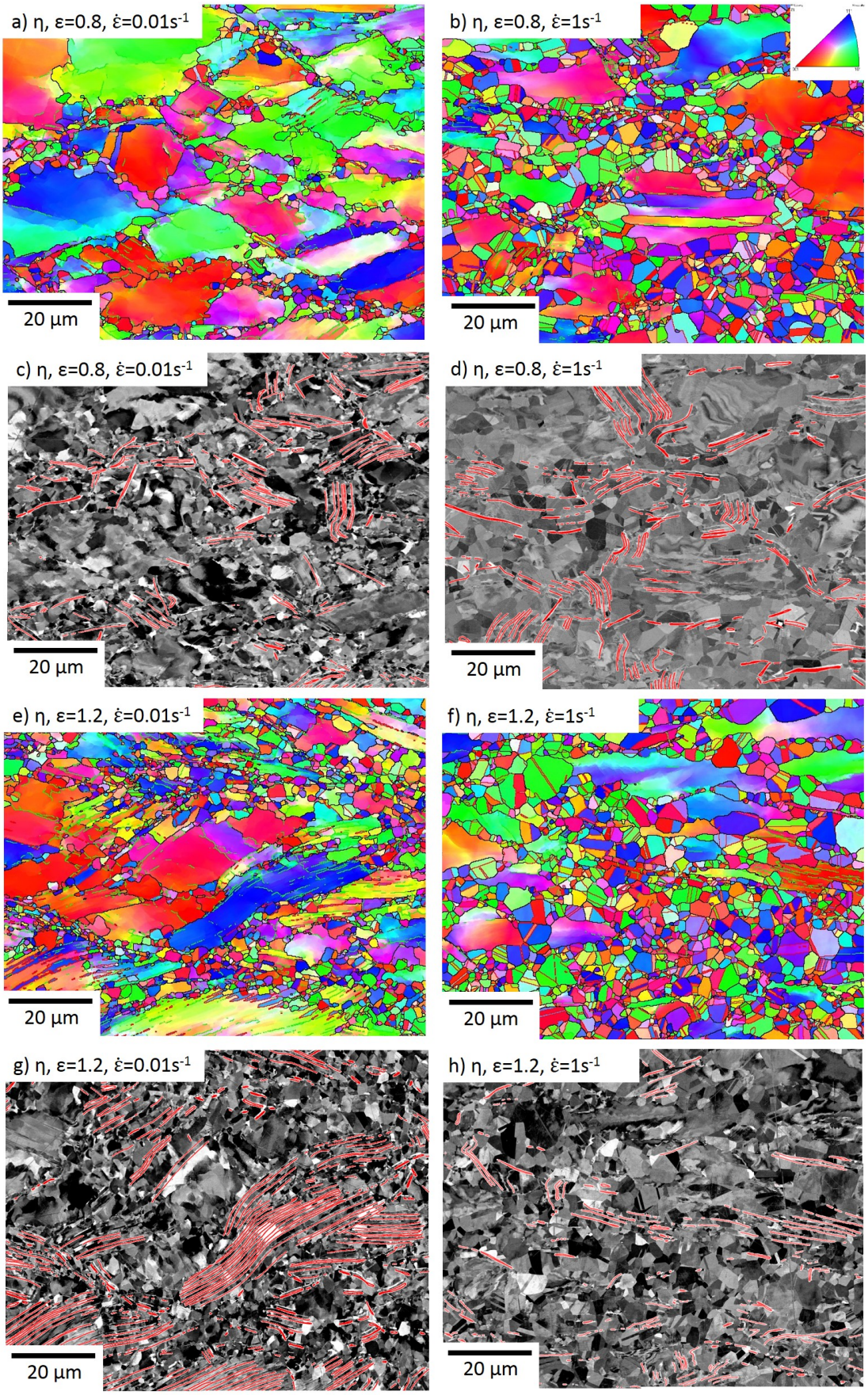

Fig. 4.17 IPF maps and corresponding BSE images of η samples deformed at 975°C at varying strains and strain rates

The η content was measured as described in Chapter 3.3.1. In Figure 4.17c η takes up 4.0 area%. Slightly more η is found in image d at the higher strain rate with 4.4 area%. The micrographs from the tests at higher strain in Figure 4.17g and h seem to be distinctively different in their η precipitation . At the low strain rate in g η occupies 7.0 area% while in h it dropped down to 2.3 area%. The reason for the low ηcontent in g could be a partial dissolution due to adiabatic heating of the sample. The test temperature was 975°C, close to the η solvus temperature, and the high strain rate has already been shown to cause heating in the sample. All other samples appear to be at around the precipitate content of 5 area% measured after the heat treatment (Chapter 4.1.1). A detailed breakdown of the measured η area fractions in the DRX samples is given in Table 4.3.

Recrystallised fraction

The recrystallised fraction was calculated in the same fashion as for the η-free microstructure and the results are presented in Table 4.3. The average grain size are given in the middle section of the table.

The recrystallised fraction increases with temperature in all specimens. Raising the temperature from 950 to 975°C leads to 30% more recrystallisation at a strain of 1.2 and strain rate of $1s^{-1}$. A rise of 60% is achieved at a strain rate of 0.01 and for samples strained to 0.8 with $1s^{-1}$ the recrystallised area almost doubled.

By compressing to higher strains the recrystallised fraction at 950°C gradually climbs from 7% at 0.4 to 37% at 0.8 and peaking to 58% at a strain of 1.2. Likewise, testing at 975°C and 0.01 and $1s^{-1}$ results in a consistent growth of recrystallised area.

Raising the strain rate enlarges the recrystallised area as well. However, this trend is reversed by the specimen compressed with the intermediate strain rate of 0.1 s^{-1} at 950°C to 1.2. Under these conditions the amount of recrystallisation drops marginally from 26%

Table 4.3 Recrystallised fraction and average grain size with standard deviation of recrystallised area in the η-containing samples. η content is the area covered by precipiates from the whole microstructure.

Strain [-]			0.4	0.8		1.2		
Strain rate [s^{-1}]			1	0.01	1	0.01	0.1	1
T [°C]	950	X_{RX}[%]	8		37	26	25	58
	975			20	70	42		76
	950	Grain	1.3±0.7		1.4±0.9	1±0.5	0.9±0.4	2±1.2
	975	size [µm]		1.2±0.7	1.9±1.3	1.2±0.6		2.3±1.8
	950	η content	5.2		4.5	6.5	4.6	5.7
	975	[%]		4.0	4.4	7.0		2.3

at 0.01s^{-1} to 25%. An acceleration in strain rate to 1s^{-1} induces 58% of the total area to recrystallise.

The positive effect of temperature and strain in the η-containing microstructure is in line with the observations from the η-free tests. In the same way, DRX clearly increases from a strain rate of 0.01 to 1s^{-1} with an intermediate plateau at 0.1s^{-1}.

In absolute numbers the η specimens have a slightly larger area recrystallized than η-free. It should be remembered at this point that the initial grain sizes of the two microstructures was different. Figure 4.18 shows a comparison of the recrystallized fractions with strain rate of the two microstructures. Here it becomes obvious that the recrystallization kinetics at the lower strain rates deviates significantly from the high strain rate.

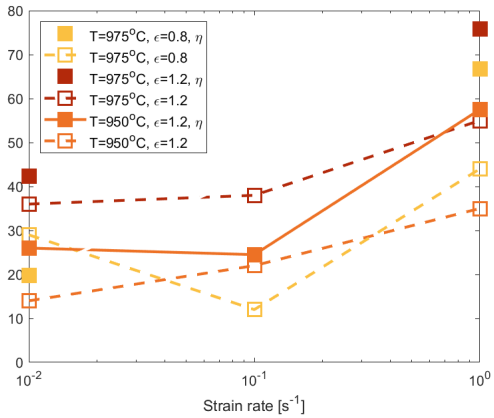

Fig. 4.18 Recrystallized fraction with strain rate for η and η-free tests

Grain size

The evolution of the average recrystallized grain size follows the observed patterns for DRX. The grain size enlarges with the testing parameters while the sample at intermediate strain rate shows the same behavior as for the recrystallized fraction. All of these results are in-line with the previously reported trends in the single-phase microstructure.

The heterogeneous distribution of the η precipitates could suggest a broad distribution in recrystallized grain size. Figure 4.19a presents the spread of grain size for the η specimens tested at 950°C, 0.01 and 1$s^{-1}$and 0.8. The corresponding η-free samples are given in b. The darker bars (green for η, purple for η-free) are the values for the tests at high strain rate and the lighter colours represent the ratios for a strain rate of 0.01s^{-1}. Envelope curves are plotted in both graphs for the respective strain rate.

A majority of the grains in both microstructures is smaller than 1 µm. Another commonality is that the peak of the curves is larger for the slower strain rate and tails off more rapidly at smaller grain sizes. However, the gradient is steeper for the η-containing microstructure

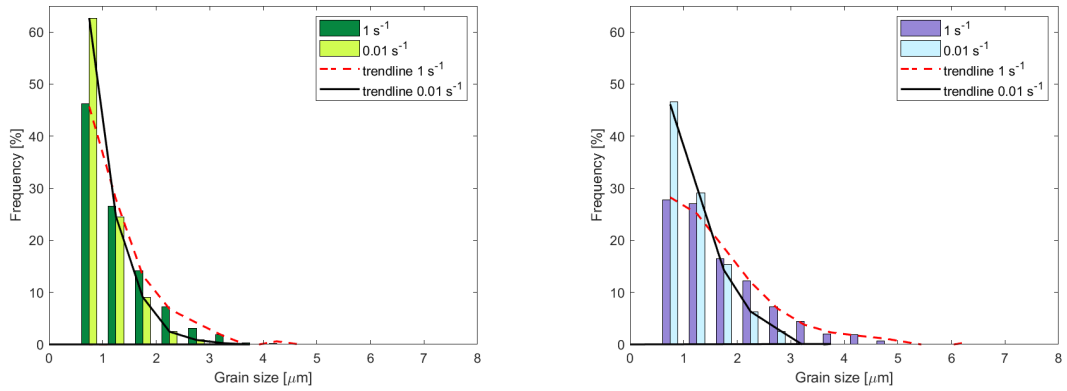

Fig. 4.19 Grain size distribution of samples deformed at 950°C to a strain of 0.8 and strain rates of 0.01 and 1 $s^{-1}$with the microstructures of a) η and b) η-free

and the difference between the strain rates is less pronounced. The η-containing samples developed a smaller grain size spread at both strain rates than the single-phase specimens.

Grain boundary characteristics

The evolution of the grain boundary misorientation angles for η specimens tested at 950°C is illustrated in Figure 4.20. The misorientation angle α was distinguished into high angle boundaries (HAGB, α>15°) and twins (α=60°$\pm$8.66° $\langle 111 \rangle$ [129]). The fractions of the grain boundaries were measured by counting one point per boundary.

The effect of temperature on the grain boundary misorientation angle is illustrated in Figure 4.20a. Even though the recrystallised fraction increases with temperature, the GB character remains constant. Comparing this results with the grain sizes given in Table 4.3 they increase only marginally from 1 to 1.1 µm at 975°C. Hence, the increase in recrystallisation at this specific sample set was based on a higher nucleation rate rather than grain growth.

HAGB and twin ratios for the tested strains are plotted in Figure 4.20b. Yellow and light green depict the GB character of the as-received state and after the η heat treatment respectively. At the lowest strain of 0.4 the microstructure consists of the highest fraction in twins of all 5 conditions. From that, the ratio decreases eventually levelling with the initial microstructure after the η heat treatment.

In Figure 4.20c the influence of strain rate on the GBs is given. Even though the recrystallised fraction and the grain size record a decrease in their numbers from 0.01 to 0.1s^{-1} followed by a climb at 1s^{-1}, this pattern is absent for the GB characteristics. HAGB consistently go down with strain rate by the expense of twin boundaries.

By and large, the grain boundary misorientation angles of the η-containing microstructure show an analogous behaviour to the η-free specimens. However, the effect of temperature in the η samples presented is only faintly visible and the results from the intermediate strain rate of $0.1s^{-1}$ were unexpected.

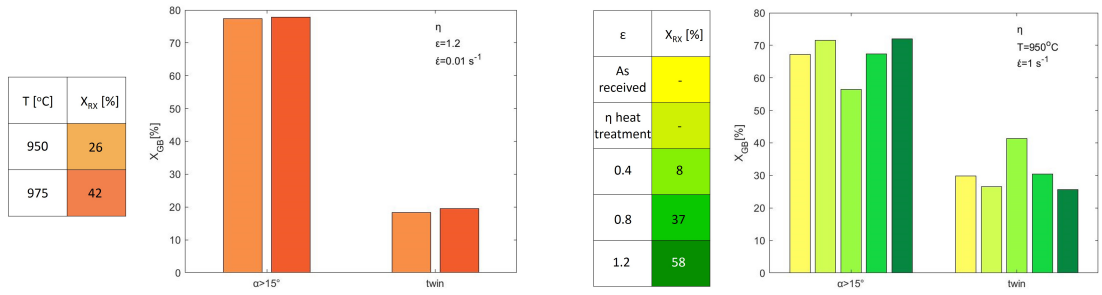

(a) Temperature

(b) Strain

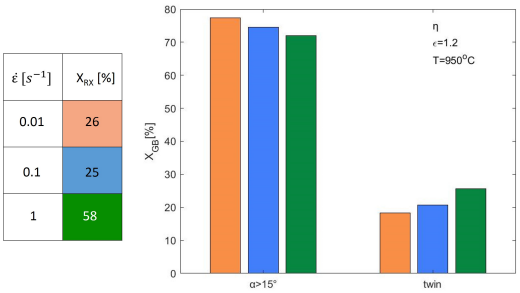

(c) Strain rate

Fig. 4.20 Evolution of grain boundary misorientation for η samples.

4.3.2 Meta-dynamic recrystallisation

Likewise for the η-free specimens reported in Section 4.2.2, kinetics for MDRX in the η-containing microstructure is analysed after the deformed cylinders were kept in the furnace for another 120 s. The study followed the same principal as previously by presenting the recrystallised fraction, grain size and distribution and the grain boundary misorientation angle.

Recrystallised fraction and grain size

The meta-dynamically recrystallised samples tested at 975°C are shown as IPF maps in the out-of-plane-direction and BSE images in Figure 4.21. These are the corresponding MDRX specimens to those shown for DRX in the previous section in Figure 4.17. The top

Table 4.4 Recrystallised fraction and average grain size with standard deviation of recrystallised area in the η-containing samples. η content is the area covered by precipiates from the whole microstructure.

Strain [-]			0.8		1.2	
Strain rate [s^{-1}]			0.01	1	0.01	1
T [°C]	950	X_{RX}[%]		66	49	78
	975		53		77	98
	950	Grain		1.8±1.3	1.1±0.7	1.5±1.0
	975	size [µm]	1.7±1.6		2.2±1.5	2.2±1.8
	950	η content		5.0	5.6	4.1
	975	[%]	6.1		4.0	3.3

pair is from the test to a strain of 0.8 and at the bottom to 1.2. On the left side the slow strain rate is represented and to the right the high strain rate.

The microstructure consists of recrystallised grains alongside few deformed grains with a higher orientation gradient. The recrystallised grains appear, in general, larger than after dynamic recrystallisation. This observation is according to the findings of recrystallisation in the η-free specimens. Besides unrecrystallised areas, the recrystallised grain distribution seems to consist of a number of small grains alongside larger ones. A majority of grains with a diameter smaller than ~2 µm are in the vicinity of η particles.

The average grain sizes together with the recrystallised area and η content are given in Table 4.4. All three parameters, temperature, strain and strain rate have a positive influence on the recrystallised fraction. The same holds true for the effect of temperature and strain rate on the grain size. At 975°C and 1.2 the average grain size stayed constant however, the standard deviation increased from 1.5 to 1.8 µm. It can be assumed, that at $1s^{-1}$ even though some grains were larger compared to $0.01s^{-1}$ more smaller grains could inhibit a shift of the average grain size towards higher values. Compressing to higher strains resulted in a decrease of grain diameter from 1.8 to 1.5 µm at lower temperatures and a growth at 975°C by 0.5 µm. The standard deviation of the grain size increased from the DRX to the MDRX microstructure which was also found in the η-free specimens. A better way of understanding grain size variabilities is a visualisation of the grain size distribution.

To analyse the grain size heterogeneity in more detail the size distribution is given in Figure 4.22. The diagrams present the evolution of grain sizes with post-deformation dwell time for specimens deformed at 975°C to a strain of 1.2 with $1s^{-1}$. The η-containing microstructures in green only show small changes in the grain size spread during MDRX. Both microstructures have a descending frequency of grain size with the tallest peak at the smallest grains. The MDRX microstructure developed a few grains larger than 7 µm. The

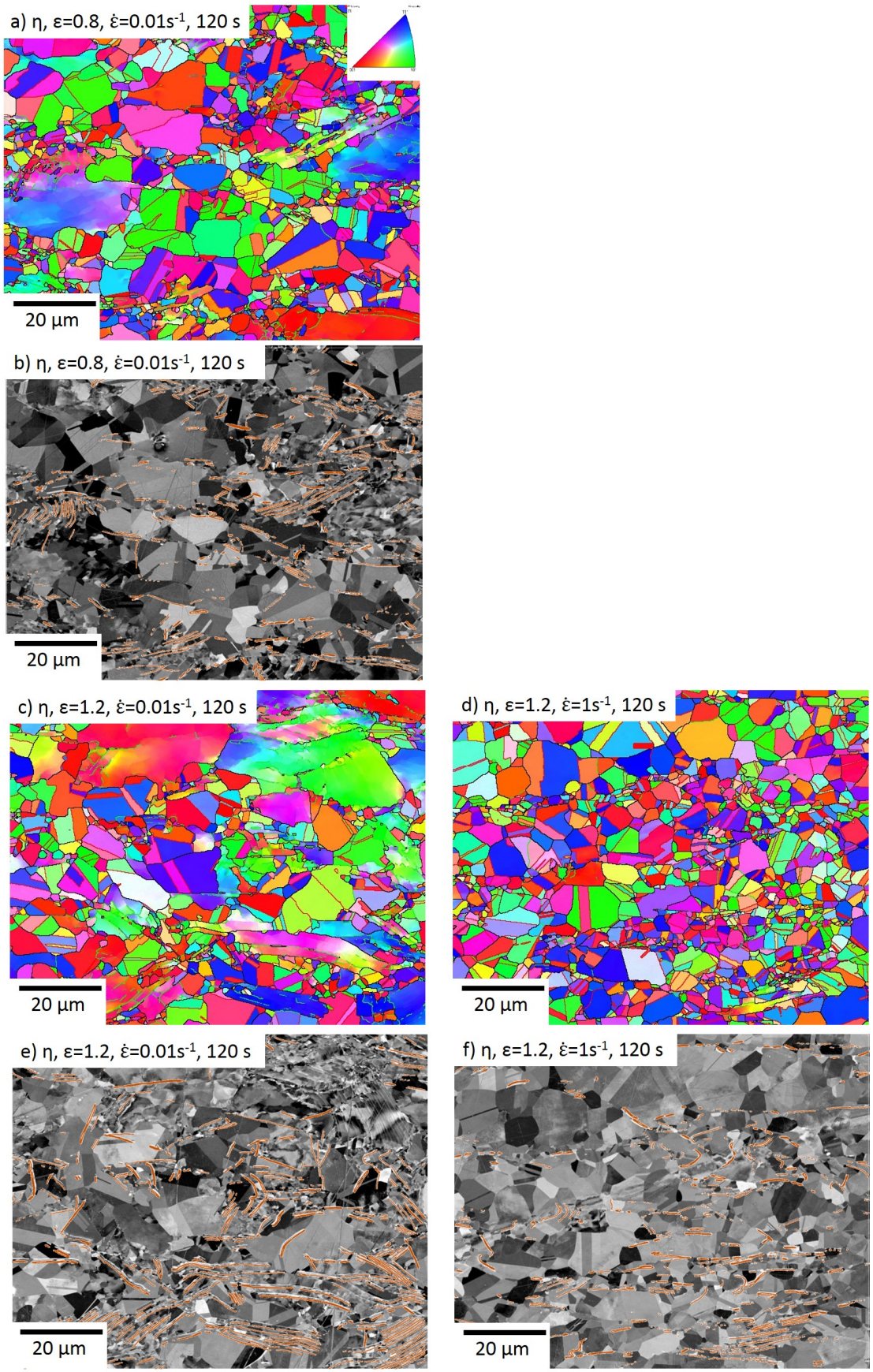

Fig. 4.21 IPF maps and corresponding BSE images of η samples deformed at 975°C at varying strains and strain rates in the MDRX regime after 120s^{-1} dwell

η-free samples are given in blue and purple and the differences in grain size variance are significant. The specimens without dwell have a similar distribution to the η-containing microstructure with a plateau at the smallest grain sizes. However, the grain size distribution after 120 s is distinct from η-containing specimens. Even though most grains are still smaller than 0.8 µm, the proportion between η and η-free has diminished by two-thirds. Several other peaks can be detected with a clear shift to higher grain sizes. The scatter is broader and lasts up to the cut-off size of 15 µm. About 3% of grains were larger and are not represented in this graph.

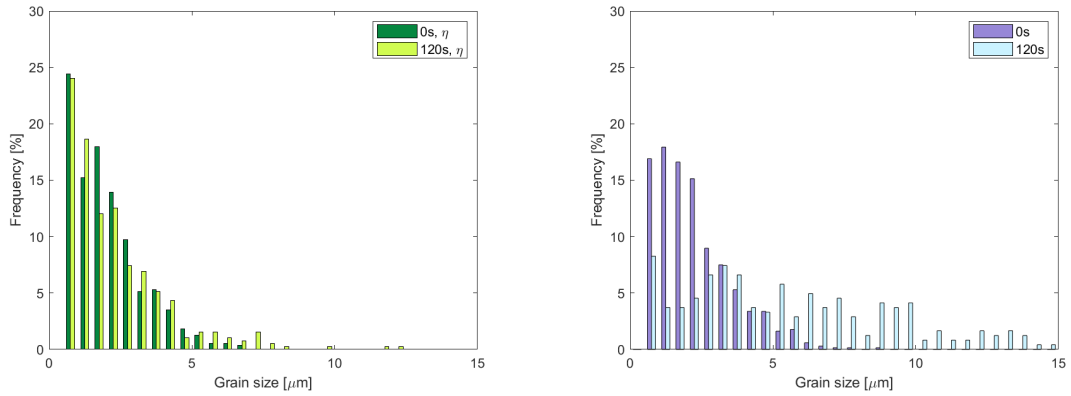

(a) (b)

Fig. 4.22 Grain size distribution for 0 and 120 s dwell time and samples deformed at 975°C, ε=1.2 and $\dot{\varepsilon}$=1s^{-1}. (a) η-containing (b) η-free microstructure

Grain boundary characteristics

The evolution of grain boundary misorientation angle is presented in Figure 4.23. Each graph shows two pairs of samples with the darker coloured ones being DRXed and lighter coloured from MDRXed microstructures.

In the first graph in Figure 4.23a the HAGB and twin fractions are given with varying temperatures. In general, MDRX caused a smaller relative number of HAGBs by forming more twins. Raising the temperature from 950 to 975°C had the same effect.

For the influence of strain the picture is less straight forward. At a strain of 0.8 the microstructure forms relatively more HAGB during the 120 s dwell and at 1.2 the reverse is true. These contradicting results depict what was found in the grain size evolution where the grains appeared to have shrunk at the higher strain.

Comparing the effect of strain rate, the fraction of HAGBs in the MDRX microstructures is reduced with faster strain rate. In the η-free samples the number of HAGBs increased during the dwell time after compression at 1s^{-1}. Interestingly, the trend for the grain boundary

characteristics from DRX to MDRX are the same for both pairs even though the evolution of grain sizes is not.

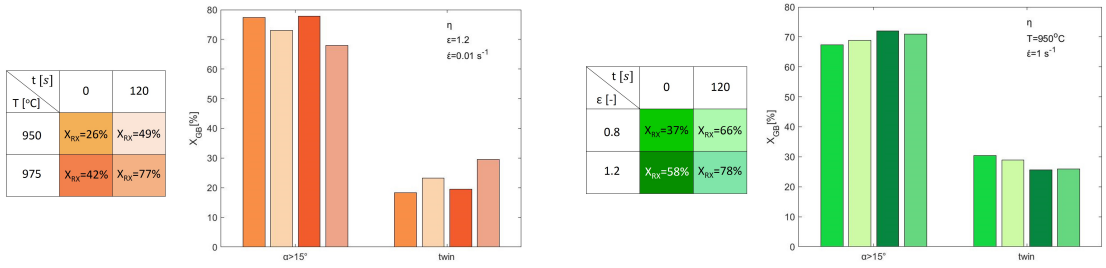

(a) Temperature

(b) Strain

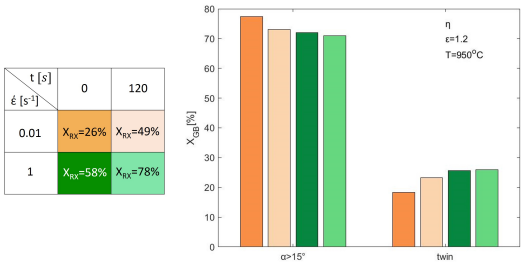

(c) Strain rate

Fig. 4.23 Evolution of grain boundary misorientation for MDRX in η samples with (a) temperature (b) strain (c) strain rate

4.3.3 Discussion

The secondary η precipitates in 718Plus were found to influence recrystallisation of the alloy during high temperature compression. The recrystallized fraction during DRX and MDRX were higher in the two-phase microstructure. In addition, MDRX in η-free leads to a multi-modal grain size distribution.

Dynamic recrystallization seemed to increase with the presence of η. However, this cannot be solely attributed to the particles as the initial grain size of the two-phase microstructure is slightly smaller. Grain boundaries are the preferred nucleation site for recrystallizing grains hence DRX will be faster in finer microstructures [34].

In terms of post-deformation recrystallization, the grain size distribution and the recrystallised fraction were affected the most by the secondary particles. The grain size distribution of the η samples had a single peak at the smallest grain size and tailing off at a grain size of 8 µm. In contrast, the η-free specimens had a broader scatter in grain sizes up to 15 µm. Large grains can cause crack initiation during fatigue and should be avoided [138]. Therefore,

η provided a good barrier preventing this to happen. Chapter 6.2 will give more details on the deformation mechanisms of η.

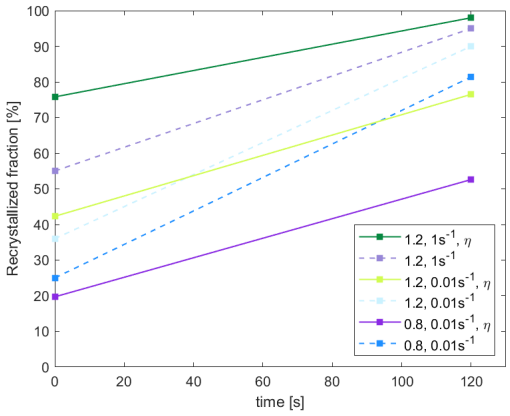

Fig. 4.24 Recrystallised fraction with time of η and η-free specimens

Figure 4.24 shows the recrystallized fraction with time. The η-containing samples are drawn in continuous lines and η-free are dotted. In terms of their gradient, the η microstructures have a shallower evolution than the η-free samples. This image suggests, that recrystallization in η-containing specimens slows down in comparison to the single phase microstructure. This could be simply based on the lesser stored energy available for MDRX which is generally represented by the exponential function of the JMAK-equation. In addition, it can be shown that η successfully pins the grain boundaries However, the packs of η were found to inhibit recrystallization between the laths. Figure 4.25 shows the IPF maps of all orientations obtained from transmission Kikuchi diffraction (TKD) of a TEM sample which was kept in the furnace for 120 s after the compression. The η particles are the white lines in the STEM-HAADF image and the unindexed areas in the IPF maps. Surrounding the η pack are recrystallized grains while within the laths the original grain orientation is still visible. In addition, there are no signs of formation of substructures between the laths which would be a precursor for recrystallization.

A remarkable difference in the grain size distribution could be observed between the η-containing and the η-free samples. The microstructure with the precipitates retained many small grains, even after the 120 s dwell time. The η-free samples developed a broader scatter during the hold. This observation goes in-line with the evolution of recrystallised area. The precipitates pin the grain boundaries hindering grain growth during MDRX. The area of small grains were located in the vicinity of the particles, giving the microstructure a heterogeneous nature. A heterogeneous microstructure can cause problems with stress concentrations in mechanical testing. Previous characterisation of a forged component stated

a large variation in η area fraction from 2 area% in the centre to 9 area% at the rim [25]. In terms of MDRX this scattering can lead to a wide scatter in grain sizes throughout the component. Hence, further analysis are required to investigate the mechanical properties of such a hetereogeneous microstructure.

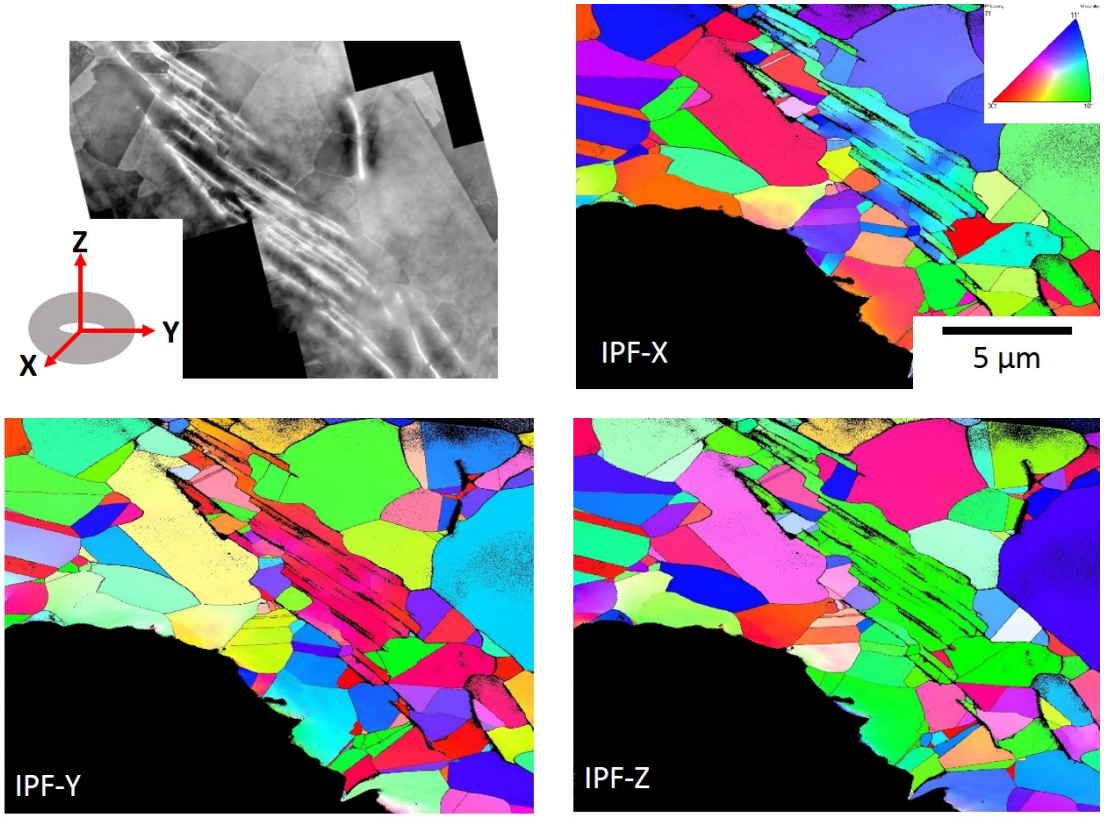

Fig. 4.25 TKD, IPF maps of a partially recrystallised area containing η-laths. Sample tested at 950°C, 1s^{-1}, ε=1.2 and a post-deformation dwell of 120 s.

In nickel-base superalloys heteroepitaxial recrystallization (heRX) was found as an additional recrystallization mechanism during high temperature testing [100]. It was claimed to form around primary γ' based on inverse precipitation from γ' to γ. An analytical study proposed that the key feature for heRX to occur is the ability to form a coherent particle-matrix interface [103]. In contrast to δ in IN718 η in 718Plus can form a coherent interface $[0001]_\eta||[111]_\gamma$. Figure 4.26 shows a STEM-BF image of a sample compressed at 975°C with 1s^{-1} to 1.2. The dark η precipitates are within a larger recrystallized grain. However, some particles have a dark gray area around them with a grain boundary between the surrounding large grain (red arrows). HeRX grains are supposed to be unstable and are consumed by growing grains [102]. As the presented image stems from a sample which

was exposed to MDRX, it seems to be unlikely that the observed feature is a heRXed grain. However, further studies are required to investigate the potential of heRX of η in 718Plus.

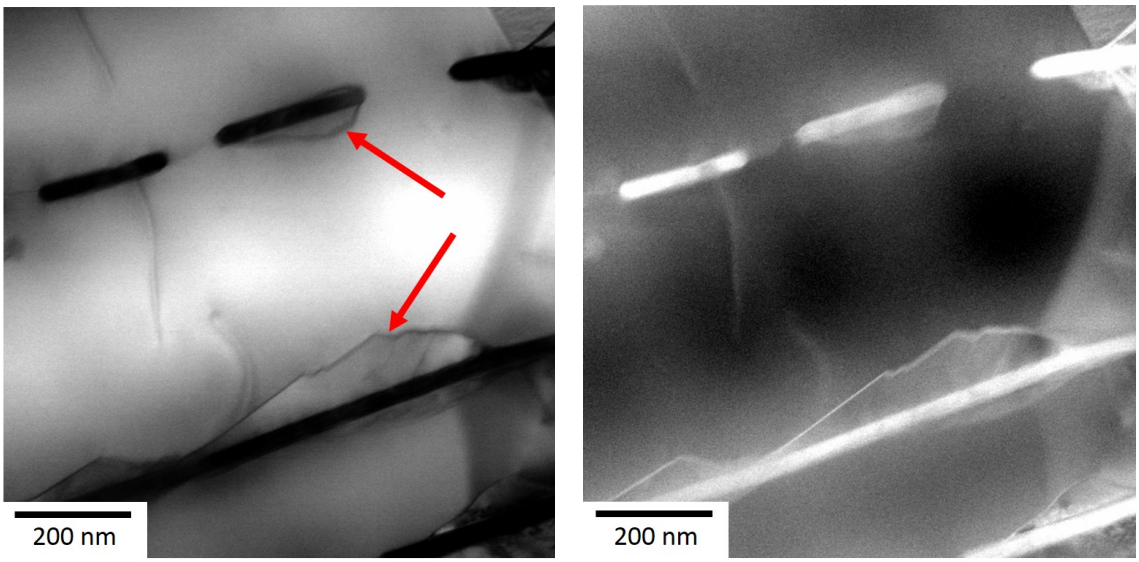

Fig. 4.26 STEM BF and high angle annular dark field (HAADF) images of η and surrounding recrystallization of the alloy tested at 975°C, $\dot{\varepsilon}$ 1s^{-1} and ε=1.2

4.4 Summary

The effect of deformation parameters on the kinetics of dynamic and meta-dynamic recrystallisation in 718Plus have been studied. A single- and two-phase microstructure was tested in order to analyse the influence of particles.

The recrystallised area increases with temperature, strain and strain rate. While the fraction of twin boundaries increases with temperature, the opposite was found for strain. This observation can be verified by the higher migration rate of high angle grain boundaries leading to an increase in stacking errors which can promote the formation of annealing twins. Evidence was also found for an increase in recovery for low strain rate deformation. In addition, DRX and MDRX could clearly be distinguished using TEM bright field imaging. The high recrystallised fraction with strain rate is likely to have resulted from MDRX occurring during the transfer time between deformation and quench.

In the two-phase microstructure, MDRX was hindered by dense packets of secondary η phase. As a result, η-containing samples showed a lower recrystallised fraction than its η-free counterparts after the 120 s dwell time. The η precipitates were also responsible for a

limited grain growth during MDRX. Heteropitaxial recrystallisation could not be verified in the specimens.

Chapter 5

Flow behaviour and recrystallisation kinetics

A thorough understanding of the recrystallisation mechanism during forging is essential to develop new manufacturing routines. In the previous chapter, dynamic and meta-dynamic recrystallisation of 718Plus with a single- and two-phase microstructure were quantitatively analysed. The influence of the testing parameters on the recrystallised fraction and other microstructural features was demonstrated. In the current chapter, this newly gained knowledge will be used to develop a basic empirical model for the application in industrial settings.

In comparison to IN718 [139], the flow behaviour of 718Plus has attracted little attention [14, 63]. In the first part of the chapter, the flow behaviour of 718Plus during forging conditions will be analysed. The effects of γ' will be highlighted and the influence of the testing parameters. Further to that, the role of η phase on the stress-strain curve has not yet been analysed. Therefore, the flow curves of the high temperature compression tests of the two microstructures are studied in terms of strain rate and temperature.

In the second part of the chapter, the Johnson-Mehl-Avrami-Kolmogorov (JMAK) approach is used to develop an empirical model. The simplistic nature of these equations make them attractive for finite element (FE) modelling in industry. Only two studies are currently known to have used JMAK for DRX of 718Plus, Momeni et al. [63] and Sommitsch et al. [22], both of which have solely studied a γ microstructure. This chapter will derive the modelling constants for the JMAK framework for DRX and MDRX of an initial γ-γ' and γ-η microstructure.

The compression tests and the conversion from load-stroke data to stress-strain curves of the γ-γ' microstructure were done by A. Casanova. The tests and subsequent conversion routines for the γ-η microstructure as well as any further analysis of the data were done as part of this work.

5.1 Post-processing and experimental validity

Stress-strain or flow curves from tensile or compression tests represent the material's response against elastic and plastic impact. Important static material parameters such as the yield point σ_Y can be extracted from these curves.

Material parameters can only be taken from samples which have deformed homogeneously. Hence, several shape parameters of the specimens after the test ensures that the execution of the experiments was within limits.

In order to obtain stress-strain curves tensile or compression tests can be performed. Details on the experimental set-up were given in Chapter 3. The raw data consists solely of the distance travelled from the stroke of the test equipment and the load applied on the dies. To convert the readings from the load-stroke format to stress-strain a number of steps need to be followed in order to generate a reliable set of data.

Firstly, the raw stroke reading needs to be corrected for machine compliance and setup-errors at the initial stage of the loading. The corrected load-stroke data can then be translated into a stress-strain curve using the sample geometry. In the current study, the compression tests were performed at high temperature which requires the knowledge of thermal expansion of the sample geometry. The next step is the correction of the stress data due to friction and adiabatic heating of the test piece. After all these modifications the material constants can be extracted from the flow curves. In the following, the detailed data cleaning procedures are presented and applied on the compression test measurements.

5.1.1 Experimental validity

Mechanical tests are standardised procedures to guarantee the repeatability and validity of the measurements. The high temperature compression tests in this study were performed in accordance to ASTM E209-00 [140]. The standard ensures that the test piece is deformed homogeneously throughout its dimensions. To prove the correct execution of the test, the deformation shape of the test pieces need to be within pre-defined limits. For compression tests these limits are set by the barreling, ovality, height and shear coefficient [141].

Barrelling coefficient

The barrelling coefficient is defined by

$$B = \frac{h_f d_f^2}{h_0 d_0^2} \tag{5.1}$$

where h_0 and d_0 are the initial height and diameter of the undeformed specimen and h_f and d_f are the final height and diameter of the test piece after the compression. The barreling coefficient determines if the sample has experienced friction between the contact areas and the test dies. To minimise friction and improve the homogeneity of deformation, the interfaces are coated with a lubricant. Values of B should be smaller than 1.10 to meet the criteria [141].

Ovality coefficient

The ovality coefficient defines the shape of the cross-section of the compressed sample and is determined by

$$O = \frac{d_{f_{max}}}{d_{f_{min}}} \tag{5.2}$$

From the four measurements taken at the same height, $d_{f_{max}}$ is the maximum and $d_{f_{min}}$ the smallest diameter measured.

Height factor

Similar to the ovality coefficient is the definition of the height factor:

$$H = \frac{s(h_f)}{h_f} \tag{5.3}$$

where $s(h_f)$ is the standard deviation of all four height measurements taken. The height coefficient ensures the parallelism of the sample during compression and must be smaller than 0.04. The height factor for all samples was excellent at 0.0.

Shear factor

The shear coefficient S determines, how much the axes of the undeformed and deformed sample deviate:

$$S = tan\theta \tag{5.4}$$

with θ being the angle between these two centre lines. A test is invalid for $S \leq 0.175$ resulting in a maximum angle θ of 10^o [141]. It is accepted to measure the deviation by an optical projection method which was the case for this study.

Table 5.1 presents the validity factors for all tests. The values for the η-containing samples can be found in the second half of the table and are indexed appropriately. All samples but one deformed according within the limits. The specimen compressed at 850°C with the highest strain rate of $1.0s^{-1}$ was out of limits of the ovality as well as barreling coefficient. Hence, the microstructure and the mechanical properties of this specimen need to be interpreted with care.

Table 5.1 Validity coefficients B and O and effective strain φ_{eff} for all specimens. B_η, O_η and $\varphi_{\eta,eff}$ are the values for the η-containing samples.

φ	T [°C]	$\dot{\varepsilon}[s^{-1}]$	dwell time [s]	B	O	φ_{eff}	B_η	O_η	$\varphi_{\eta,eff}$
0.76		0.01		1.07	1.04	0.77			
0.66	850	0.1		1.08	1.0	0.67			
0.87		1		1.1	1.13	0.74			
0.4	950	1		1.04	1.01	0.31	1.03	1.0	0.38
	975	1		1.03	1.0	0.31			
0.8	950	1		1.05	1.0	0.64	1.06	1.0	0.73
			120	1.05	1.0	0.63	1.07	1.0	0.75
	975	0.01		1.02	1.0	0.66	1.04	1.0	0.63
			120	1.03	1.0	0.66	1.05	1.0	0.61
		0.1		1.05	1.01	0.64			
		1		1.03	1.01	0.61			
			120	1.06	1.01	0.64			
	1000	0.01		1.02	1.01	0.66			
		0.1		1.05	1.02	0.67			
		1		1.04	1.01	0.66			
	1025	0.01		1.06	1.01	0.64			
1.2	950	0.01		1.0	1.01	0.97	1.06	1.01	1.02
			120	1.04	1.01	0.97	1.07	1.01	1.03
		0.1		1.03	1.02	0.94	1.07	1.0	1.01
		1		1.04	1.02	0.95	1.08	1.0	1.09
			120	1.06	1.01	0.91	1.09	1.0	1.09
	975	0.01		1.02	1.01	0.99	1.08	1.01	1.07
			120	1.03	1.01	0.97	1.07	1.01	1.04
		0.1		1.03	1.01	0.97			
		1		1.04	1.01	0.98	1.07	1.0	1.08
			120	1.06	1.01	0.94	1.07	1.0	1.09
	1000	0.01		1.04	1.01	0.96			
		0.1		1.04	1.0	0.96			
	1025	0.01		1.04	1.02	1.01			

The columns marked with φ_{eff} show the effective strain which will be calculated in the next section.

5.1.2 Correction of load-stroke curves

A number of external factors influence the load-stroke data of a compression test. To obtain the actual flow behaviour of a material, the data needs to be adjusted for these factors. This section provides a summary of all corrections done on the original data. While the corrections of the η-free data were made by Ana Casanova, the η-containing samples were cleaned by the current author.

Effective strain

The reported stroke was measured by a linear-variable-differential-transformer (LVDT) on the ram of the test equipment. The obtained values are falsified by effects due to the testing material, the test machine and sample geometry. Elastic and plastic displacement of the specimen can cause a significant error between the calculated strain from the test and the actual strain within the sample. The logarithmic strain φ used hereafter is calculated from the engineering strain

$$e = \frac{h_0 - h_f}{h_0} \tag{5.5}$$

by integration to

$$\varphi = \left| ln\left(1 - \frac{h_0 - h_f}{h_0}\right)\right| \tag{5.6}$$

and is commonly used for compression tests. Columns seven and ten in Table 5.1 present the strains φ_{eff} calculated from the reduction in height before and after the compression for the two microstructures. For a nominal reduction of 1.2 the plastic strain achieved in the sample was ~0.95, for 0.8 the sample strain was ~0.64 and an actual strain of 0.3 could be reached for measured strains of 0.4.

Machine compliance

The elastic and thermal displacement of the different parts of the test machine are summarised in a machine compliance error. This error was retrieved for temperatures 850, 950 and 1025°C for the η-free tests and interpolated for 975 and 1000°C. The η-containing specimens were tested at a later point in time and the compliance was measured for both testing temperatures, 950 and 975°C. The stroke readings were subsequently corrected for the machine compliance at the respective temperatures.

Correction of the origin

At the beginning of each test, the data logging system recorded a displacement while the

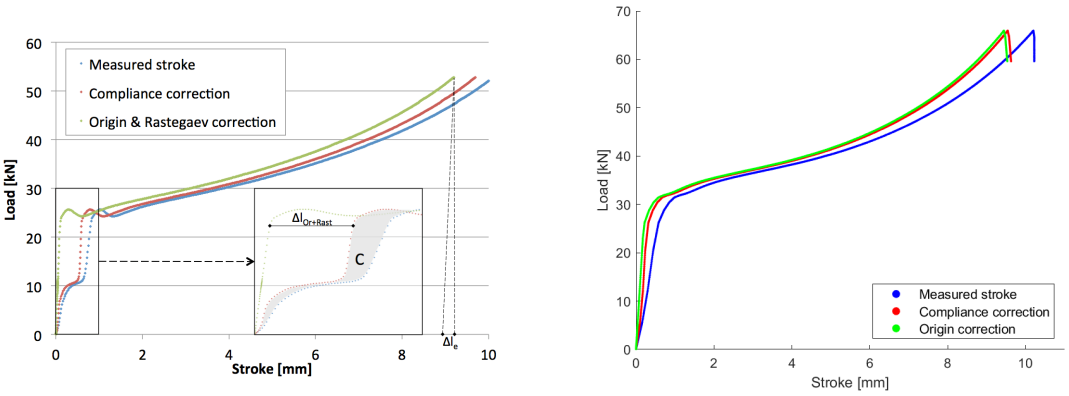

(a) (b)

Fig. 5.1 Correction steps in for the load-stroke curves. The curves are from specimens compressed with $0.1s^{-1}$ to 1.2 a) η-free tests at 975°C, image courtesy A. Casanova b) η data at 950°C

applied load stayed at a minimum. The source for this error are minor decentrations between the various parts of the machine which align themselves accordingly when some load is applied. Due to this effect, the origin of the curves need to be reset by shifting the whole curve along the stroke axis until the linear part initiated at the origin of the load-stroke diagram.

All three correction steps are given in Figure 5.1 for the η-containing and η-free microstructure.

Rastegaev shape correction

The specimens with the η-free microstructure were machined to a Rastegaev shape with grooves for lubrication on both ends (see Figure 3.1 in Chapter 3.2). This specific form causes a deflection in the elastic region of the load-stroke curve as the thin walls deform before the bulk of the sample. The error was corrected by calculating the elastic constant from the undisturbed part of the linear region. The elastic constant was then used to redraw the linear part of the curve and shift the data by the calculated strain values. The η-containing samples had the Rastegaev rims removed before the test which is why this correction was not applicable for this set of samples.

Conversion load-stroke to stress-strain

With all the errors listed, the corrected load-stroke curves were transformed into true stress-strain curves. The true strains were calculated using the corrected stroke data Δh_c and the

temperature adjusted initial specimen height $h_{0,c}$:

$$\varepsilon = \left| ln\left(1 - \frac{\Delta h_c}{h_{0,c}}\right)\right|. \tag{5.7}$$

Variable $h_{0,c}$ was calculated via $h_{0,c} = h_0(1 + \alpha \cdot T)$, α being the coefficient of thermal expansion extrapolated for the respective temperatures from the 718Plus Data Sourcebook provided by ATI Specialty Materials Ltd. [132]. Similarly, the temperature corrected initial specimen cross section $A_{0,c}$ was corrected with $A_{0,c} = A_0(1 + \alpha \cdot T)$ and together with load F used in the formula for deriving the true stress:

$$\sigma = \frac{F}{A_{0,c}}\left(1 - \frac{\Delta h_c}{h_{0,c}}\right). \tag{5.8}$$

Friction and adiabatic heating

The stress-strain curves derived with the outlined procedure can still not be compared with each other as they contain errors from friction between specimen and compression dies as well as adiabatic heating due to the induced deformation. Hence, the data will be adjusted to obtain frictionless and isothermal conditions.

Numerous models were developed to calculate friction and adiabatic heating for compression tests. They can either be modelled individually or via combined approaches. In the first place, separate concepts are presented following a combined method.

Friction at the sample/die interface spawns barreling of the specimen which itself leads to a heterogeneous distribution of stress and strain [142]. Friction also provokes a rise in load which causes the stress-strain curve to be shifted to higher stresses. Another consequence of friction on the sample conditions can be accruing heat. Zhao [143] analytically approached the topic of friction heat during compression for strain rates from 0.001 to 100s^{-1}. He concluded that due to the lubrication at the interface the heat generated by friction is neglectable compared to deformation heat. Interface friction can either be determined by direct measurements or calculated as a function of the barreling [144, 145].

Adiabatic heating of the specimen during deformation changes the temperature conditions for which the test was designed to be. The heating of the sample leads to smaller stress values than what the material is actually capable at a certain temperature. Hence, different approaches to correct for this discrepancy have been developed. The most common method is by using an adiabatic correction term [146]. This empirical factor however can be oversimplistic and lead to the a shift towards models considering FEM analysis [142, 147]. These models require a detailed knowledge of the thermodynamic conditions of the system which are usually difficult to establish.

In the current study, a combined correction approach was chosen which acknowledges the intertwined nature of friction and adiabatic heating. Therefore, an interpolation function was developed for high temperature alloys based on 3087 FE simulations[148]. The six variables required were functions of the specimen geometry, testing parameters and the barreling coefficient as a measure for friction. Figure 5.2 shows the initial and corrected flow curves for η free samples tested at 950°C.

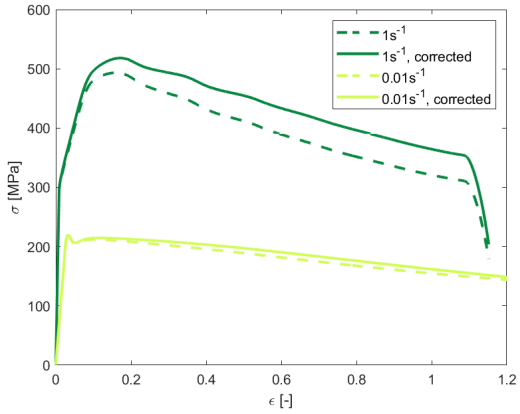

Fig. 5.2 Adiabatic and friction correction of the stress-strain curves for η samples at 975°C

The difference between the measured and corrected flow curves is small because friction and adiabatic heating seem to cancel each other out. While friction correction decreases the stress levels, adjusting adiabatic heating causes the stress to rise.

5.2 Flow behaviour of 718Plus

In this section, the flow curves of the high temperature compression tests will be presented subdivided in the two tested microstructure. The main results will then further be discussed in the subsequent section.

The corrected stress-strain curves of 718Plus of the initial γ-γ' microstructure are given in Figure 5.3 and the corresponding mechanical properties in Table 5.2. Each diagram represents a different temperature and shows the flow curves at the three strain rates. Table 5.2 lists the yield point σ_Y, the upper and lower yield stress $\sigma_{Y,U}$ and $\sigma_{Y,L}$ and the peak stress σ_P for the η-free and η microstructures.

The flow curves can be divided in two main stages, the elastic and the plastic region which are both outlined in the sketch at the top left corner of Figure 5.3. Stage I contains the linear-elastic area which is terminated by the yield point σ_Y. The yield stress σ_Y marks the end of the elastic region and is defined as the stress at 0.2% plastic strain. In the tested

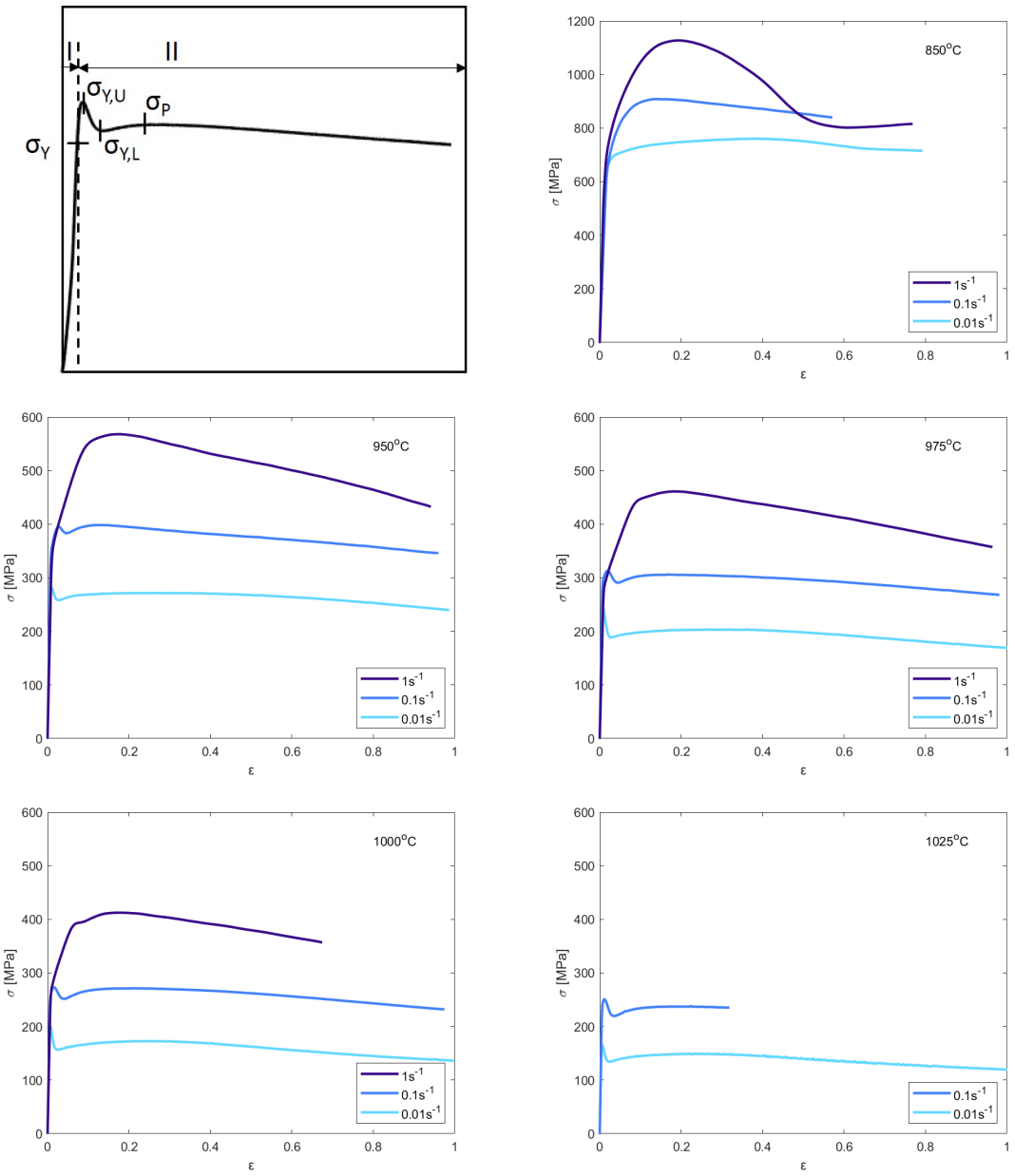

Fig. 5.3 Corrected stress-strain curves for η-free microstructure

Table 5.2 Yield stress, upper and lower yield point and peak stress for samples tested to maximum strain. The stress values are in MPa.

φ	T [°C]	$\dot{\varepsilon}$ [s^{-1}]	σ_Y	$\sigma_{Y,U}$	$\sigma_{Y,L}$	σ_P	$\sigma_{Y,\eta}$	$\sigma_{Y,U,\eta}$	$\sigma_{Y,L,\eta}$	$\sigma_{P,\eta}$
0.76		0.01	621			760				
0.66	850	0.1	646			908				
0.87		1	649			1126				
		0.01	268	281	259	271	285	297	268	277
	950	0.1	326	390	384	398	320			402
		1	347			568	357			594
		0.01	212	241	190	203	225	240	211	216
	975	0.1	284	307	292	306				
1.2		1	294			461	328			518
		0.01	173	179	157	173				
	1000	0.1	254	267	252	271				
		1	275			412				
	1025	0.01	145	161	135	149				
		0.1	249	251	220	238				

samples the yield stress is decreasing with temperature. While at 850°C and a strain rate of $0.1s^{-1}$ σ_Y reaches 646 MPa, the value drops by almost half to 326 MPa at 950°C. It further decreases to 284 MPa at 975°C, 254 MPa at 1000°C and 249 MPa at 1025°C. The large dip between 850 and 950°C can be attributed to partial dissolution of γ' at higher temperatures and the related loss in strength of the material.

The effect of strain rate has an inverse relation to the evolution of σ_Y. With fastening the strain rate at 950°C the yield point rises from 268 MPa at $0.01s^{-1}$ to 347 MPa at $1s^{-1}$. This is a consistent trend for all temperatures in the present study.

Following the yield point stage II, the plastic region, is reached. Two different transitions can be noticed in 718Plus. Firstly, a continuous increase in stress with strain up to the peak stress σ_P such as in the flow curves at 850°C. Secondly, the stress peaks at an upper yield point $\sigma_{Y,U}$ before declining to the lower yield stress $\sigma_{Y,L}$ which is then ceased in a second stress rise up to the peak stress. This phenomenon is referred to as yield point drop. The specimens compressed at temperatures higher than 850°C and with strain rates of 0.01 and $0.1s^{-1}$ all form a yield point drop. Even though the yield point drop is absent for the samples at $1s^{-1}$, the curve at 1000°C has a small dent around a strain of 0.15.

After the peak stress σ_P the flow curve consecutively decreases and potentially reaches a steady state. Analogous to the yield stress are the influence of temperature and strain rate on the peak stress. The peak stress becomes smaller with temperature but rises with strain rate.

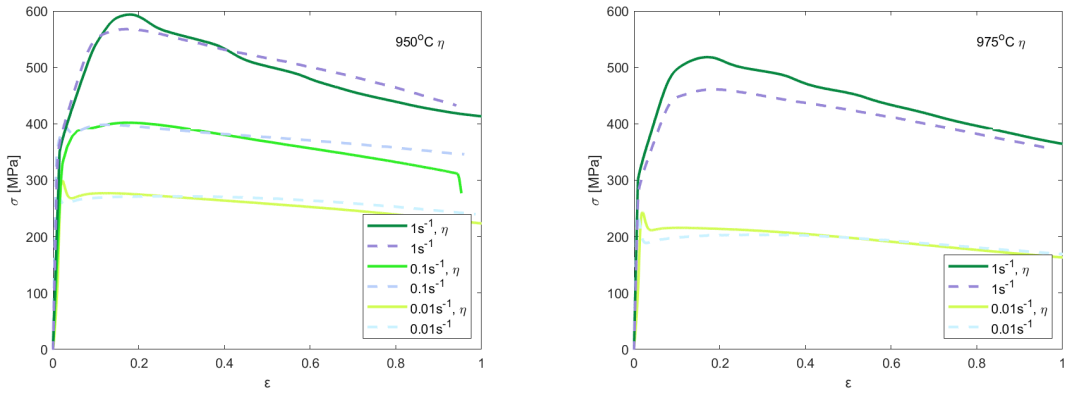

Fig. 5.4 Corrected stress-strain curves of η and η-free samples

The rate of flow softening succeeding the peak stress determines how much the material weakens with ongoing deformation. Reasons can be microstructural changes such as recrystallisation. Observing the flow curves this effect is stronger at higher strain rates.

Figure 5.3 solely considered the γ-γ' microstructure. Figure 5.4 is an overlay of the flow curves of the η-containing specimens as continuous lines with the η-free curves dotted. The supplementary flow parameters are on the right side of Table 5.2.

In line with the trends of the γ-γ' microstructure, the yield point of the η samples increases with higher strain rates and decreases with temperature. Comparing σ_Y of the two microstructures the η samples tend to have higher yield stresses. An exception is the test at 950°C and 0.1s^{-1} strain rate where σ_Y of the η-free equivalent is with 326 MPa slightly higher than η with 320 MPa.

As in the earlier results, the η specimens form a yield point drop at the lowest strain rate of 0.01s^{-1}and a monotonic flow curve at 1s^{-1}. However, the test at 950°C and 0.1s^{-1} lacks a yielding phenomenon which is present for the γ-γ' samples. Instead of a well-developed yield point drop the curve plateaus at ~0.08 strain with a faint dent. A similar feature was described for the γ-γ' specimen tested at 1000°C and 1s^{-1}.

The ultimate strength $\sigma_{P,\eta}$ at 950°C and 0.01s^{-1} is with 277 MPa slightly higher than σ_P with 271. In general, the peak stress for the η microstructure exceed the η-free one. The effect of strain rate and temperature on $\sigma_{P,\eta}$ is the same as for $\sigma_{Y,\eta}$ and the γ-γ' specimens.

Flow softening in the η samples after reaching the peak stress is greater than in η-free. The gradient of flow curve softening becomes smaller with lowering the strain rate.

5.2.1 Discussion flow curves

The as-described flow curves are characterised by a linear increase in stress up to the yield point, a possible yield point drop followed by a further rise in stress until they reach the peak stress which is terminated by flow curve softening. The upcoming discussion focuses on the general effect of η particles, the yield point drop and the flow softening behaviour of 718Plus.

The η-containing specimens produce a slightly higher yield stress than their single-phase counterparts. From the characterisation of the initial microstructure in Chapter 4.1.1 the initial grain size between η-free and η specimens differed by ~7 µm. Following the well-known relationship by Hall-Petch the microstructure with the smaller grain size (η) results in higher yield stresses. In the Hall-Petch relation the grain size strengthening term is defined as $\frac{k}{\sqrt{d}}$ where k is a material specific constant and d the grain size. For the tested samples the grain size for the η-free microstructure was measured to be 43 µm and in η-containing samples 36 µm. Assuming k to be 1 MPa m$^{1/2}$ [149], the strengthening term for the smaller grain size adds up to 167 MPa. For the larger grain size of 43 µm strengthening by grain boundaries is calculated to reduce by 9% to 152 MPa. The strengthening effect of the η precipitates could have a smaller influence due to the low volume fraction of η. The primary role of η particles is to pin the grain boundaries rather than hinder dislocation movement. From the present study, the individual influence of grain size and precipitates on the yield stress cannot be distinguished.

Yield point phenomenon

The relative yield point drop RYD was calculated using the upper and lower yield point:

$$RYD = \left(1 - \frac{\sigma_{Y,L}}{\sigma_{Y,U}}\right). \tag{5.9}$$

A graphical representation of the influence of temperature and strain rate on the RYD is shown in Figure 5.5. Such a yield point drop has been reported frequently in nickel-base superalloys such as 718Plus [150, 139, 63]. From Figure 5.5a it can be seen that for a constant temperature the yield point phenomena becomes stronger with slower strain rates. Considering the influence of temperature, the maximum yield point drop is shifted to higher temperatures when the strain rate gets faster indicating it is a time-dependent process. Even though the stress-strain curve at 1000°C for the highest strain rate of 1.0s^{-1} does not show a yield point drop, a noticeable dent around 400 MPa appears. Figure 5.5b is the evolution of yield point drops during high temperature compression tests from 718Plus calculated from the flow curves published by Momeni et al. [63]. The progress of RYD at a strain rate of 1s^{-1} continuous the trend from the present study. With higher temperatures the curve of 1s^{-1}

develops a yield phenomenon. In the current analysis the maximum yield point drop shifts to higher temperature with increasing the strain rate. Momeni et al. report the maximum RYD for the slowest strain rate $0.01s^{-1}$ at 1000°C, for 0.001 and $0.1s^{-1}$ at 1050°C and $1s^{-1}$ at 1100°C. Besides of the curve for $1s^{-1}$ the temperature ranges of the observed maxima between the present results and the published data by Momeni et al. are off by ~100°C. In addition, the tests with $0.1s^{-1}$ consistently produces the highest yield point drop irrespective of temperature.

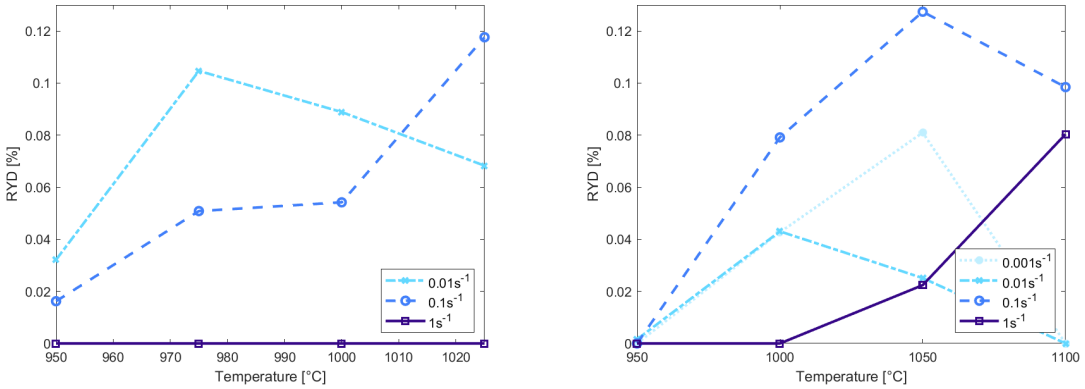

(a) This study (b) Calculated from Momeni et al. [63]

Fig. 5.5 Relative yield point drop

Potential reasons for a yield point drop can be changes in the microstructure such as recrystallisation or local obstructions in the dislocation movement.

Dynamic recrystallisation has been extensively studied in Chapter 4. At the minimum tested strain of 0.4 the recrystallised fraction was the lowest at 3% for a strain rate of $0.1s^{-1}$ and 15% for a strain rate of $1s^{-1}$. The yield phenomenon occurs at even smaller strains of ~0.1 where significant DRX is not to be expected. Another potential softening mechanism of the microstructure is adiabatic heating. The flow curves have been corrected for this and it can be seen from Figure 5.2 that there is no deviation from the actual values around the yield point while it gradually increases with strain. Hence, microstructural softening due to recrystallisation or adiabatic heating are unlikely to have taken place and cannot explain the yield drop.

Changes in the dislocation mobility can be caused by two possible scenarios. Firstly, dislocation movement is inhibited until a critical strain is reached at which point the dislocations can break free. This is characterised as the upper yield point. At the lower yield point the normal work hardening rate exceeds the softening by dislocation glide. Another possibility is a rapid generation of dislocations which allows the material to accommodate for the strain at a lower flow stress, causing a drop in the otherwise monotonic flow curve. Both mechanisms

can be provoked by a number of microstructural effects which will be discussed and related to the given examination.

For the first mechanism of hindering the dislocation movement, three different theories have been suggested so far. One of which is the precipitation of γ' at dislocations and stacking faults. These structures can act as obstacles for dislocations limiting their mobility. For the current case, this mechanism is not applicable as the vast majority of the tests were performed above the γ' solvus temperature of 718Plus of 967°C.

The second pinning mechanism proposed is due to a short range ordering (SRO) event of the disordered γ phase [151, 150]. Short range order is defined as the local ordering of a disordered matrix. In case of a nickel-base superalloy the ordered phase is the Ni_3Al γ'. It can occur rapidly but will dissipate if solute atoms from the matrix phase diffuse to these clusters. Considering the latter effect, slow strain rates would decrease the yield point phenomena in case of short range ordering. If anything the opposite is the case as the yield point phenomena is absent for the highest strain rate.

The final mechanism is the locking of dislocations by a Cottrell atmosphere or dynamic strain aging (DSA) which is the collection of solute atoms around dislocations [152]. This mechanism could explain the temperature and strain rate dependency of the yield point drop as it is diffusion driven. The higher the temperatures and the slower the strain rates the more time is available for solutes to diffuse to energetically favourable locations around defects. In the samples compressed at 850°C no yield point drop can be observed. Firstly, at these conditions the diffusion rate is lower compared to the other testing temperatures and secondly, the γ' particles denude aluminium and titanium from the matrix so they cannot form clusters around dislocations. This mechanism can partly be supported by considering the RYD of the η-containing samples. The RYD for these curves is added to the η-free values in Figure 5.6. As already mentioned in section 5.2, the yield point phenomenon is absent for the intermediate strain rate at 950°C. Niobium, titanium and aluminium build up η precipitates and hence are not in solution. However, if solutes with a tendency to form η would pin dislocations, the RYD should be smaller for the η specimens. In fact, at 950°C and $0.01s^{-1}$ the yield point drop of η testing exceeds this from η-free. Another general observation of dynamic strain aging needs to be considered as well. DSA is present at tensile tests with low strain rates in the temperature range between 200 and 600°C [153]. In addition, the mechanism is characterised by periodical drops throughout the flow curve as the solutes continue to diffuse to the dislocations and pin them. Neither the temperature range nor serrations in the flow curve can be detected for these samples. Therefore, a yield point phenomenon based on solute pinning of dislocations might not be a valid explanation.

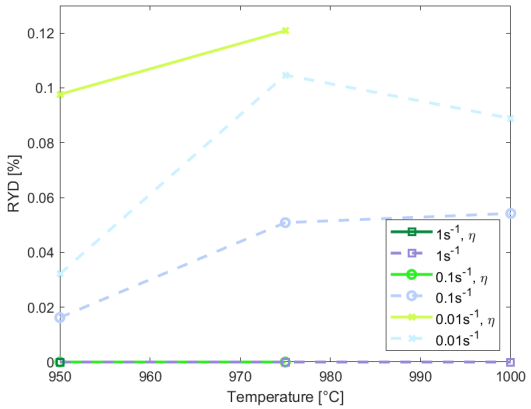

Fig. 5.6 Relative yield point drop in η and η-free samples

A second rational for a yield point drop by dislocations is the rapid multiplication of the same [154]. For example, the formation of Frank-Read sources is one of the possibilities for the fast generation of dislocations. An example of an operating Frank-Read source in 718Plus in presented in the upcoming chapter in Figure 6.10. For dislocation multiplication having a noticeable effect on the flow curve, the initial microstructure must have a low dislocation content. For the present samples, a TEM study of the microstructures of 718Plus in the various steps before testing revealed completely dislocation free grains throughout the TEM foils. Hence, it seems valid to propose a rapid multiplication of dislocations as the reason for the yield point drop in 718Plus.

Flow curve softening

Stage II in the flow curves is characterised by an increase in stress up to σ_P followed by a decrease. After the yield point, the dislocation density gradually increases and as they interact with each other hindering further movement. This is known as work hardening. However, the softening mechanisms of recovery and recrystallization are active in the same regime. The drop in the flow curves indicates that the softening effects dominate the rate of work hardening. Dynamic recrystallization is a continuous process and even if the microstructure is fully recrystallized it can undergo another recrystallization cycle if deformation continues. A single peak in the flow curve indicates that only one recrystallization cycle was in place while a wavy flow curve suggests multiple recrystallisation cycles. The ratio between the initial and recrystallized grain size is one of the factors which determines if a single or multiple peaks occur [37]. The relative softening coeffcient was calculated by

$$S = \left(1 - \frac{\sigma_{\varepsilon_{max}}}{\sigma_P}\right) \tag{5.10}$$

and shown for the η-free microstructure in Figure 5.7. Flow softening in the γ' samples at 850°C is more pronounced than for higher temperatures. Chapter 4 presented the recrystallised fractions where these samples only had less than 5% recrystallised microstructure. The flow softening in this case is therefore related to γ' shearing and other deformation mechanisms which will be presented in Chapter 6.

Figure 5.7 presents the relative softening coefficient of the η and η-free microstructure. The softening coefficient for η samples is higher than the respective η-free values. These differences can be attributed principally to the higher recrystallized fraction pointed out in Section 4.2.1. Additionally, η can break up and realign with to the material flow [33]. A detailed study on the deformation mechanisms of η will be given in Chapter 6.

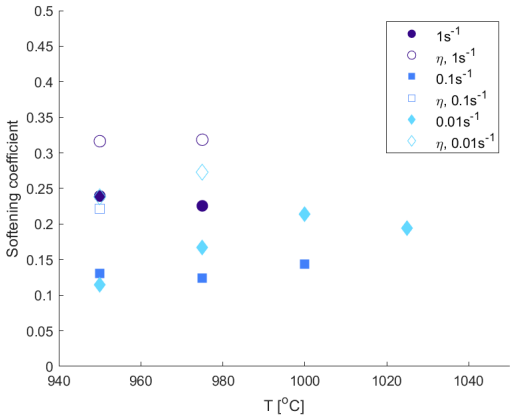

Fig. 5.7 Relative flow curve softening

5.3 Constitutive analysis

Finite element models require a good understanding of the material and their underlying response to stress and strain. For industrial applications such as forging simulations of turbine discs, the material model needs to be detailed enough to reproduce the important mechanisms but equally simple and quick to estimate so the overall calculation time of the component stays at an acceptable value.

The Arrhenius equation is frequently used to correlate the flow stress with the forging parameters. The knowledge of the flow stress across a range of temperatures and strain rates is a relevant part for load calculations. Besides the flow stress modelling, it is important to have some knowledge as to whether the component has fully recrystallised. Large, unrecrystallised grains can serve as a crack initiator during service of the component. In the field of dynamic

recrystallization the JMAK-approach has been used extensively for this application. Below, both frameworks will be applied on the data acquired in this study.

5.3.1 Peak stress modelling

The Arrhenius formulation consists of the Zener-Hollomon parameter Z with Q being the activation energy in kJ mol^{-1} and the universal gas constant R in kJ mol^{-1}

$$Z = \dot{\varepsilon} \cdot exp^{\frac{Q}{R \cdot T}} \tag{5.11}$$

Parameter Z can also be described as a function of stress and different approaches have been put forward [155]

$$Z = \begin{cases} A_1 \sigma^{n_1} \\ A_2 exp^{\beta \sigma} \\ A_3 \left\{ sinh\left(\alpha\sigma\right) \right\}^{n_2} \end{cases} \tag{5.12}$$

with the empirical material constants $A_1 - A_3$, n_1 and n_2, β and α. The first two variations are adjusted from creep modelling for low and high stress regimes. Sellars et al. [156] developed the third approach for a wider range of stresses with a hyperbolic sine function. The material constants for the different functions are determined as follows:

$$ln\left(\dot{\varepsilon}\right) + \frac{Q}{R \cdot T} = \begin{cases} ln\left(A_1\right) + n_1 \cdot ln\left(\sigma_P\right) \\ ln\left(A_2\right) + \beta \cdot \sigma_P \\ ln\left(A_3\right) + n_2 \cdot ln\left\{ sinh\left(\alpha\sigma_P\right) \right\} \end{cases} \tag{5.13}$$

The material constants n_1, β and n_2 in these equations are calculated from the ratios

$$n_1 = \left[\frac{\delta ln\left(\dot{\varepsilon}\right)}{\delta ln\left(\sigma_P\right)} \right]_T \beta = \left[\frac{\delta ln\left(\dot{\varepsilon}\right)}{\delta\left(\sigma_P\right)} \right]_T n_2 = \left[\frac{\delta ln\left(\dot{\varepsilon}\right)}{\delta ln\left\{ sinh\left(\alpha\sigma_P\right) \right\}} \right]_T \tag{5.14}$$

which can be read from the slopes of the graphs shown in Figure 5.8. The constant α is defined as β / n_1 and used in the hyperbolic sine function. In the next step, the values just derived are used to determine the activation energy for the three different frameworks:

$$Q = \begin{cases} R \cdot n_1 \left[\frac{\delta ln(\sigma_P)}{\delta(1/T)} \right]_{\dot{\varepsilon}} \\ R \cdot \beta \left[\frac{\delta \sigma_P}{\delta(1/T)} \right]_{\dot{\varepsilon}} \\ R \cdot n_2 \left[\frac{\delta ln\{sinh(\alpha\sigma_P)\}}{\delta(1/T)} \right]_{\dot{\varepsilon}} \end{cases} \tag{5.15}$$

Table 5.3 Activation energy and variables

β	n_1	n_2	α	Q_{sub} [kJmol^{-1}]	Q_{super} [kJmol^{-1}]	Q_{comb} [kJmol^{-1}]
0.0173	5.7191	4.2883	0.003	824	371	521

Figure 5.8 presents the curves from which the ratios are calculated. The evolution of the peak stress with temperature and strain rate differed for the samples tested at 850 and 950°C to those compressed at higher temperatures. With the γ' solvus temperature of 967°C the microstructure of the specimens at 850°C included strengthening precipitates which change the work hardening behaviour of the material. A TEM study on the samples tested at 950°C did not show any signs of γ' in the microstructure or diffraction pattern. The flow stress values of this set of samples was also considerably lower than comparable tests at 850°C. The Arrhenius plot shows a distinct change in the gradient at the γ' solvus. Hence, the activation energy for subsolvus behaviour Q_{sub} was calculated at 824 kJ mol^{-1} and supersolvus Q_{super} at 371 kJ mol^{-1}. In comparison, the activation energy for the temperature range from 950-1025°C was derived to Q_{comb}=521 kJ mol^{-1}. Activation energies reported for 718Plus varied based on the temperature range chosen. Momeni et al. [157] calculated Q=357 kJ mol^{-1} using data spanning from 950 to 1100°C. On the other hand, Huber et al. [158] distinguished between η sub- and supersolvus areas and stated an activation energy of 430 kJ mol^{-1} subsolvus.

The activation energy was initially developed assuming chemical processes where atoms diffuse and react with each other. The energy barrier for an atom to move to a vacancy position is then defined as the activation energy. Based on this definition, the activation energy for recrystallisation follows a different concept. While Q in the initial concept by S. Arrhenius defines a single process, i.e. atom diffusion, Q in the case of recrystallisation includes a number of processes which are necessary to successfully recrystallise a microstructure [159]. Firstly, recrystallisation starts off with pre-existing nuclei as already explained in Chapter 2.3. This is in contrast to the formation of e.g precipitates which requires the formation of a stable nucleus by single atom diffusion. Secondly, in the case of MDRX the available stored energy for the grain growth continuously decreases throughout the process. This also leads to an alteration in the apparent activation energy. Hence, the definition of the activation energy in recrystallisation should be detached from the original idea and it is more appropriate to consider it as an empirical constant for a variety of physical phenomenons.

Figure 5.9 relates the peak stress with the Zener-Hollomon parameter which itself consists explicitly of temperature and strain rate. For the given representation Z was calculated with the activation energy of either γ' sub-solvus (yellow) or super-solvus (red). Based on the definition, the Zener-Hollomon parameter increases with strain rate and decreases with

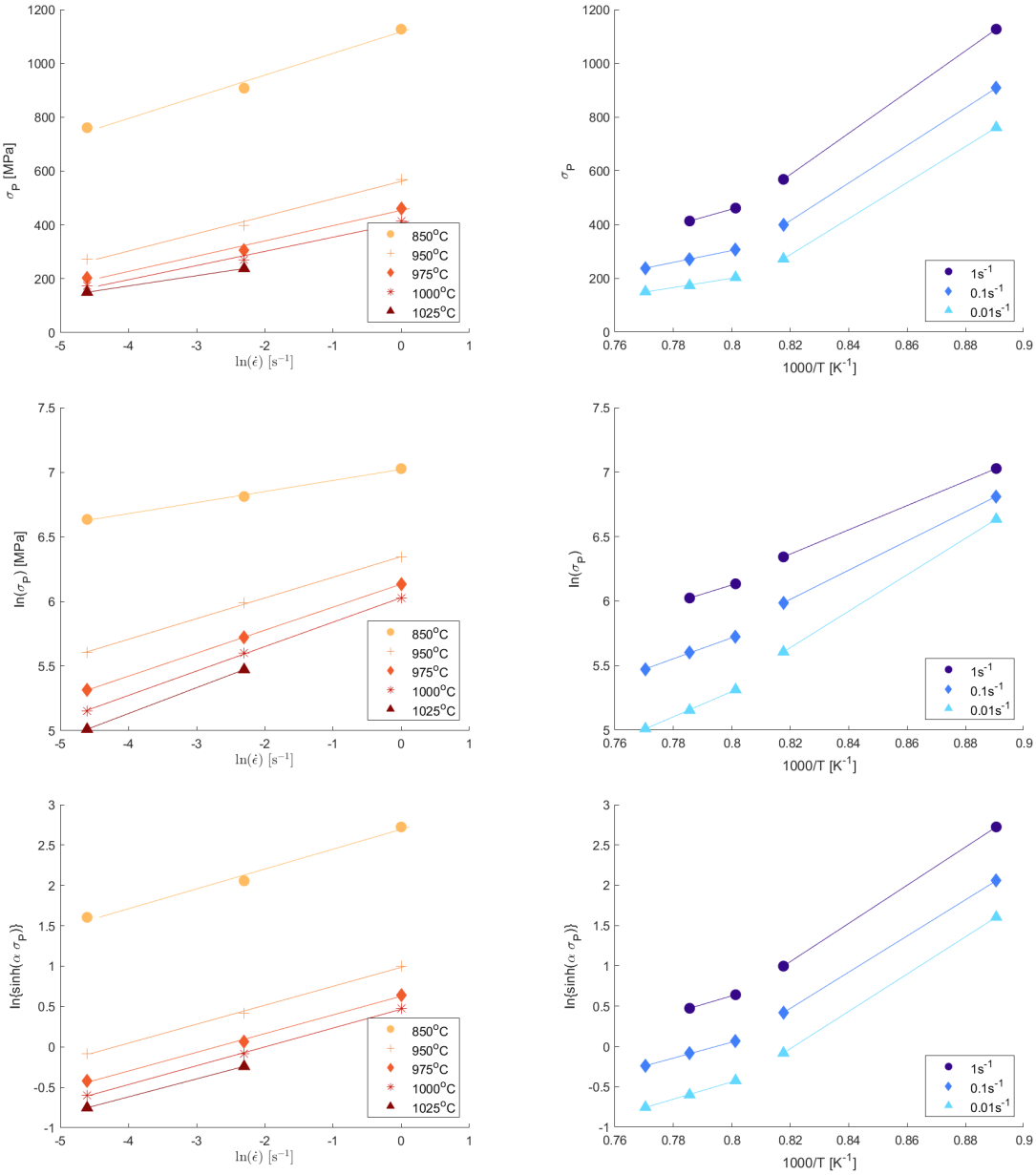

Fig. 5.8 Graphs for calculating the various constants for the Zener-Hollomon parameter

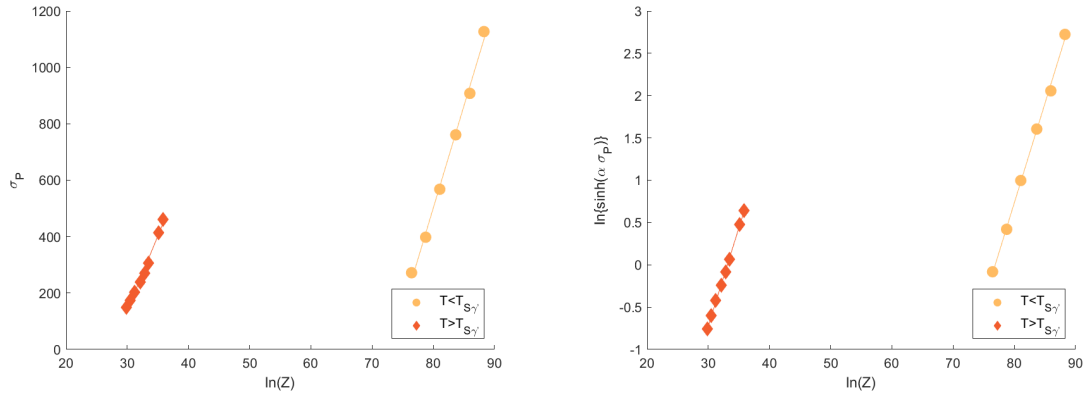

Fig. 5.9 Peak stress σ_P as a function of Zener-Hollomon parameter Z

temperature. Peak stress and ln(Z) have an almost linear relationship which serves as a good agreement of the calculated values with the experimental data.

The peak stress can now be redefined in the formula

$$\sigma_P = \frac{1}{\alpha} \cdot ln \left[\left(\frac{Z}{A} \right)^{1/n} + \left\{ \left(\frac{Z}{A} \right)^{2/n} + 1 \right\}^{1/2} \right] \tag{5.16}$$

which was derived from Equation 5.11 and 5.12.

5.3.2 Dynamic recrystallisation modelling

The kinetics of DRX is modelled with the JMAK approach where the recrystallised fraction X_{DRX} is described by

$$X_{DRX} = 1 - exp\left(-2f(x)^n\right) \tag{5.17}$$

where n is the Avrami exponent and $f(x)$ the time spent in dynamic recrystallisation. Factor $f(x)$ has been defined as a function of different strains with the exact function chosen by best fit to the available data

$$f(x) = f(\varepsilon) = \begin{cases} \frac{\varepsilon - \varepsilon_c}{\varepsilon_{ss} - \varepsilon_c} [160] \\ \frac{\varepsilon}{\varepsilon_{0.5}} [54] \\ \varepsilon - \varepsilon_c [63] \end{cases} \tag{5.18}$$

with ε_{ss} as the strain at steady state and $\varepsilon_{0.5}$ the strain at 50% recrystallisation. In this study the last description with the critical strain ε_c was used.

The critical strain is determined as the threshold for the onset of DRX. Poliak and Jonas [65] developed a framework to determine parameters such as the critical or steady state strain from the flow curve. The strain hardening rate $\theta = d\sigma/d\varepsilon$ is used to plot a $\theta - \sigma$ curve from which the variable can be read. The data in this study included the yield point drop at lower strain rates, which significantly influenced the accuracy of the reading. Various noise cleaning attempts were unsuccessful. It was decided that simply ignoring this feature would falsify the results to a great extent and hence a different approach was taken to determine the critical strain.

Various studies have defined the critical strain as a factor of the peak strain. One of the most common values is $\varepsilon_c = 5/6\,\varepsilon_P$ and was used for this analysis [54].

The Avrami exponent n was determined using a double logarithmic plot $ln\,[1/(1-X)]$ vs. $ln\,(\varepsilon - \varepsilon_c)$. Figure 5.10a presents the plots for the various temperatures and strain rates for the (a) η-free specimens and (b) their respective η-containing counterparts. The three values for each condition stem from the two tested strains of 0.8 and 1.2 and an additional strain was calculated by linear regression for the strain at which 50% of the microstructure is recrystallised.

The gradients from which the Avrami exponent is calculated scatter widely. For the η-free microstructure the tests at 1025°C/0.01s^{-1} and 975°C/1s^{-1} have the shallowest gradient. From them in ascending order are 975°C/0.01s^{-1}, 975°C/0.1s^{-1} and with the precipitous gradient the specimens deformed at 950°C and 1s^{-1}. Decreasing the temperature leads to steeper slopes as concluded from the following temperature pairs: for a constant strain rate of 1s^{-1} 950/970°C and the other at 0.01s^{-1} 975/1025°C. The effect of strain rate is absent of any clear pattern at 975°C as the gradient is the flattest for 1s^{-1}, intermediate for 0.01s^{-1} and the strongest for 0.1s^{-1}. However, these observations are in-line with the trends of the recrystallised fraction presented in Chapter 4.2.1.

The results from the η-containing tests are given in Figure 5.10b. The identification symbols were chosen according to the η-free labelling in (a). For this microstructure the spread in gradients between different conditions is narrower than for the η-free tests. At a condition of 975°C/1s^{-1} marked with the filled dots the slope is slightly shallower than for the other two conditions but the differences are very small. Contrary to η-free, dropping the temperature from 975 to 950°C results in a minimally steeper slope. Comparing the Avrami-gradients between the microstructures the η slopes at 975°C are steeper while at 950°C it is shallower than the η-free tests.

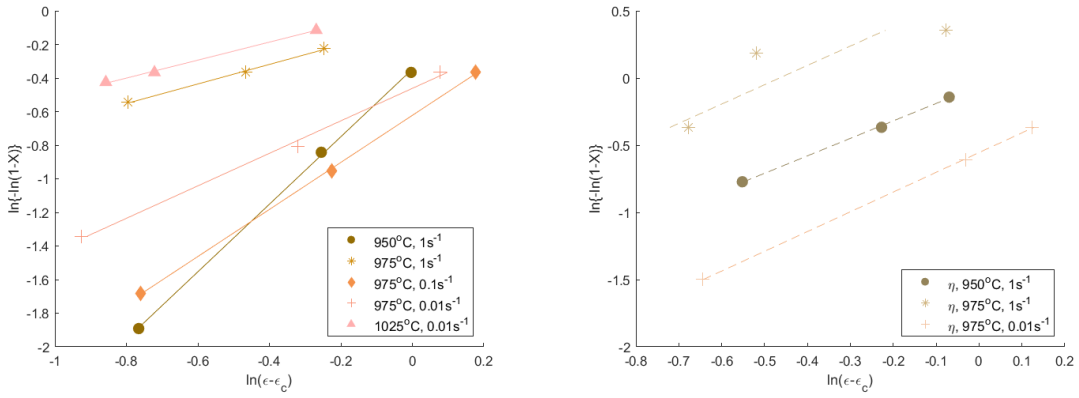

(a) η-free (b) η

Fig. 5.10 Avrami plots in the DRX regime

5.3.3 Meta-dynamic recrystallisation modelling

The JMAK approach can not only be used for the kinetics of dynamic recrystallisation but also meta-dynamic recrystallisation. While DRX was defined as a function of strain, MDRX evolves with time t at constant strain, strain rate and temperature. The function $f(x)$ then depends on $t_{0.5}$, the time when 50% of the microstructure is recrystallised

$$f(x) = f(t) = \frac{t}{t_{0.5}}. \tag{5.19}$$

MDRX is frequently determined by double-hit compression tests with varying interpass times [45, 109, 67, 161, 162]. The softening of the flow curve at the second hit can then be used to calculate the fraction of MDRX during the holding interval. The advantage of this method is a clear distinction between softening due to DRX vs. MDRX. For double-hit compression tests the time t for the JMAK function can be directly extracted from the test matrix. In contrast, single-hit compression tests with a dwell time after deformation combine the recrystallised fraction of MDRX with the preceding DRX. Simply subtracting the recrystallised fraction of MDRX with the respective value of DRX is misleading as the evolution of MDRX slows down with increasing recrystallised fraction. Hence, the time used in equation 5.19 is the total test time. As an example, consider a test with a strain rate of 1 $s^{-1}$to a strain of 1.2 of the present samples. The compression itself takes 0.7 s. Including the transfer time to the sample quench of 5 s equals to a total of 5.7 s at which the microstructure was recrystallising. The samples referred to as 'MDRX' had an additional 120 s in the furnace before the quench resulting in a total time of 125.7 s. In comparison, a test with a strain rate of 0.01 s^{-1}leads to a total test time of 75 s for an immediate quench and 195 s

with the furnace dwell time. Even though the as-described approach mixes the definition of the metallurgical terms of DRX and MDRX, it has its advantages for the application of the model. A combined equation for recrystallisation rather than two separate ones reduces time and necessary fitting parameters in an FE model. However, the different kinetics of MDRX and DRX cannot be accurately represented. To accommodate for this issue, the results will be presented under the term 'D/MDRX'.

MDRX is the growth of dynamically recrystallised grains at the expense of the stored energy by dislocations after the deformation has ceased. The amount of energy available depends on the strain at which the compression was stopped. As such, the kinetics of MDRX depends on the strain. Figure 5.11 presents the double logarithmic plots to obtain the Avrami exponents for the calculation of the recrystallised fraction. The graphs on the left are from the η-free microstructure and the right side is allocated to the η samples. The results for the low strain of 0.8 are on the top and for 1.2 at the bottom.

The D/MDRX kinetics for the η-free microstructure strained to 0.8 is given for three combinations of temperature and strain rate. The gradient for 950°C/1s^{-1} is the flattest and slightly increases with rising the temperature to 975°C. Dropping the strain rate from 1 to 0.01s^{-1} at 975°C leads to an even steeper gradient.

Now comparing the as-described results to the Avrami-plots at the higher strain of 1.2. The testing conditions of 950°C/1s^{-1} and 975°C/0.01s^{-1} caused a similar slope for a strain of 1.2 and 0.8. However, D/MDRX appears to slow down for 975°C/1s^{-1} at a higher strain. It should be remembered, that these samples had the highest absolute recrystallised fraction after DRX.

The respective η specimens are shown in Figures 5.11b and d. The relative difference in the samples at a strain of 0.8 between the η and η-free microstructure are small with marginally flatter slopes in general. The same trends can be drawn from the higher strains.

From both plots the samples compressed at lower strain rates seem to have a steeper gradient compared to the higher strain rates. The combined approach for RX mechanisms can over- or underestimate a particular kinetic behaviour. It as already been considered in Chapter 4, that samples at higher strain rates are more affected by the quench delay than at lower strain rates.

5.3.4 Discussion of the recrystallisation model

The activation energy was derived using the Zener-Hollomon parameter. Based on the slopes of the respective curves, the activation energy Q was divided in a γ' sub- and super-solvus regime. Table 5.4 compares Q of different studies.

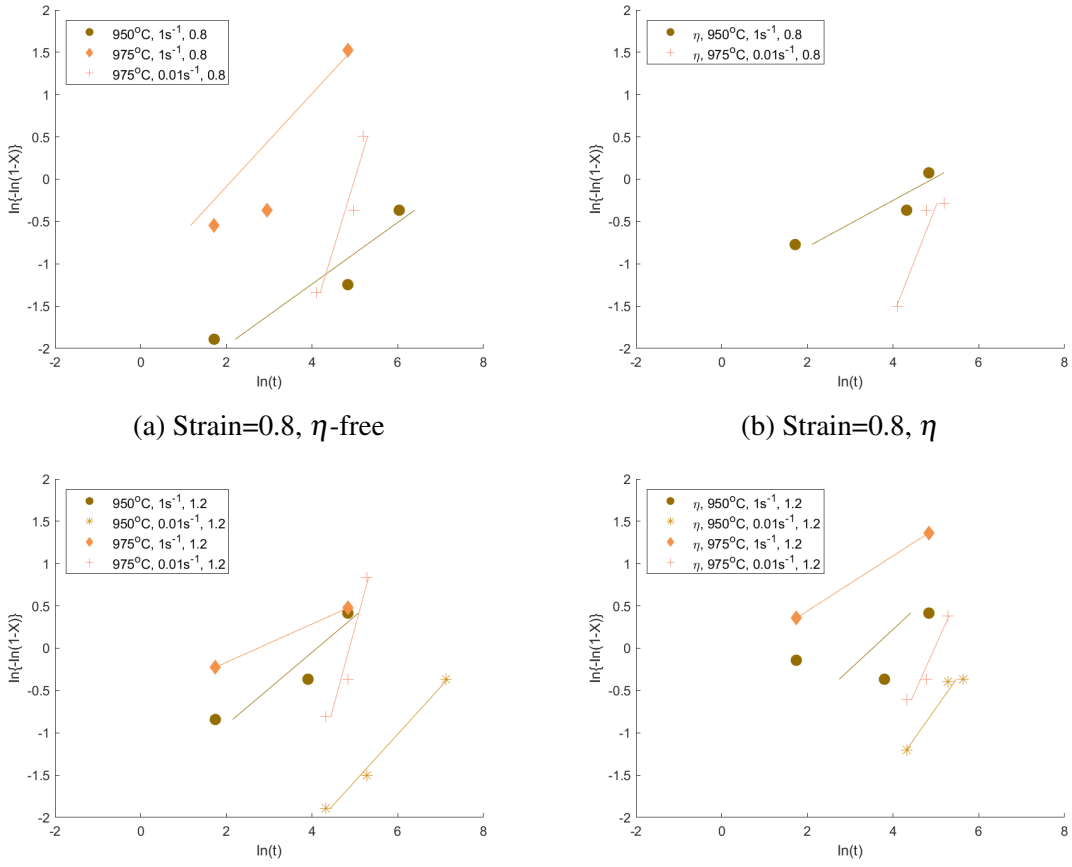

(a) Strain=0.8, η-free

(b) Strain=0.8, η

(c) Strain=1.2, η-free

(d) Strain=1.2

Fig. 5.11 Avrami plots for η-free and η samples in the D/MDRX regime for strains of 0.8 and 1.2

Q [kJmol^{-1}]	Temperature range [°C]	Reference
521	950-1025	
824	850-950	this study
371	975-1025	
430	900-1050	[158]
421	950-1100	[63]
525	900-1050	[163]

Table 5.4 Activation energies for η-free samples

The dependence of the activation energy with temperature shows that the samples compressed at 950°C are slightly off the trend between 975 and 1025°C. With a γ' solvus temperature of 967°C, the tests at 950°C are starting to dissolve. The specimens at 950°C were analysed in different TEMs multiple times but the diffraction patterns only showed γ spots. One possible reason considered was that during the foil preparation γ' was removed by the electro-polishing. This effect could be observed in some samples deformed at 850°C. In such samples the γ' superlattice diffraction spots were absent in the thin regions. However, the initial location of the precipitates was clearly visible by leaving dents in the γ matrix. Comparing this effect to the 950°C specimens their microstructure resembled the smooth appearance of a single-phase γ matrix. It could be possible though that short range order was present in these samples. Such small clusters of an ordered γ' structure could act as obstacles for dislocation movement.

After deriving the activation energy for the onset of dynamic recrystallisation, the JMAK approach was applied to determine an empirical function for the DRX kinetics of 718Plus The Avrami exponent was calculated from the presented X-f(ε) graphs and given in Table 5.5. The values vary between 0.53 and 2 in the η-free samples and 1-1.5 in the η specimens. A detailed analysis of the evolution of the slopes/exponents has already been given in Section 5.3.2. Hence, the discussion will focus on relating the calculated Avrami exponents with previously found data. Table 5.5 compares the Avrami exponents from different studies. Countless studies have been published discussing the value of the Avrami number and its potential meaning for the kinetics of dynamic recrystallisation.

Momeni et al. [63] were one of the few who analysed DRX in 718Plus. They observed a trend in the n value with the Zener-Hollomon parameter. At low and high Z values n constantly decreased while in the intermediate regime it rose. It was suggested, that this was due to the change in DRX mechanism from discontinuous DRX (dDRX) to continuous DRX (cDRX). For the present samples, the Avrami exponent increases with Z. However, the samples tested at 975°C and 1 s^{-1}contradicts the trend. As already shown and discussed

Table 5.5 Avrami exponents for η-free and η samples in the DRX regime

Alloy	T [°C]	$\dot{\varepsilon}$ [s^{-1}]	n	n_η	Reference
718Plus	950	1	2	1.3	this study
	975	1	0.58	1	
	975	0.1	1.4		
	975	0.01	0.96	1.5	
	1025	0.01	0.53		
IN718	900-990	0.1-10	3.34		[22]
	990-1050	0.1-10	0.88		[22]
	950-1100	0.001-1	0.8-3.5		[63]
	950-1100	0.001-1	1.1-3.2		[63]
	960-1020	0.001-1	0.934		[164]
	925-1070	$5*10^{-4}$-10	1.68-1.90		[165]
Waspaloy	1010-1027		3-1.8		[54]

in Chapter 4, the differences in cDRX and dDRX for low stacking fault materials are of a theoretical nature rather than what is directly observed in the material. Extensive subgrain formation was found in this study in samples strained at high as well as low strain rate samples which is in general associated with cDRX. DRX by grain boundary bulging is a mechanism attributed to dDRX which should occur during high strain rate tests but was also verified at a strain rate as low as $0.01s^{-1}$ in Chapter 4.2. Hence, a change in DRX mechanism is not supported by the direct evidence presented here.

The Avrami exponent is highly sensitive to small changes in the input data. Changing the recrystallised fraction by only 5% can increase the value of n from 0.53 to 1.0. This error can be circumvented either by extending the area of interest from which the recrystallised fraction will be calculated and/or increasing the number of testing parameters. Both methods are typically found for JMAK analyses. It is worth emphasising that the statistically recommended number of grains of 500 for microstructural analysis was always met in this study [166]. Nevertheless, considering the span of reported n values as listed in Table 5.5, a discussion of a 'correct' Avrami exponent is optimistic. The JMAK theory was developed assuming a homogeneous nucleation of grains throughout the microstructure. While this issue has partly been resolved for heterogeneous nucleation [167], the dynamic nature of DRX as well as the heterogeneity of the stored energy differ fundamentally from the baseline assumptions of the JMAK theory [168, 49].

Table 5.6 presents the Avrami exponent for the D/MDRX regime. Two different calculations were performed: the one labelled n_5 is measured including the 5 s transfer time as part of total recrystallised time and n is calculated without this time. As expected, including the transfer time had a bigger impact on tests with fast strain rates. From the presented values,

Table 5.6 Avrami exponents for η-free and η samples in the D/MDRX regime

ϕ	T [°C]	$\dot{\varepsilon}$ [s^{-1}]	n	n_5	n_η	$n_{5,\eta}$
0.8	950	1	0.2	0.32	0.13	0.23
	975	0.01	1.5	1.5	1.1	1.2
		1	0.36	0.69		
1.2	950	0.01	0.54	0.55	0.66	0.68
		1	0.21	0.37	0.06	0.14
	975	0.01	1.6	1.7	1	1
		1	0.14	0.23	0.2	0.33

there is a difference between high and low strain rates. The recrystallisation time used to calculate the values included not only the post-deformation dwell time in the furnace but also the time of the compression test, as outlined in Section 5.3.3. Therefore, the effect of the 120 s dwell time is a higher percentage of a test which only lasted 0.7 s than for one which took 70 s. Hence, the difference in recrystallisation mechanisms between DRX and MDRX is inherent to the Avrami exponent however speedy the quench. The n values for MDRX were reported to be lower than for DRX, but due to different testing methods and subsequent definition of recrystallisation time a comparison with these values is misleading [67, 54].

5.4 Summary

In the present chapter, the flow curves of the high temperature compression tests on 718Plus were presented and analysed. The raw test data of the γ-γ' specimens was converted to stress-strain curves by A. Casanova. The same procedure was followed for the γ-η microstructure and was part of this study as was any subsequent analysis.

For the γ-γ' microstructure, the mechanical properties clearly reflected the presence and absence of the strengthening γ'. The η phase affected the flow curve softening due to the increase in DRX. A yield point drop could be observed in samples deformed at lower strain rates and was suggested to stem from a rapid multiplication of dislocations.

The activation energy for the onset of 718Plus was found to be higher for γ' containing specimens than for the single γ phase. A JMAK-based model has been developed for DRX and MDRX differentiating between an η and η-free microstructure. The trends of the Avrami exponent could not be related to any testing parameter but was generally found to be higher in the η-containing samples. This observation was correlated to the low number of varied samples for each parameter. However, the calculated constants are perfectly valid for the conditions tested and are ready to be implemented in industrial forging simulations.

The trends of the Avrami exponent with the testing parameters were carefully examined. Based on the observations of the microstructure in Chapter 4, the discussion refrained from relating patterns in the calculated exponents with a change in DRX from dDRX to cDRX or vice versa.

Chapter 6

Deformation mechanisms

A thorough understanding of deformation mechanisms is an essential part of improving the properties of current materials as well as developing new alloys. Material models calculating the life of a component rely on knowledge of the microstructural mechanisms in place. These mechanisms depend on the phases present and their behaviour under deformation. Hence, this chapter focuses on deformation mechanisms in the γ-γ' microstructure and a study on how η phase accommodates the strains during hot forging.

The first part of this work considers deformation twinning in the matrix phase γ and γ-γ'. The effect of the testing parameters on the propensity for twinning was studied using TEM. Alongside the quantification, the twin formation will be discussed.

The deformation of η phase is the subject in the second part of the chapter. It will be presented in detail how η accommodates for the strain in the microstructure.

6.1 Deformation twinning

Deformation twinning is a deformation mechanism frequently observed in hcp materials and other metals with a low order of symmetry [169]. It can be found in ccp alloys when deformed at low temperatures and/or high strain rates [170]. Surprisingly, 718Plus was found to form deformation twins at temperatures up to 1025°C and strain rates as low as $0.01s^{-1}$. This study presents and discusses deformation twinning in a nickel-base superalloy at high temperatures and low strain rates for the first time.

6.1.1 Review on deformation twinning in ccp alloys

The associated characteristics of deformation or mechanical twinning in alloys are a combination of high tensile strength and elevated ductility [170]. In ccp materials deformation

twinning is frequently observed at low temperatures and/or high strain rates [171–173]. The propensity of deformation twinning of high temperature alloys under forging conditions (temperatures>800°C and strain rates ~$0.1s^{-1}$), is yet to be characterised.

Nickel-base superalloys are well known for forming microtwins during creep at temperatures between 650 and 750°C [174]. Twins have also been studied during thermomechanical fatigue testing of single-crystals at temperatures up to 1000°C [175, 176]. In these alloys, deformation twins are typically found at room temperature or even at cryogenic temperature [177]. However, only a few cases of deformation twinning at high temperature compression tests have been reported [178] [59]. In the nickel-base superalloy UNS10276 twins were found after compression tests at temperatures as high as 950°C and strain rates of $10s^{-1}$ [178]. The tests at strain rates between 0.01 and $1s^{-1}$ did not show deformation twinning. Similar observations were made for Alloy 617B. Deformation twins started to form at relatively high strain rates of 10 and $20s^{-1}$ [59]. As with the study by Pu et al. [178], deformation twinning was not reported at lower strain rates of 0.01, 0.1 and $1s^{-1}$. It is common to both studies is that the twins were only found at high strain rates.

Other alloy systems with a ccp structure have been analysed for their tendency for deformation twinning at high temperatures and low strain rates. Twinning induced plasticity (TWIP) steels, for example, were designed to deliberately form deformation twins leading to high ultimate tensile strength and a high ductility [170]. For this type of material it could be shown that they twin even at lower strain rates at high temperatures. A study on a transformation induced plasticity (TRIP)-TWIP steel showed deformation twinning during compression tests at strain rates of $0.01s^{-1}$ up to a temperature of 900°C [179]. While the martensitic transformation was operating at temperatures below 150°C, deformation twins were observed in the temperature range from 150-900°C. Eskandari et al. associated the twin formation with simultaneous carbide precipitation which depletes the matrix carbon and therefore locally decreases the stacking fault energy [179].

Another ccp alloy system is TiAl. TiAl is known for twinning at temperatures of 750-800°C [173]. TiAl forms lamellae of ccp grains which can serve as a local stress concentrator. It was recently reported, that based on the constraint of grain boundaries deformation twins are frequently observed in TiAl [180].

Deformation twinning in ccp materials involves the formation and propagation of the same Shockley partial a/6<112> on consecutive {111} planes each leaving behind a stacking fault [181]. A number of models have been proposed and reviewed to explain the nucleation of these partials [79, 182, 173, 170]. Twinning partials are supposed to be formed by cross-slip of dislocations in pile-ups, various dislocation reactions within a pile-up or emitted directly from grain boundaries.

6.1.2 Microscopy study of twinning in 718Plus

In this study the deformation mechanisms of 718Plus after high temperature compression tests are analysed. The specimens have already been extensively quantified on their recrystallisation behaviour in the previous chapters. It should be remembered at this point, that only the samples deformed at 850°C remained the γ' precipitates. In the samples tested at all other temperatures γ' dissolved completely and even upon quenching the γ matrix was the only detectable phase.

Stacking fault energy

The stacking fault energy (SFE) of an alloy determines how far the partial dislocations can separate while gliding through the crystal. The lower the SFE, the larger the distance. As deformation twins consist of overlapping stacking faults a low SFE is required to initiate twinning and also give a low coherent twin boundary energy. The stacking fault energy for the γ matrix of nickel-base superalloys are reported to be in the range of 20-30 mJ m^{-2} but can be as low as 11 mJ m^{-2} for the single-crystal experimental alloy UMF and as high as 40 mJ m^{-2} for the polycrystalline U720Li [183–185]. The stacking fault energy of 718Plus has not been reported yet.

Estimating the SFE can be done by either measuring the distance between two partials or their curvature at a triple junction as outlined on Figure 6.1a. With the latter method the stacking fault energy γ_{SFE} follows the relationship: [186]

$$\gamma_{SFE} \cong \frac{Gb^2}{4\pi d} \tag{6.1}$$

with G being the shear modulus, b the Burgers vector and d the equilibrium spacing of the partials. Distance d can further be defined by $R \approx 6d$ with R as the radius marked in Figure 6.1b.

The radii of two triple junctions shown in Figure 6.1b were selected to calculate the stacking fault energy of 718Plus. The constants in Equation 6.1 were the following: G at 975°C=60 GPa [132] and b=a/6$\langle 112 \rangle$ with the lattice parameter a=3.596Å [13]. Table 6.1 lists the measured radii and estimated SFE.

Microstructure of the deformed state

A typical example of the microstructure after the test is shown in Figure 6.2a. This TEM bright field (BF) image shows a recrystallised grain (numbered 1 and 2) adjacent to a deformed grain (3). Part 1 of the recrystallised grain includes dislocations as expected for a dynamic recrystallisation process. When a new grain forms and continues growing, the dislocation density in this grain will increase due to the ongoing deformation of the sample. Section

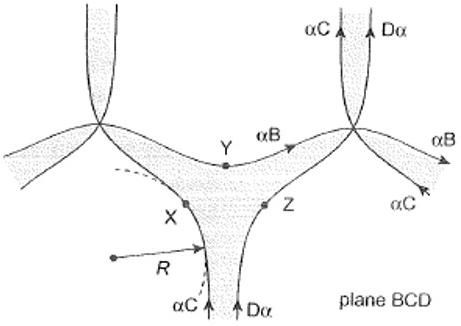

(a)

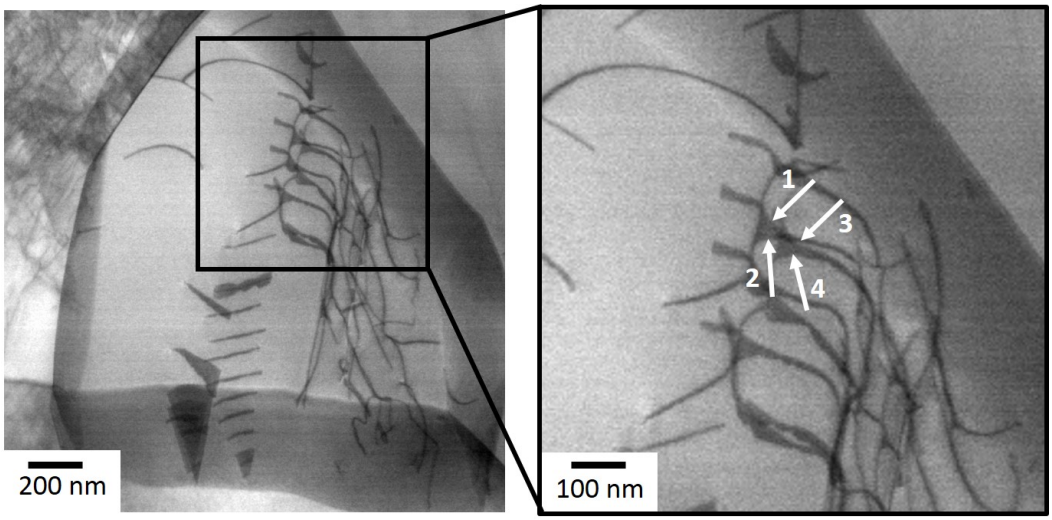

(b)

Fig. 6.1 (a) Theoretical measurement of the SFE on stacking fault nodes adapted from [186]. (b) Measured radii at stacking fault nodes in a sample deformed at 975°C.

Table 6.1 Radii and calculated stacking fault energies for γ in 718Plus

Radius #	R[nm]	γ [mJ m^{-2}]
1	48.5	12.7
2	42.4	14.6
3	36.4	17.0
4	40.4	15.3

1 and 2 are connected via an annealing twin boundary. Annealing twins are commonly observed during the growth of recrystallised grains at the given testing conditions [47, 187]. The contrast in the second part of the grain is homogeneous, showing no signs of dislocation activity. Hence, this part must have grown within the 5 s transfer time after the deformation finished and before the sample was quenched. This mechanism is generally referred to meta-dynamic recrystallisation. The deformed grain labelled 3 shows a high dislocation density with bend contours and fine packets of twins. Figure 6.2b shows a STEM-BF image and the respective diffraction pattern (DP) from region 3 of Figure 6.2a. The dislocation density and arrangement is due to the work hardening taking place during deformation. In addition, the present grain underwent twinning as part of the deformation process.

Figure 6.2c presents a twin leading into a recrystallisation nucleus in grey at the bottom. This specimen has been compressed at 1025°C to a strain of 1.2 with $0.01s^{-1}$. The lenticular shape of the twin as well as the dislocations at the boundaries indicate that this is a deformation twin rather than one of the annealing twins commonly formed during recrystallisation.

Figure 6.3 shows the STEM-HAADF (high angular annular dark field) image of a twinned and deformed grain from a sample deformed at 950°C with $1s^{-1}$ to a strain of 1.2. Deformation twins have formed together with low-angle grain boundaries. In addition, the grain consists of a high dislocation density which was generated during the compression. The diffraction pattern of this grain is presented in the top right corner and various close-ups of certain features are presented alongside. Subfigure 1 shows deformation twins which can be distinguished from other grain boundaries due to their straight interfaces. As observed in other samples, these twins are narrow. Dislocation interactions can be seen in subfigure 2. Several arrangements similar to a chain-wire-fence are visible. These are cross-slip events and the starting formation of a low-angle grain boundary. In subfigure 3 the white, thick lines are low-angle grain boundaries. In contrast to twin boundaries, low-angle grain boundaries can be bent and the interface varies in thickness. Parts of the boundary also show the dislocation network typical for twist boundaries. The pictured grain perfectly represents the main deformation mechanisms which are active at the conditions tested. Deformation twinning occurred alongside the climb of dislocations and their assembly into low-angle grain boundaries.

Further microstructural elements observed were stacking faults (SF) and dislocation pile-ups (Figure 6.4). Stacking faults are created by a/6<112> partials, the same which are involved in the formation of deformation twins.

Influence of forging parameters on the deformation mechanisms

High-temperature compression tests were performed above and below the γ' solvus tem-

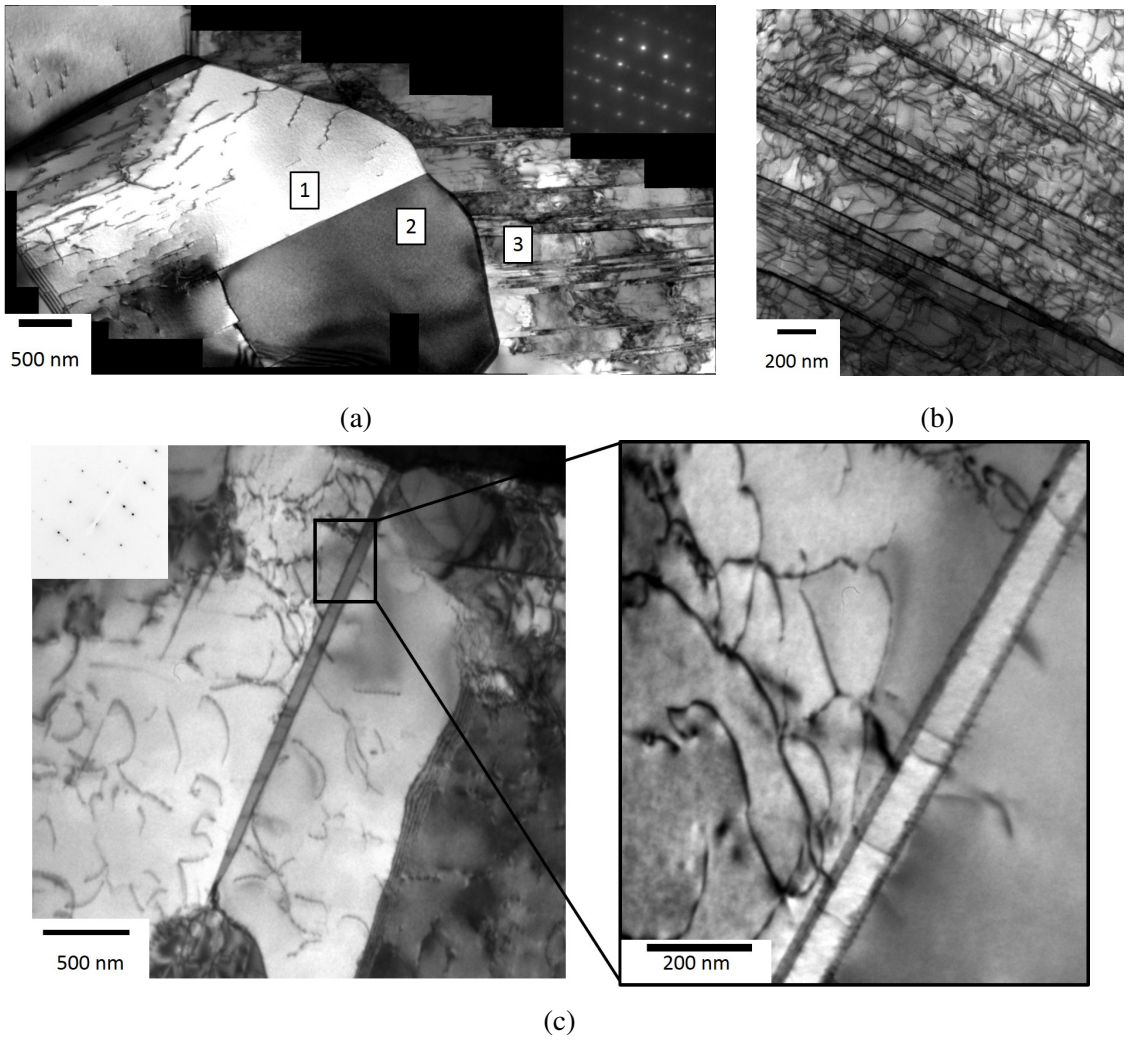

Fig. 6.2 (a) TEM-BF image of a recrystallised (marked with 1 and 2) and deformed (3) grain in a sample compressed with a strain rate of $1s^{-1}$ to a strain of 1.2 at 975°C. (b) STEM-BF image and diffraction pattern of area 3 in (a). (c) Deformation twin in a sample deformed at 1025°C with $0.01s^{-1}$

perature and across a range of strains and strain rates. An in-depth quantification of the deformation mechanisms and the influence of the testing parameters was attempted. Electron channeling contrast imaging (ECCI) on bulk material remained difficult due to the high dislocation density in the grains of interest. TEM foils were therefore the only source of information but limited the analysable area. However, all samples observed at each test condition included at least one grain showing deformation twinning. Deformation twinning in 718Plus during high-temperature compression testing can be accounted as a significant mechanism. An effect of strain and strain rate could not be determined because the limited area observed does not constitute a statistically valid sample.

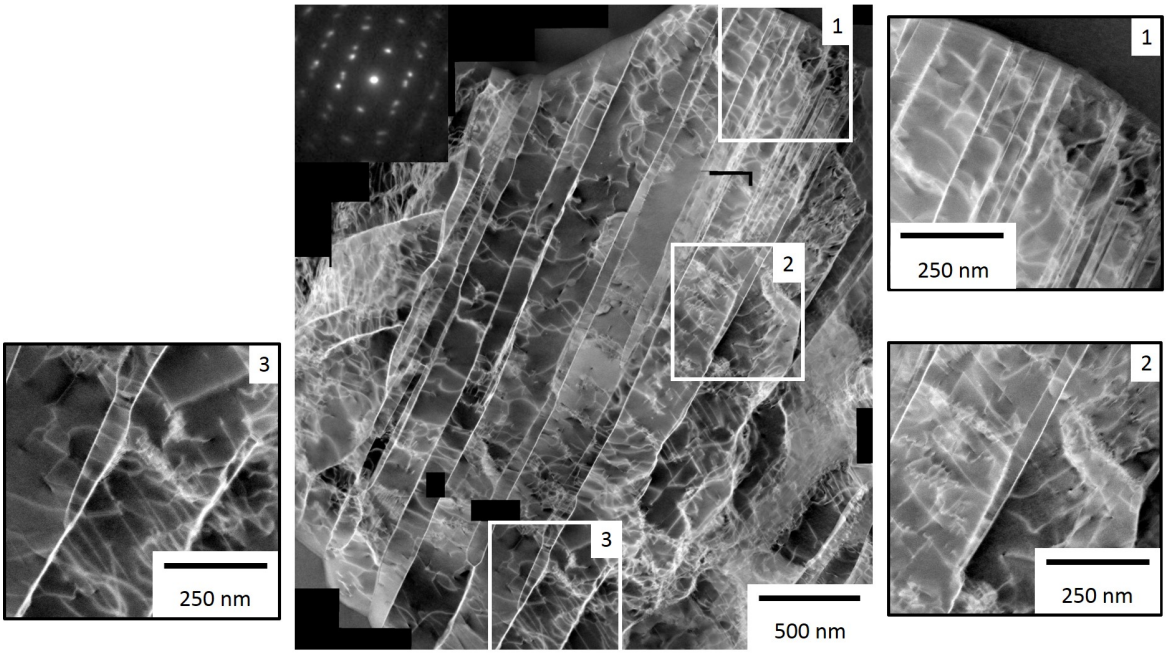

Fig. 6.3 STEM-HAADF image of a grain containing deformation twins, low angle grain boundaries and dislocation interactions.

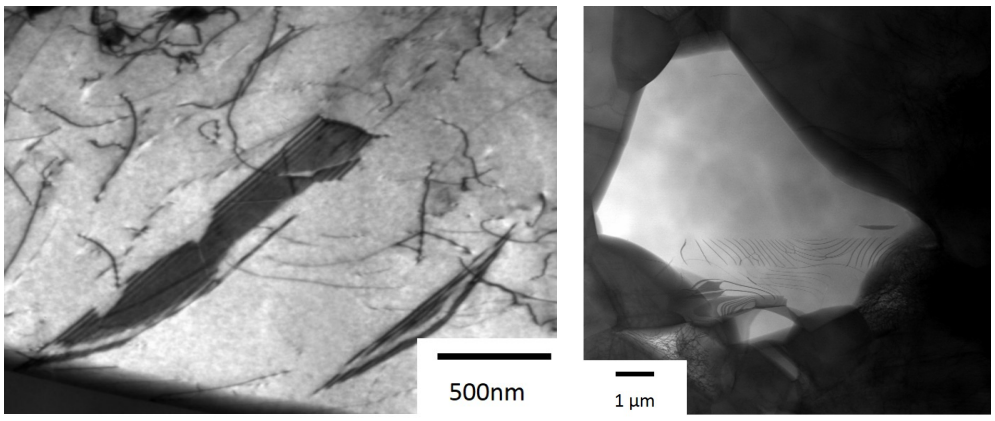

(a) (b)

Fig. 6.4 (a) TEM-BF image of stacking faults in a recrystallised grain; (b) STEM-BF image of a dislocation pile-up

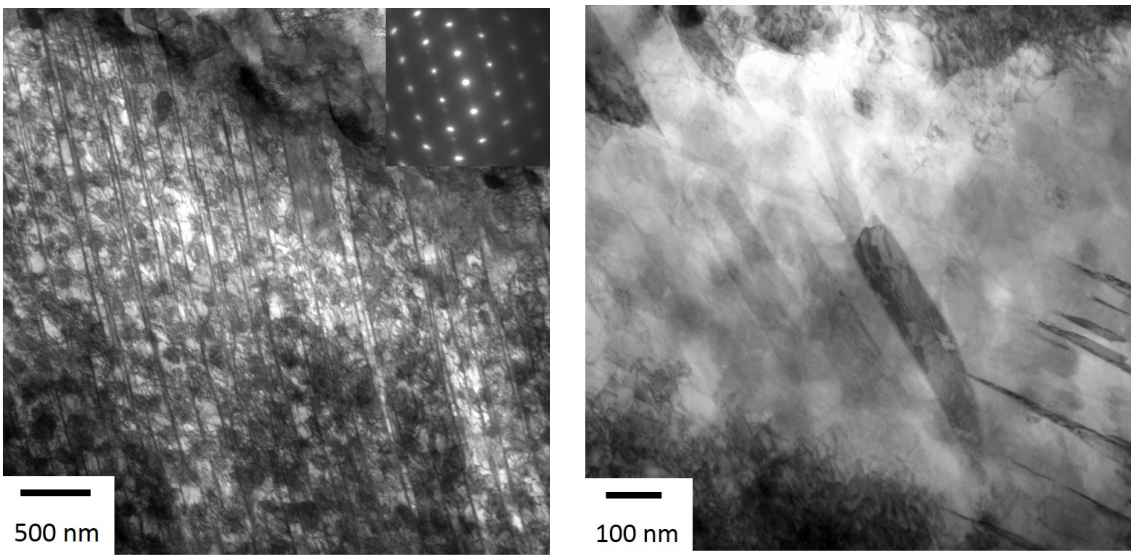

(a) (b)

Fig. 6.5 Samples deformed at 850°C with a strain rate of $1.0s^{-1}$ to a strain of 1.0. (a) Twinned grain with a γ-γ' microstructure; (b) Planar and close-to edge-on twins on two different slip systems

The samples deformed at the lowest temperature of 850°C showed a notably higher density of deformation twins. As pictured in Figure 6.5a, the grains in the γ-γ' microstructure have a high dislocation density as well as twins. In contrast to the specimens compressed at higher temperatures, the samples from the 850°C tests contain grains with twins on multiple slip systems illustrated in Figure 6.5b. The planar twins in the centre of the image grew on a different slip system to that of the narrow twins observable on the right side. The dark patches on top and bottom of the micrograph stem from dense dislocation forests spreading throughout the grain.

Twin nucleation

Figure 6.6 shows a series of dislocations in bright-field (BF) and weak beam dark-field (WBDF) conditions for different g-vectors. From the diffraction contrasts in Figure 6.6a-b it can be seen that these defects are partial dislocations leaving behind stacking faults. For a ccp crystal structure with the stacking sequence ABCABC a single partial would change this to ABC*BCA* creating an intrinsic stacking fault (see Figure 6.7). The change in stacking is seen by the shift in contrast from white to black in the BF-image and from gray to dark-gray in the WBDF condition. If a second partial with the same Burger's vector glides on the {111} above the stacking changes to ABCB*AB* and the contrast BF mode becomes slightly darker and shifts in the WBDF image from dark-gray to white. The third partial on the adjacent plane

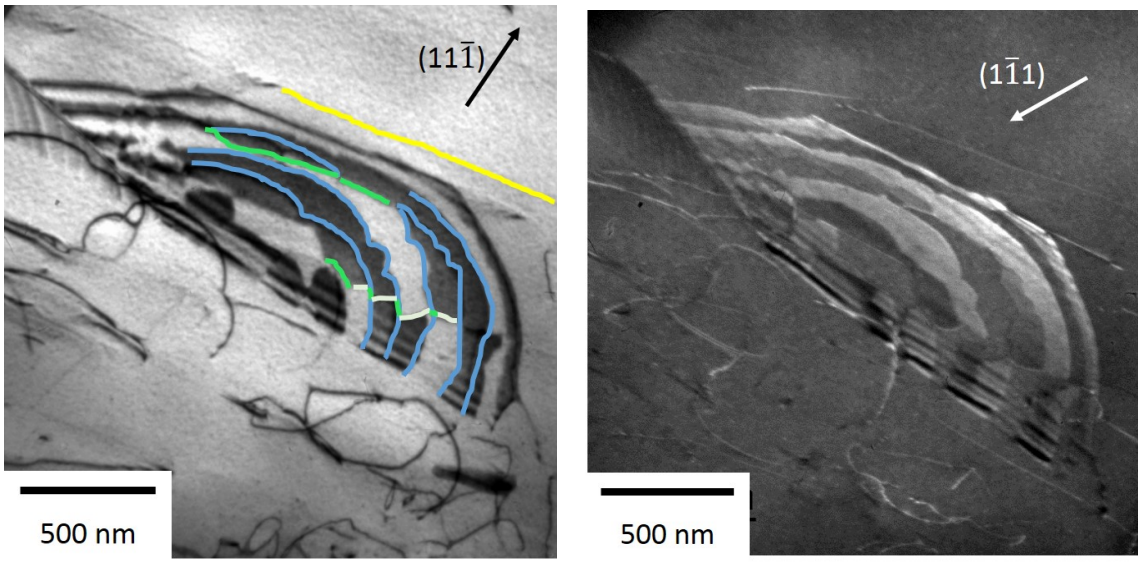

(a) (b)

Fig. 6.6 TEM images of partial dislocations. (a) BF on the g-vector of (11$\bar{1}$) (b) WBDF on the g-vector of (1$\bar{1}$1)

forms the stacking sequence ABCBA*C* and restores the white contrast in BF and light-gray in WBDF.

The feature described was imaged in six distinct conditions to derive the Burgers vector of the partials (Figure 6.8). Three different partial types could be identified marked in blue, green and white in Figure 6.6a. Deformation twins form to compensate the elastic strain field within the grain. As a consequence, the partials within the twin must be the same to generate an opposing strain field. This is the case in the given example for the blue partials. The active slip plane was determined to be (1$\bar{1}\bar{1}$). The respective partials were of following type: blue: a/6 [211], white: a/6 [1$\bar{1}$2] and green: a/6 [12$\bar{1}$]. The dislocation highlighted yellow was a matrix dislocation a/2 [101].

The fringes bordering the stacking faults mark the surface of the sample at which the dislocations are cut off. On the left side of the image a wedge-like row of dislocations intersects with the partials.

A similar arrangement of stacking faults was found in an other grain, see Figure 6.9. The upper part of the bright grain in Figure 6.9a has a slightly darker area which includes straight as well as more bent dislocations. This area finishes at an almost horizontal border at which the contrast changes to white and dislocations forming fan-shaped overlapping stacking faults. A Burgers vector analysis was performed on this grain with the identified dislocations in Figure 6.9b. The dislocations were defined for the plane ($\bar{1}$1$\bar{1}$) and estimated to be: blue: a/6 [$\bar{1}$12] , green: a/6 [21$\bar{1}$] and yellow: a/2 [10$\bar{1}$]. The yellow full dislocations

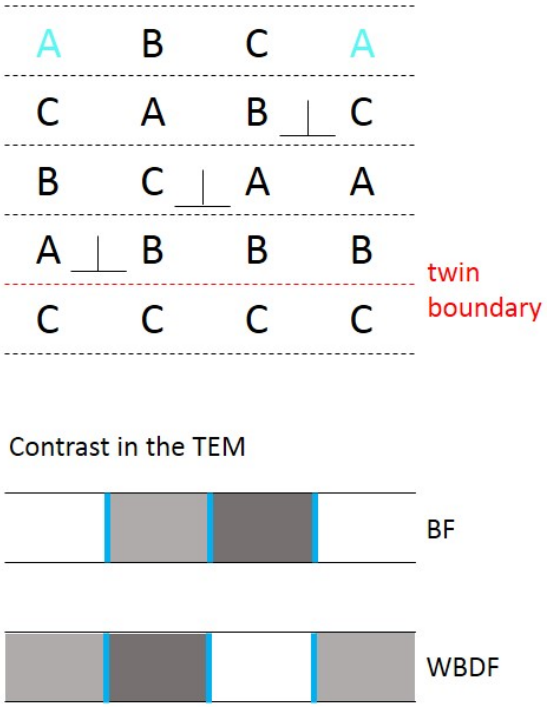

Fig. 6.7 Change in contrast with the movement of partial dislocations in an ccp-stacking

on the top are arranged in a twisted low angle grain boundary. The straight nature of the dark purple dislocations appear to be similar to sessile Frank partials defined by Idrissi et al. [188]. However, they do not seem to disturb the pattern of matrix dislocations. The light purple dislocation marks a border to the fan of partials at the bottom. Interestingly, the dislocation activity from the part on the top towards the border does not alter. The straight light purple dislocation intersects another sessile dislocation at a grain boundary creating a triple point. It is this triple point from which the twin-forming partials seem to emerge.

Figure 6.10a presents the formation of a stacking fault with both partials, the leading and the trailing, visible. The micrograph consists of a coloured representation of the identified dislocations. A Burgers vector analysis of the dislocations revealed the following types for the plane $(\bar{1}1\bar{1})$: turquoise: a/2 $[10\bar{1}]$ (111), brown: a/6 $[1\bar{1}\bar{2}]$, beige: a/6 $[21\bar{1}]$ and yellow: a/2 $[1\bar{1}0](\bar{1}11)$. The dislocations form stacking faults as they move into the center of the grain, away from the twin boundaries. In this case, the trailing partial can follow the leading partial and hence does not form a twin. The stacking faults do not overlap because their contrast does not change.

The grain also has two annealing twin boundaries marked with TB1 along the upper part and TB2 at the bottom. To explain the dislocation configuration, a 3D visualisation with MATLAB was developed by F. León-Cázares from TEM-images of six different orientations.

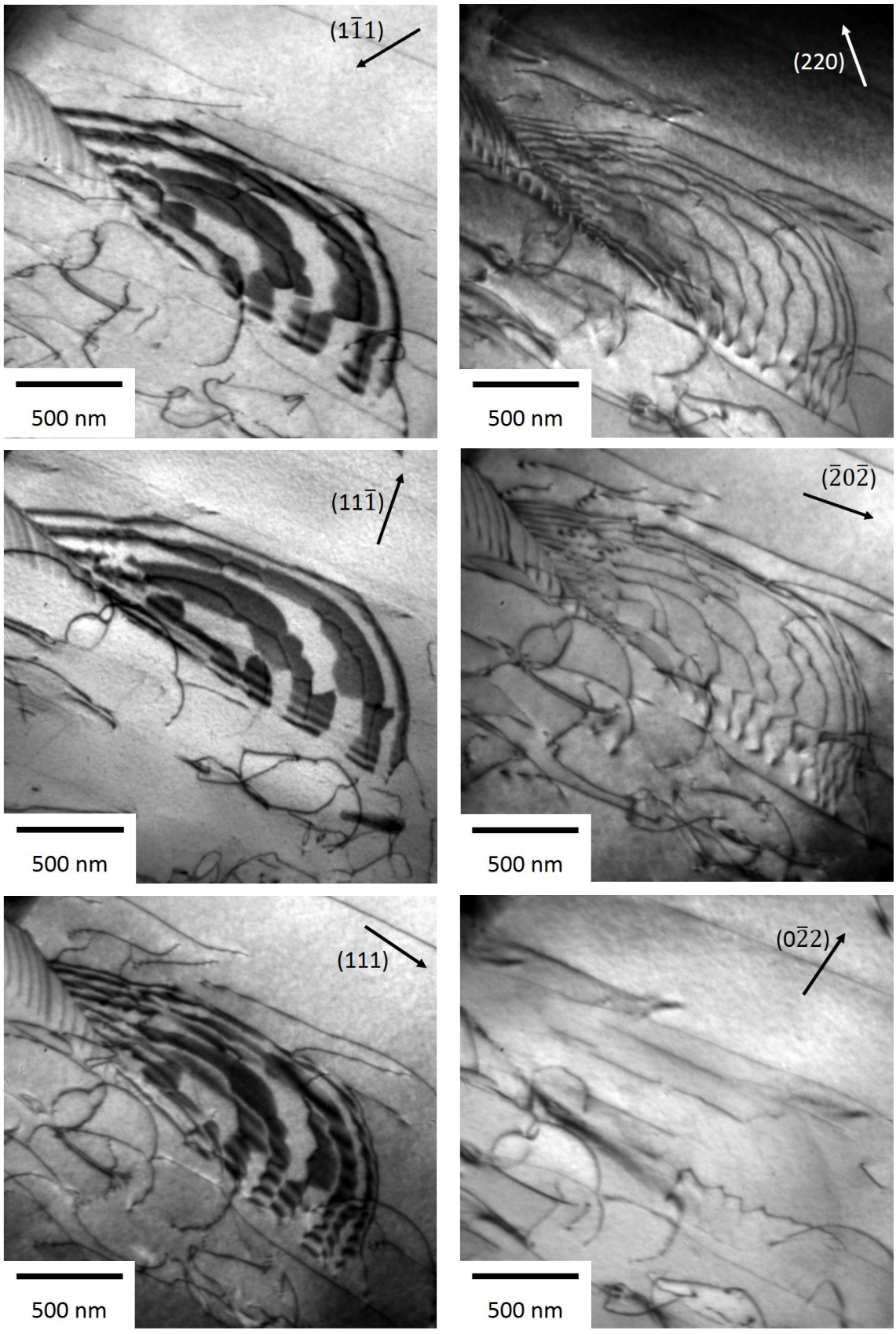

Fig. 6.8 BF images for Burgers vector analysis

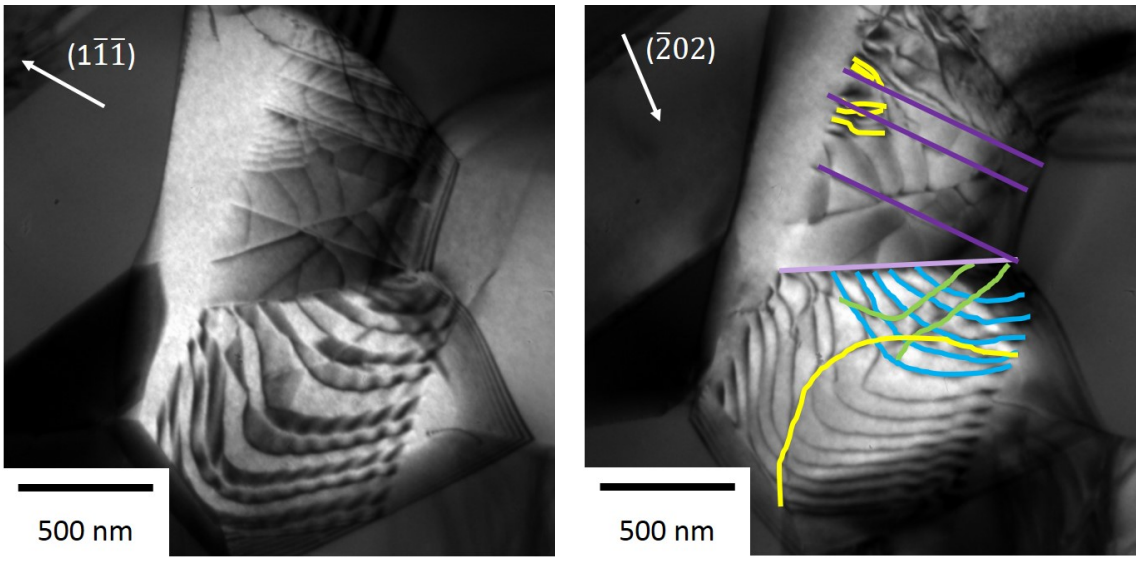

(a) (b)

Fig. 6.9 Burger vector study on a sample deformed at 975°C, ε=1.2 and $\dot{\varepsilon}$=1s^{-1}. BF on the g-vector of (a) (1$\bar{1}\bar{1}$) and (b) ($\bar{2}$02) and highlighted dislocations with different Burgers vectors.

The TEM-images for the Burgers vector analysis and the visualisation tool are given in Figure 6.11. In the 3D visualisation the dislocations are coloured according to the slip plane they are operating on. In this case, three different slip systems are active marked in red, blue and green.

The origin of the dislocations active on the blue plane (close to the specimen plane) is a Frank Read source (FR) close to the twin boundary TB1 but separate from it. The segment bowing out on the blue plane is connected to two segments on the red plane pointing up and down through the thickness of the specimen. The dislocations thus generated appear to punch through this twin boundary, into the annealing twin, TB1, at the top of the figure. There are four separate arrays of red dislocations generated on parallel planes: these too seem likely to be generated from Frank Read sources not captured in the specimen section. However, the cross-slip of the blue dislocation between the blue and red slip planes, creates short sections both suitable to act as dislocation sources.

From the 3D visualisation it can be observed, that the splitting of the dislocation into partials only occurs on the red plane. It seems that the resolved shear stress on that specific plane favours the separation of partials.

Three different examples have been shown in which partial dislocations generate stacking faults, two of which form overlapping stacking faults which are a precursor for deformation twinning. The grains where these twin events are observed are all small, with pile-up lengths

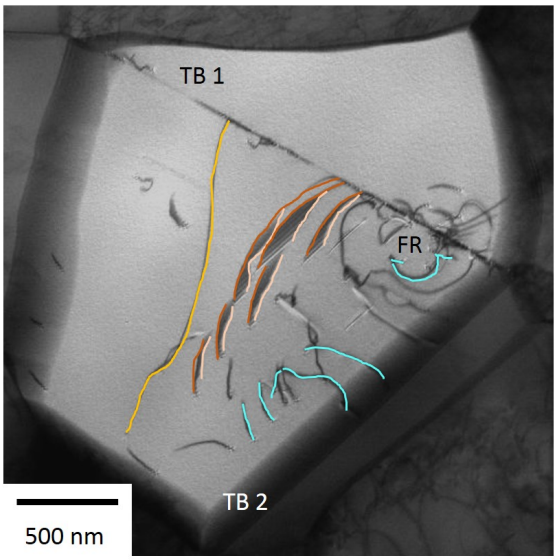

(a)

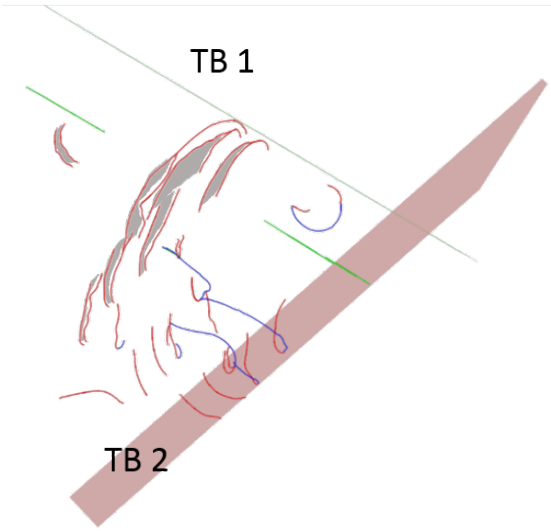

(b)

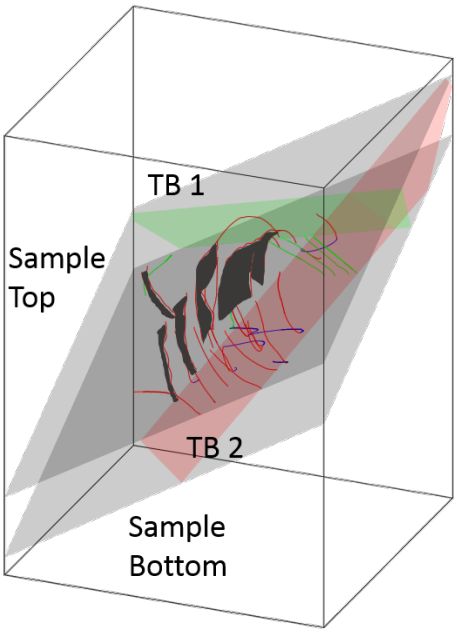

(c)

Fig. 6.10 (a) STEM image of stacking faults and dislocation activity on multiple slip systems (b) and (c) 3D visualisation of (a)

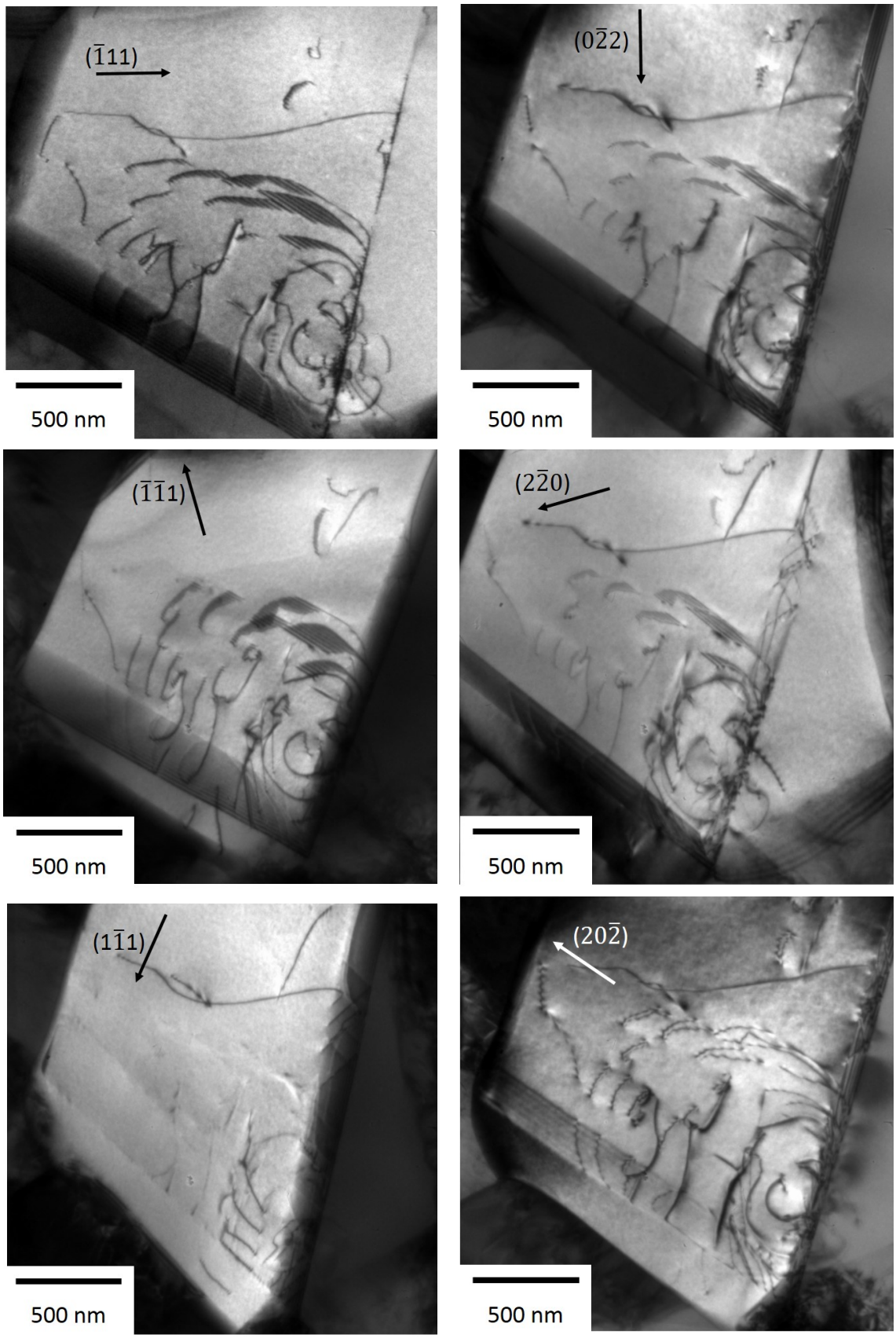

Fig. 6.11 BF images for Burgers vector analysis

well below 5 µm. Whilst it is not possible to say from these TEM observation what the overall size of the grain was, it is possible to initiate twinning in confined grains where long-range pile-ups and associated high stresses are not needed to generate the twin. Indeed, the geometry of the local shear stress and the effect on the partials seems to be the more important issue which was illustrated in Figure 6.10.

Grain orientation

The relationship between grain orientation and propensity to twinning has been analysed in numerous studies. During tensile testing, the highest twin density was found for grains with their ⟨111⟩ parallel to the tensile axis showing the lowest Schmid factor for dislocation motion [189]. Deformation twins in compression testing on the other hand favoured grains with the ⟨001⟩ parallel to the compression axis [190].

To analyse the orientations of twinned grains, a TEM foil was extracted from the mid-section perpendicular to the loading axis. With this procedure, the forging axis was well defined being out-of-plane. Figure 6.12 presents the IPF maps for a twinned grain obtained via transmission Kikuchi diffraction (TKD). The IPF map in Z-direction reveals that the grain normal is oriented parallel to the ⟨001⟩. This observation is in-line with previously stated relationships between grain orientation and twinning [190].

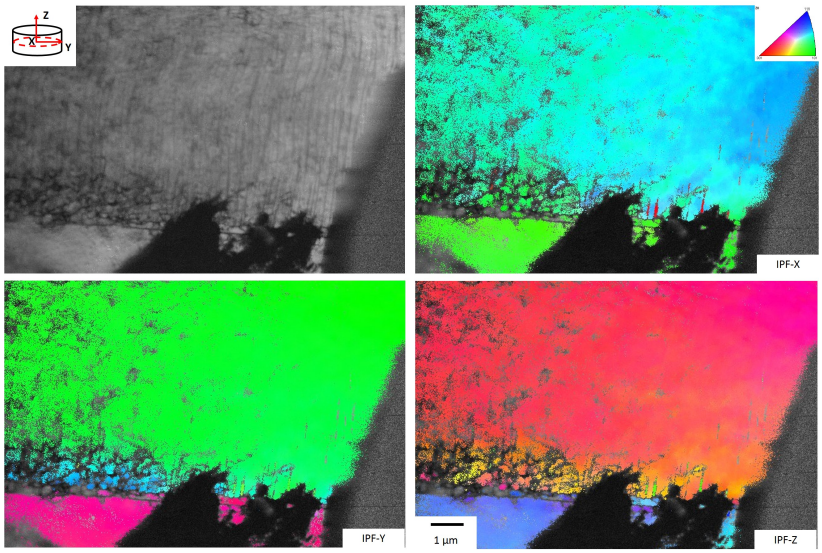

Fig. 6.12 IPF maps of a TKD scan on a grain with a high deformation twin density from a samples compressed at 850°C, $1s^{-1}$ and 1.2 strain.

6.1.3 Discussion

The present study reveals the deformation mechanisms active in the nickel-base superalloy 718Plus during high temperature compression tests equivalent to conditions typical of forging practice. Formation of stacking faults and deformation twinning make a significant contribution to strain in all samples, together with dislocation pile-ups. Within the grains of very high dislocation density, packs of 'mature' twins were present, some spanning the whole grain. During the tests, dynamic recrystallisation was activated leading to a partially recrystallised microstructure. This resulted in a heterogeneous microstructure where heavily deformed grains could be analysed alongside newly recrystallised ones. The initial stages of twin formation were captured in recrystallised grains. In the following discussion, the occurrence of deformation twins based on testing and material parameters will be discussed together with the mechanism for the twin formation.

Parameters for the formation of deformation twins

The experimental parameters for the compression tests covered a wide range of temperatures, strain rates and strains. Within the constraints of the current study, there was no effect of temperature on the propensity for twinning between 950 and 1025°C detectable. However, lowering the test temperature to 850°C, being γ' sub-solvus, showed a distinct increase in the degree of twinning within grains and also resulted in twinning on multiple planes. The influence of temperature is three-fold nature.

- Firstly, the movement of edge dislocations by climb is vital to recovery processes and is controlled by diffusion. For conventional single phase ccp alloys, raising the temperature increases the diffusion rate. This makes recovery easier and lowers the need for alternative deformation mechanisms such as twinning [173]. TiAl, however shows the opposite trend with an increase in deformation twinning with temperature. This was reasoned to be related to the lamellar nature of the alloy where co-ordinated twinning can reduce the constraint generated at neighboring colonies [180].

- Secondly, the testing temperature determines whether the microstructure is single- (γ) or two-phase (γ-γ'). In nickel-base superalloys the γ' precipitates hinder the dislocation movement by glide [2]. In γ-γ' superalloys twinning requires activation to pass through ordered precipitates, and hence tends to be a high-temperature phenomena during creep in several nickel-base alloys [191, 192]. Stacking fault energy penalties generated during twinning can be lower than anti-phase boundary (APB) energies in γ' but require thermally activated re-ordering to occur [192]. Although mostly deformed in the supersolvus condition, 718Plus remains close to the solvus and may experience short range order effects.

- The temperature dependence of the SFE of superalloys is still under debate. Recent theoretical studies claim a decrease of the SFE of nickel with temperature, contradicting the common assumptions based on CALPHAD calculations of the relative enthalpies of the ccp and hcp phases [193–195]. It was also shown by Shang et al., that the γ' forming elements aluminium and titanium further decrease the SFE of nickel [194]. Thus above the γ' solvus the effect of temperature on twinning is complex. On the one hand one would anticipate an intrinsic increase of the SFE with temperature, and on the other the enrichment of the matrix with aluminium and titanium on dissolution of the γ' leads to a lowering of SFE.

In terms of the role of temperature on twinning in 718Plus, the mechanism appears to be less affected by the appearance of ordered precipitates than by the ability of the dislocations to recover. SFE with temperature is competing with the ease of climb rising with temperature. Hence it is perhaps not surprising that the influence of temperature on the amount of twinning is minor.

High strain rates and severe plastic deformation are frequently reported to trigger deformation twinning in nickel-base superalloys [178, 59]. Twins have been found after high temperature compression tests for strain rates of 10 and $20s^{-1}$. At high strain rates the dislocations have less time to reduce the overall energy by thermally activated recovery processes. Hence, twinning provides an alternative mechanism which is less inhibited by dislocation density, and indeed may be facilitated by moderate amounts of slip. In the present study twinning was observed at strain rates as low as $0.01s^{-1}$, but was more common at the higher strain rates, albeit relying on observations from a limited number of grains. In TWIP Steels [170], the argument is made that a certain level of strain needs to be achieved to reach the critical resolved shear stress on the twinning plane. This involves dislocation activity leading to work-hardening. It implies that twinning requires more stress than initial dislocation motion. Hence, in TWIP steels twinning is preferred in larger grains ($>3\,\mu m$ [170]) and high strain rates where sufficient work-hardening can be achieved. The observations here do not suggest that twinning requires significantly more stress than dislocation motion, although it is clear that the twinning mechanisms proposed in a later section require dislocation activity in order to operate [196]. Twinning in this study is seen to be operating in newly recrystallised grains with, overall, a very low level of dislocation density. The three strain levels in this study, 0.4, 0.8 and 1.2, had no influence on the amount and appearance of, the twins. Closely packed deformation twins were only observed in grains present before the compression test: within recrystallised grains deformation twins were always in the early stages of formation.

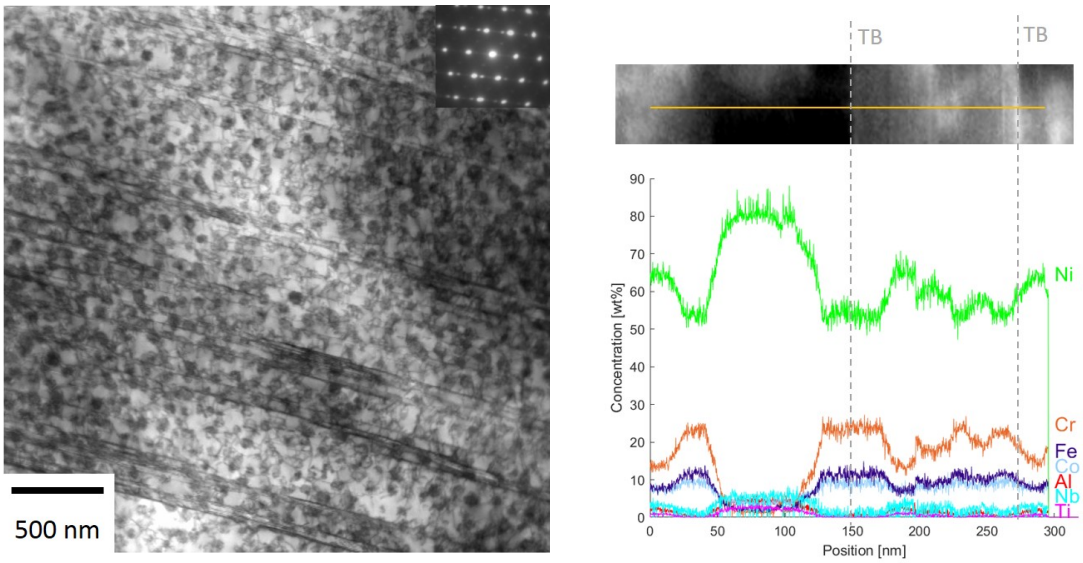

(a) (b)

Fig. 6.13 Sample deformed at 850°C with a strain rate of 0.01 µm to a strain of 1.0. (a) Heavily twinned γ-γ' microstructure (b) EDX-linescan across several twin boundaries (TB).

Chemical effects: segregation and phase formation

In an ccp lattice, twins locally form an hcp structure. Alloy 718Plus precipitates η phase, an hcp-phase with the crystal structure $D0_{24}$. The nose of the TTT-diagram of η was experimentally determined to be at around 950°C [16]. As the compression tests were performed in this temperature range it is possible that η starts precipitating in the metastable γ matrix preferring a site that is already hexagonal. An alternative, but equivalent, view would be that appropriate elements partitioning to the η phase, (niobium and titanium) would segregate to such a fault effectively lowering the SFE. To evaluate whether this could be a contributory factor in twinning, EDX measurements on twin boundaries were performed on samples deformed at 850°C. Figure 6.13b presents the results of a linescan across twin boundaries on edge in a sample deformed at 850°C with a strain rate of $0.01s^{-1}$ (Figure 6.13b). The dark area on the left side of the first twin boundary is a γ' particle in diffraction, seen by the increase of titanium, aluminium and niobium and the decrease in chromium, cobalt and iron. Another precipitate is detected at the position 180-200 nm, close to the end of the scan. The scan shows several peaks at and in between the twin boundaries, but they tend to be consistent for all elements. Therefore, the rise in count number of the elements is due to preferential etching of specific lattice planes during the electropolishing of the TEM discs, and provides no evidence for segregation to the twin interface. Previous observations of segregation of cobalt and chromium at stacking faults and microtwins were observed within

γ' precipitates by high resolution TEM [197]. Similarly, the formation of η phase during creep was detected in γ' particles but not the γ matrix [198].

Formation of deformation twins

A number of recrystallised grains were found which showed the initial stages of the formation of a deformation twin. These grains were formed in a 'necklace' structure by dynamic recrystallisation and were much smaller than the deformed grains, many less than 3μm in diameter as sectioned. The dislocation density varies depending on when these grains formed during the continuous compression of the samples. Twin-forming partials were observed in recrystallised grains containing other dislocations, not part of the twinning process, and were all found close to a grain boundary.

Figure 6.14a is a good example where a fan of overlapping partials is emitted from a low angle grain boundary where the individual dislocations characterised in Figure 6.8 are visible. The low angle grain boundary (LAGB) forms a small wedge which does not pass through the full thickness of the foil, instead there is a sharp fold within the foil where the dislocations in the LAGB cross-slip onto the twinning plane and the leading partials bow out to form the twin on the (111) plane. There is almost a one-to-one correspondence between the dislocations in the LAGB and the twinning dislocations, and the Burgers vectors are compatible. It is notable that the dislocations only show the propensity to dissociate on the one plane not the plane of the LAGB. This could be due to the forces acting on the individual partials to constrict or expand the stacking fault, these forces would depend on the dissociation plane [186]. As with all the other early twinning events observed, it is close to a grain boundary.

A further example where a more irregular LAGB can serve as a twin nucleation site is shown in Figure 6.14b. This shows an edge-on deformation twin (marked with DT) emerging from the LAGB at the lower right side of the image. Grain boundaries can serve as nucleation sites for partial dislocations, especially important for nanocrystalline materials which are too small to provide a suitable length for a dislocation pile-up [199, 79]. In the cases presented low angle grain boundaries emit twinning partials leaving trailing partials as part of the boundary, necessary to accommodate the misorientation of the emerging micro-twin.

Figure 6.14c presents overlapping twinning dislocations in the plane of the foil. The alternating contrast of the twinning partials are marked by the red arrow. White arrows indicate accentuate straight dislocations on two different planes. The straight lines could be sessile dislocations. In a similar pattern these dislocations were determined to be Frank partials by Idrissi et al. [188]. Unfortunately, it was not possible to fully characterise them in the present image.

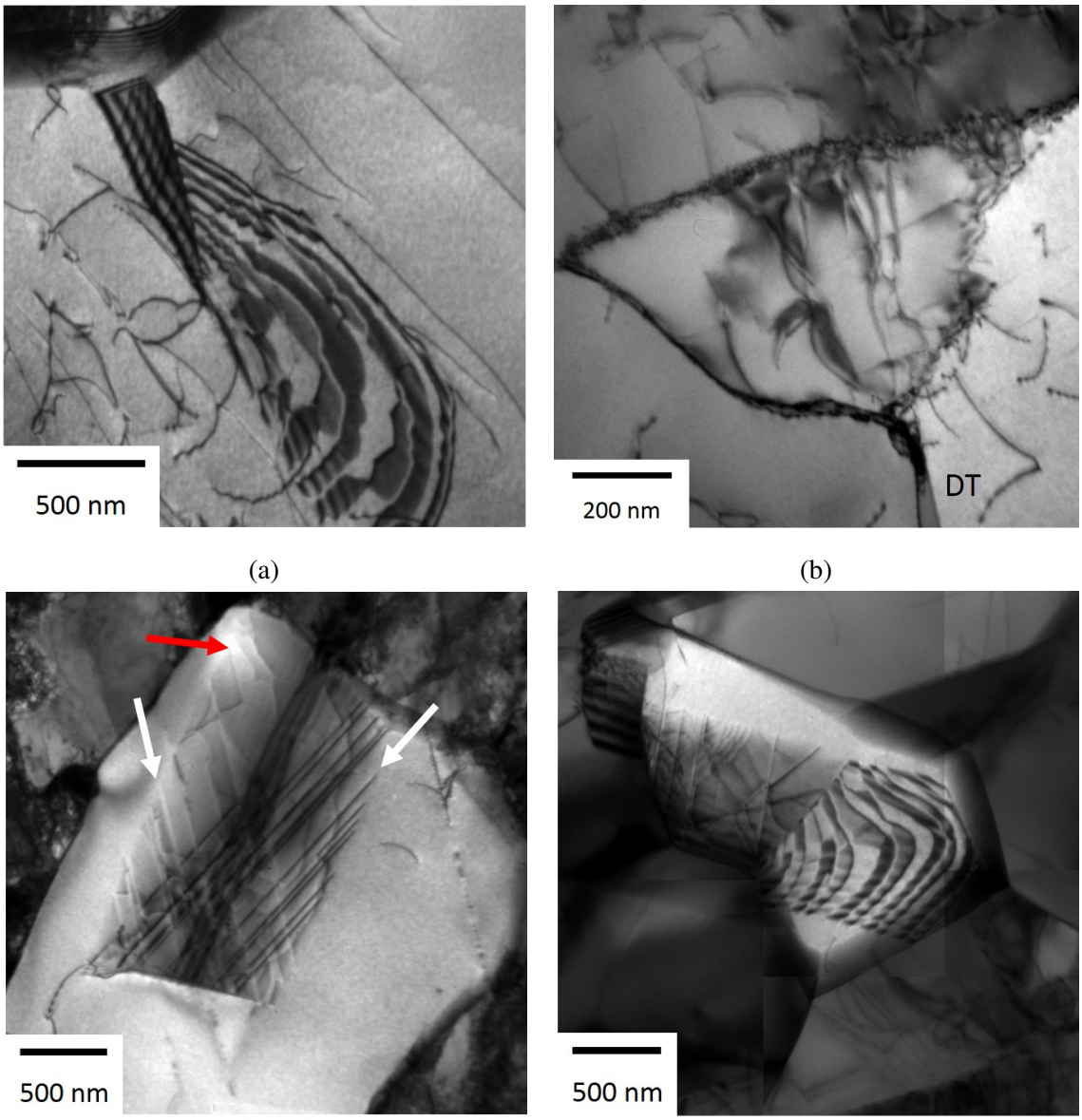

(a) (b)

(c) (d)

Fig. 6.14 Nucleation sites for deformation twins in samples with the following testing parameters: (a) and (d) T=975°C, ε=1.2, $\dot{\varepsilon}$=1s^{-1} (b) T=1025°C, ε=1.2, $\dot{\varepsilon}$=0.01s^{-1}(c) T=950°C, ε=1.2, $\dot{\varepsilon}$=1s^{-1}

Figure 6.14d shows features discussed in a and c. The grey area on the left side of the white grain includes a number of faint and straight dislocations. This area is bordered with another straight line which is slightly tilted to the right. From this feature, fan-shaped stacking faults are emerging. Again, a low angle grain boundary is present in the vicinity of the twinning partials. However, the dislocations building the LAGB had no interaction with the partials of the stacking faults.

A wide range of nucleation mechanisms for deformation twins have been developed which require cross-slip events, pile-ups or dislocation reactions on co-planar planes [79]. The pole mechanism by Venables [200] considers the formation of jogs as initiating configuration for twinning. A long enough jog of a dislocation splits into a sessile Frank partial of type a/3$\langle 111 \rangle$ and a glissile Shockley partial a/6$\langle 112 \rangle$. The Shockley partial can glide and bow around the jog leaving a stacking fault. The rotation around the poles creates stacking faults on adjacent planes with partials of the same Burgers vector forming the twin. Although this theory offers a solution for the formation of the necessary partials on adjacent planes, sufficiently large and mobile jogs are a prerequisite. Venables' pole mechanism still lacks experimental evidence [170]. Nucleation models based on twin formation on the primary slip plane rely on the formation of the correct partials on neighbouring planes. Mahajan and Chin [171] presented a mechanism where co-planar dislocations dissociate into Shockley partials which is repeated on consecutive planes. It remains unclear though, what pins the trailing partial and how likely it is to form the ideal partial configuration on adjacent planes for twin formation. Another model proposing twin formation on the same plane as dislocation slip happens is from S. Miura, J. Takamura and N. Narita [201]. A key feature is the presence of a Lomer-Cottrell lock [202]. A Lomer-Cottrell lock is formed when two leading partials on conjugate planes encounter each other on an intersection of the slip planes forming a sessile Frank partial. In the Miura-Takamura-Narita model dislocations pile up ahead of the lock. When the leading dislocation encounters the lock it reacts with the sessile a/3$\langle 111 \rangle$ to form two partials which double-cross-slip on adjacent planes and leave behind a Frank partial. This model lacks an explanation for the second cross-slip event and subsequent growth cannot be explained either. The nucleation theories by J. Cohen and J. Weertman [203] and T. Mori and H. Fujita [204] consider twinning on conjugate planes. The difference is the dissociation reactions at the cross-slip events. The Cohen-Weertman model is similar to Miura-Takamura-Narita proposing interaction of a dislocation with a Lomer-Cottrell lock and the formation of a Frank partial but only producing a single twinning partial, and this on a conjugate plane. In this theory, the existence of the lock-dislocation is ignored and the locked dislocation only serves its purpose as an obstacle in the microstructure. Mori and Fujita developed a model for the cross-slip of partial dislocations. Therefore, the partial splits

at a dislocation bundle or multipole in a sessile stair-rod dislocation a/6⟨110⟩ and a Shockley partial which forms a stacking fault on the conjugate plane.

As for the present samples, the nucleation of deformation twins in recrystallised grains did not require the formation of pile-ups. Hence, theories considering only dislocation glide such as the Mahajan-Chin [171] or Miura-Takamura-Narita [201] will not be considered any further. The Cohen-Weertman [203] and the Mori-Fujita model [204] both consider cross-slip mechanisms with different dissociation reactions. Considering the fan-shaped structure in Figure 6.14a which has a low angle grain boundary to the right. The dislocations within this boundary were identified as matrix dislocations of the type a/2 ⟨101⟩. Hence, the cross-slip mechanism by Mori and Fujita is unlikely to be active. The dissociation mechanism proposed by Cohen et al. [203] would suggest leaving behind a sessile Frank partial. These a/3⟨111⟩ dislocations cannot be on top of each other on adjacent planes as the resulting Burgers vector is energetically unfavorable. The sharp interface in the grains with the fan-shaped stacking faults was lacking in any signs of trailing, sessile dislocations. A detailed analysis of Idrissi et al. [188] on mechanisms operating in TWIP steels confirmed two of these mechanisms being active in their samples. In the present analysis we are looking at twinning at much higher temperatures than these examples and this will make a difference as to what is possible or indeed likely.

A theory which could explain the observation would be the pole-mechanism proposed by Venables [200]. The original theory considers the formation of jogs as initiating configuration for twinning. A long enough jog of a dislocation splits into a sessile Frank partial of type a/3⟨111⟩ and a glissile Shockley partial a/6⟨112⟩. The Shockley partial can glide and bow around the jog leaving a stacking fault. The rotation around the poles creates stacking faults on adjacent planes with partials of the same Burgers vector forming the twin. However, it seems unlikely for a dislocation to form a jog of adequate length.

An alternative pole-type mechanism is proposed in the following. If a partial intersects with a screw dislocation it forms a half-step. When bowing around the dislocation, one part of the partial propagates at the initial plane while the other part of the partial glides on the adjacent plane. They both leave behind stacking faults on parallel planes if the trailing partial is left behind. This theory only gives an explanation for the first two layers of the twin and is misses a consecutive propagation of twinning partials.

Dislocation activity is a necessary pre-cursor to twinning but the generally low dislocation density observed where these early stage twins are forming suggests that the SFE energy is sufficiently low for partials to move creating twins at stresses similar to those for perfect dislocation movement, but where the orientation of the grain favors the separation of the partials.

Thus, we would argue that the requirement for twinning to be preceded by substantial work-hardening, put forward for TWIP steels [170], does not appear to be valid for this super-solvus superalloy. Indeed, twinning and dislocation activity appear to operate simultaneously and grains which are heavily twinned often have high dislocation densities. Twinning and dislocation movement will of course experience different Schmid factors in each grain and twinning will also experience a tensile/compressive anisotropy, leading to the observed uneven distribution of both mechanisms in individual grains.

It was intended to describe the observed stages of early twinning with a theoretical model. However, none of the theories satisfactorily fit all the observations and restrictions in the high temperature deformation of 718Plus reported here.

6.2 Deformation of the η phase

The secondary η particles in the present study formed as long and thin lamellae. The following section presents the response of η to the strain induced by the compression tests.

6.2.1 Observations of η deformation

Figure 6.15 shows the orientation of η with the progression of strain. Automatic detection of η on the BSE images was unsuccessful due to strong deformation contrasts. Hence, the precipitates were manually redrawn and scanned to further process them with ImageJ [205].

The orientation of η was plotted in a polar histogram with the 90° position parallel to the loading axis and 0/180° perpendicular. The initial microstructure in blue shows a homogeneous distribution of η throughout the polar histogram from 0 to 180°. After straining to 0.4 (yellow) the orientation of η was still random. Increasing the strain to 0.8 (orange) has changed the orientation distribution of η to a strong horizontal positioning. In green is the alignment of η at the highest strain of 1.2. Between 0.8 and 1.2 the orientation of η relative to the loading axis stayed the same with the highest fraction of the precipitates aligned perpendicular.

After the general overview of the rearrangement of η, the specific deformation characteristics of η were addressed by analyzing etched samples. Figure 6.16a presents the various ways η adjusted to the strain. All images were taken with their y-axis parallel to the forging axis. Figure 6.16b shows the breakage and globularizing of lamellar precipitates known as spheroidization. The broken pieces of the precipitate are at ~45° angle to the undeformed horizontal lamellae. Another interesting response of η to the strain was a severe bending of the particle as seen in Figure 6.16c. While a number of particles aligning in a U-shape were

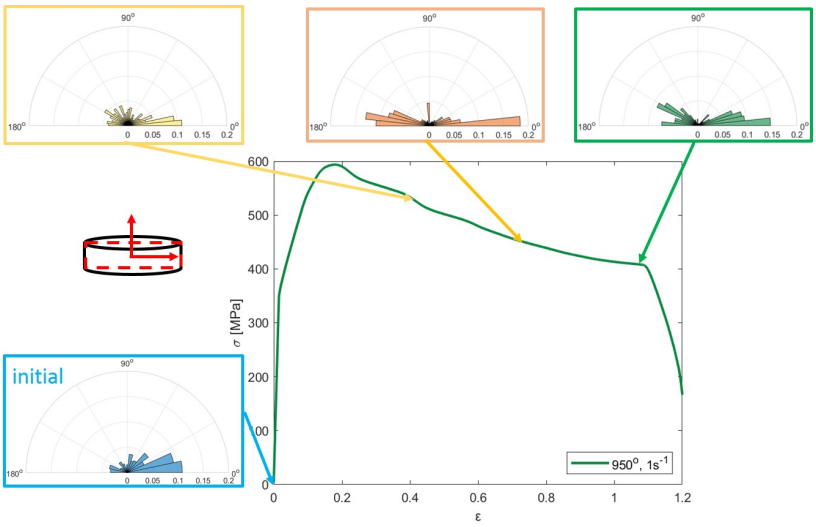

Fig. 6.15 Alignment of η particles with strain at 950°C and $1s^{-1}$ strain rate

formed by smaller parts which broke up and realigned, the left precipitate in the close-up of Figure 6.16c is found to be just a single precipitate.

The two characteristic forms of η deformation, i.e. breakage and bending, were further analysed quantitatively and qualitatively. The etched cross-sections were studied upon any site-preferred patterns of broken and heavily bent precipitates. There were no obvious areas in which a higher density of bent η could be detected. Even though this morphology can be frequently observed throughout the cross-section, the number was not high enough for a statistically valid conclusion.

A detailed investigation was done by using STEM. Figure 6.17 shows packets of thin η which are dark as they are strongly diffracting. The microstructure is partially recrystallised with a large recrystallised grain in light grey between two lines of η. A higher magnification of this area shows that η has broken up and realigned in a horseshoe configuration. This observation has already been made in the SEM micrographs.

In Figure 6.18 a set of close-ups from a highly bent η precipitate are presented. The contrast of the dislocation structure within η is weak however, the magnification show some darker, horizontal lines marked with white arrows together with areas of high dislocation density. The surrounding microstructure consists of recrystallised grains with a low dislocation density and originally present grains with a high dislocation density. The crack in the overview picture occurred during the sample handling before the images were taken. However, the dislocation structure in the γ and η phase in this area did not alter between TEM analyses before and after the crack.

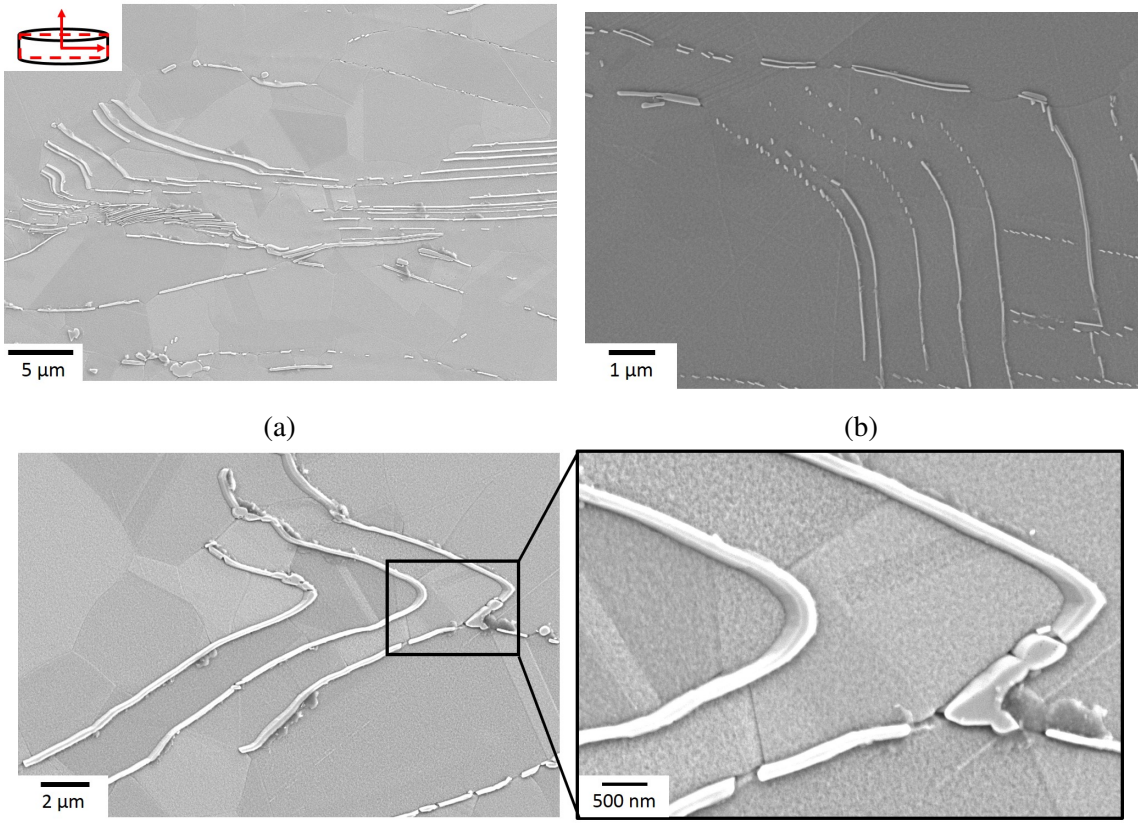

Fig. 6.16 SEI (secondary electron imaging) from γ etched specimens to reveal η. Samples were tested at 975°C, ε=1.2 and dwell time 120s^{-1} with a strain rate of 1s^{-1} (a and c) and 0.01s^{-1} (b)

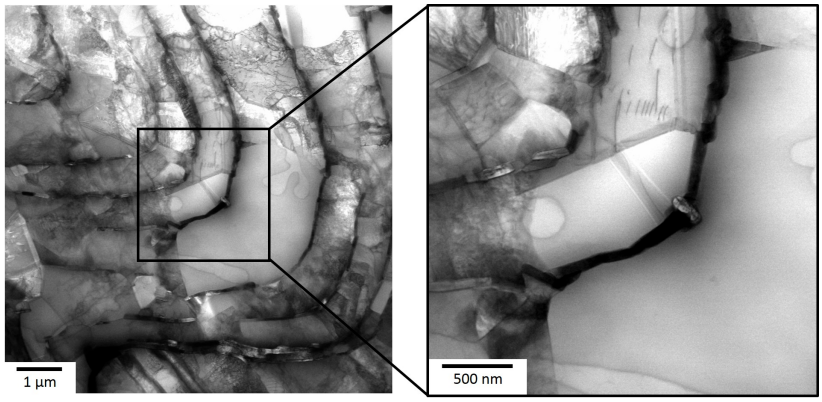

Fig. 6.17 Breakage and alignment of η in a partially recrystallised microstructure

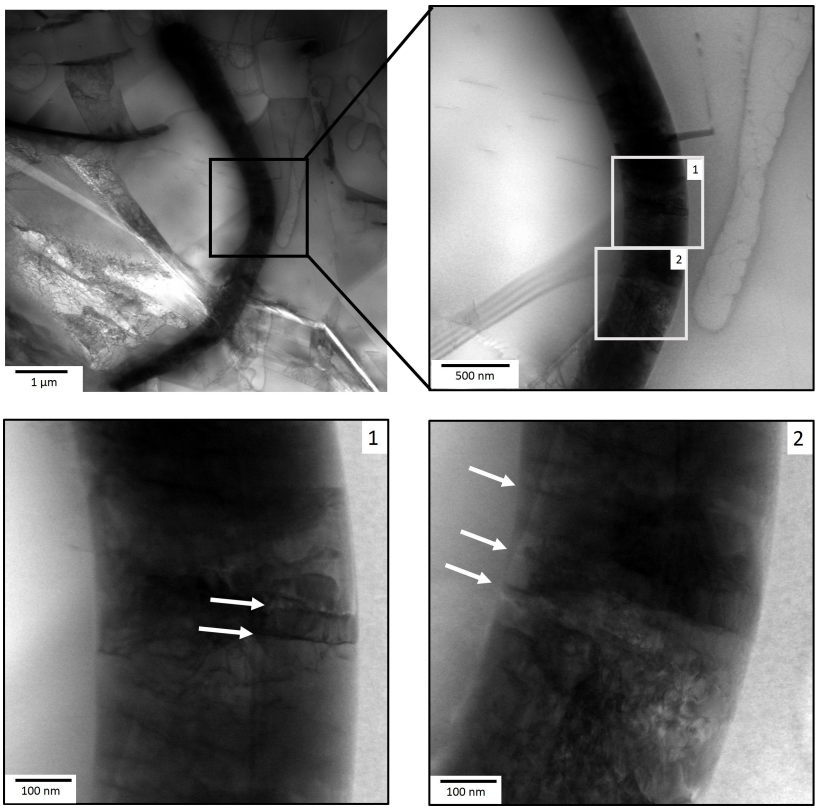

Fig. 6.18 Severe bending of η

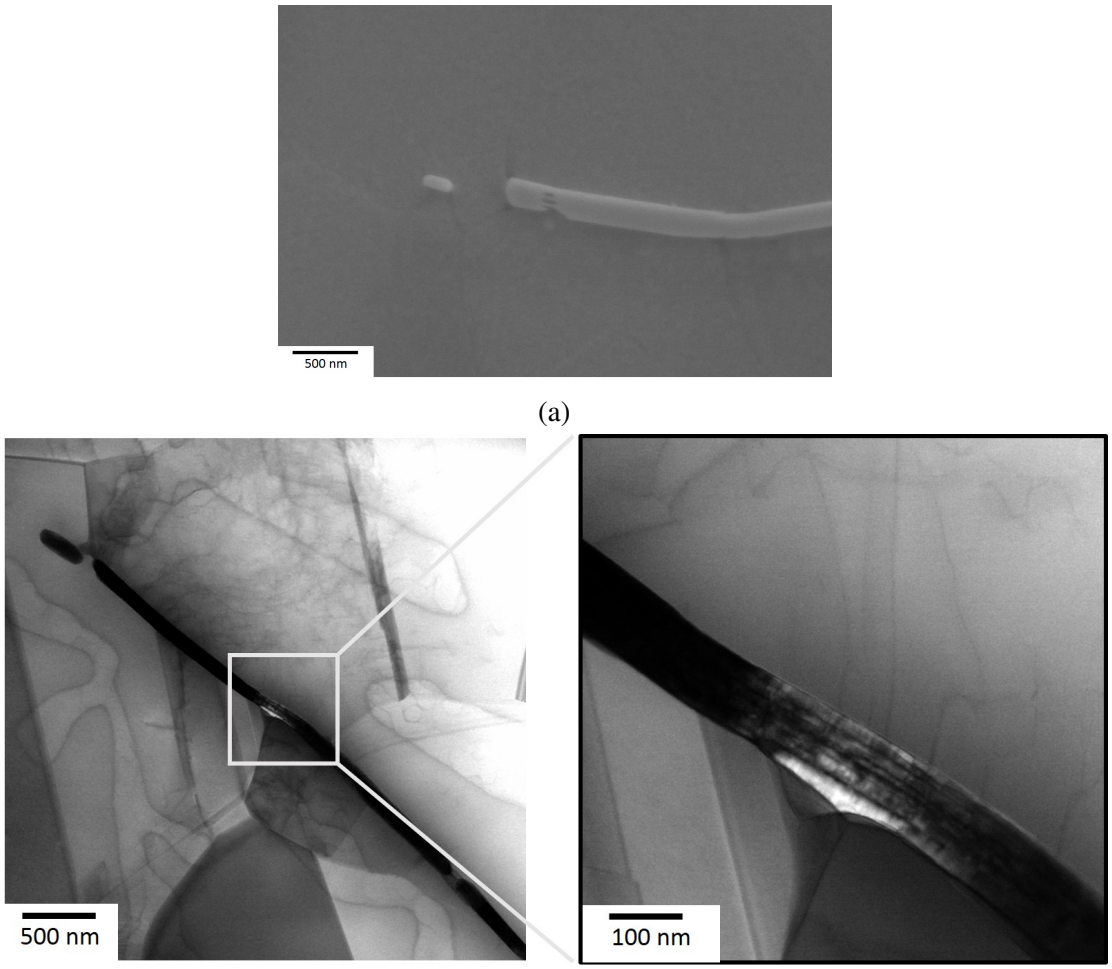

(a)

(b)

Fig. 6.19 η morphology before breakage

6.2.2 Discussion

The η phase was found to deform by either breaking up and realigning to the flow or by severe bending of the precipitate. The two deformation mechanisms were distributed homogeneously throughout the cross-section of the sample.

It was shown, that the precipitates gradually align themselves perpendicular to the compression axis with strain. A strong alignment could be achieved by the breakage of the particles and subsequent spheroidisation. The breakage and globularisation of the second-phase δ in IN718 has been attributed to a spheroidisation process [206]. Spheroidisation has been described in other systems including titanium alloys as a deformation mechanism of the hcp α phase in the bcc β matrix and pearlite in steels during annealing [207, 208]. The formation of a subboundary within the precipitate promotes diffusion of matrix elements

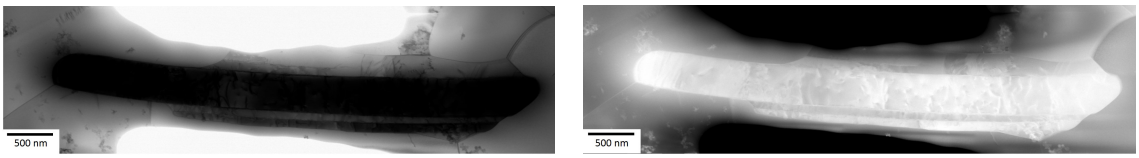

Fig. 6.20 η precipitate in recrystallised matrix.

to and into the particle. The matrix grows along the subboundary into the precipitate. The particle is chamfered and eventually pinched-off. The development of subgrains within an α particle has been observed after deformation in Ti-6Al-2Sn-4Zr-6Mo [209]. In addition to the surface tension caused by subboundaries, dislocations moving to the particle-matrix interface can serve as stress concentrators leading to break the precipitate [206]. The smaller particles can then more easily align to the material flow.

Figure 6.19a shows an SE-image of a small η precipitate ahead of a longer one. The small η could be the result of a spheroidisation event. At the front of the longer particle two oblong holes and a large groove are visible. A STEM micrograph of an η precipitate is presented in Figure 6.19b similar to that in (a). The dark η phase is bordered with recrystallised grains at the bottom and a deformed grain at the top. Ahead of the long η is again a smaller precipitate at the top left. In the middle of the image a close-up was taken which centres around a bright area of η. At this region the insides of the particle are revealed. The microstructure of η consists of a number of longitudinal, darker elements at which dislocations in form of grey lines are accumulated. The thick black lines can be layers of δ inside η acting as an obstacle for the dislocation movement [13]. The bridges in the particle in Figure 6.19a could be undissolved δ.

The formation of substructures in lamellar η was found to be of a longish shape while thicker η which experienced severe bending formed transverse structures (see Figure 6.18). It is unlikely that these structures are part of a recrystallisation process. Recrystallisation of the ordered η is difficult because during recrystallisation the ordering needs to be restored. The breaking up of the precipitate seems to be facilitated from internal stresses between the η-δ-γ layers. However, this assumption needs to be validated with further studies.

A study on δ in IN718 noted a higher degree in spheroidisation in the centre of the deformed samples [206]. Precipitates further away from the centre were found to be in the process of breaking up to a lesser degree into small and rounded δ. In the present study a site-specific deformation process was not found.

Besides the breakage of η, the precipitates were found to be able to bend by almost 180^{o} without signs of cracks. The dislocation arrangement inside η is presented in Figure 6.20. Besides a high dislocation density this specific particle shows a number of crosswise rows

at the top end, similar to what has been found in a bent particle (Figure 6.18). Transverse arrangement of dislocations can facilitate the curving of a phase. Another possible reason for the high deformation of η could be proposed for this behavior. Firstly, η in 718Plus is a 'composite' particle which constitutes of η, δ and γ [13]. The layers of each of these phases can slide over each other to accommodate external strains. Lastly, ongoing DRX continuously alters the orientation relationship between precipitate and matrix. For an hcp phase to activate the slip system on the basal and prismatic plane (which support a bending motion) a shear force needs to be applied in longitudinal direction. Similar to a three-point bending test of a beam, this configuration can be obtained by recrystallised grains which grow in different directions. Hence, the precipitate can bend without losing its connection to the surrounding matrix.

6.3 Summary

The deformation mechanisms of the γ-γ' matrix and η phase in 718Plus were analysed primarily by the use of TEM. Deformation twins were found within the samples regardless of the high testing temperature and low strain rates. Burgers vector analysis was carried out to characterise the participating dislocations. In addition, the initiation and growth of the twinning partials was discussed. The following conclusions can be drawn from the deformation twinning analysis:

- Deformation twinning was observed in 718Plus during high temperature compression tests at all strain rates (0.01-1s^{-1}) and strains (0.4-1.2) and in the temperature range from 850 to 1025°C being above and below the γ' solvus temperature.
- Twinning on multiple slip systems was active in samples containing a γ-γ' microstructure. This could be reasoned by the stress concentration of the γ' particles.
- Deformation twinning in 718Plus at elevated temperatures is believed to be due to a decrease in stacking fault energy with temperature.
- Twinning partials were observed to be emitted from low-angle grain boundaries. Another nucleation site observed was determined to be a Frank-Read source.
- The formation of deformation twins did not require a significant degree of work hardening

The η phase showed significant plasticity and was found to deform by either breakage and realignment or severe plastic deformation. Dislocation substructures could be detected

inside the precipitate. The high ductility of η was reasoned to 1) a transverse arrangement of dislocations inside η, 2) the composite nature of the precipitate and 3) the recrystallisation of the surrounding matrix. However, a detailed analysis of the deformation of η is required to confirm these observations.

Chapter 7

Conclusion and future work

In the present body of work the microstructural changes during hot forging of the nickel-base superalloy ATI® 718Plus™ were studied. High temperature compression tests on a γ-γ' and a γ-η microstructure were performed. Particular attention was given to the influence of the forging parameters on dynamic and meta-dynamic recrystallisation. In addition, deformation mechanisms have been highlighted in various phases. The final part of this work summarises the research findings and give an outlook on subsequent areas of interest.

7.1 Conclusion

High temperature compression tests were performed on cylindrical samples at temperatures ranging from 850-1025°C to strains between 0.4 to 1.2 and with strain rates of 0.01 to $1s^{-1}$. The test matrix for the γ-η microstructure was slightly reduced with test temperatures of 950 and 975°C which were both below the η solvus temperature. A certain set of samples was kept in the furnace after compression for 120 s at testing temperature to investigate meta-dynamic recrystallisation.

7.1.1 Dynamic and meta-dynamic recrystallisation

Previous studies on dynamic recrystallisation in 718Plus have shown, that the recrystallised fraction increases with strain rate, a finding which contradicts the trend observed in IN718 or Waspaloy. Recrystallisation is reported to decelerate when the strain rate is increased. This inconsistency was taken as opportunity to study the kinetics of recrystallisation in 718Plus in more detail.

From EBSD analysis of the samples after the compression tests, the influence of the test parameters on the characteristics of the recrystallised area were analysed. In-line with the

reported pattern, the recrystallised fraction increased with strain rate. This behaviour was attributed to a shift in recrystallisation mechanism from dDRX to cDRX [63, 64]. However, due to vague definitions of these terms and the lack of direct evidence, this study has analysed the microstructure in more detail by utilising a TEM. The TEM observations showed specific differences in the morphology of the recrystallised grains. DRX and MDRX could clearly be distinguished from the dislocation morphology using bright field imaging. The increase of the recrystallised fraction resulted from MDRX occurring during the transfer time between deformation and quench.

The γ-η microstructure presented the same relationship between strain rate and recrystallised fraction. A comparison between the η-free and η-containing microstructures was attempted cautiously due to the different initial grain sizes. The recrystallised area in the η microstructure consisted of smaller but more grains compared to the η-free samples. However, packets of fine, lamellar η seemed to inhibit a homogeneous recrystallisation of the sample. This mechanism was intensified at specimens which were kept in the furnace for 120 s to analyse MDRX. Dislocations between the η laths did not recover to subgrains from which recrystallisation could have proceeded. A narrow grain size distribution even after MDRX could be linked to the presence of η.

The kinetics of DRX in the current study contradicts to the common explanation which differentiates between discontinuous and continuous DRX (dDRX, cDRX). While the initial definition of these processes was based on location where DRX occurs, it has, over time, become confused with the underlying microstructural mechanisms. It was shown in this study, that, irrespective of strain rate, DRX forms subgrains near previously existing high-angle grain boundaries. These subgrains can trigger the bulging of the HAGBs and hence the formation of a recrystallised grain.

7.1.2 Flow curve characteristics

Modelling recrystallisation during forging in an industrial setting requires a mathematical description of the recrystallisation kinetics. The Johnson-Mehl-Avrami-Kolmogorov (JMAK) equation was utilised to reproduce the kinetics of DRX and MDRX. While this framework has already been applied to recrystallisation of γ-γ' 718Plus it was yet to be adapted for a γ-η microstructure.

For both microstructures, the flow curves were processed, together with the recrystallised fraction, to establish the necessary constants for empirical models. The Avrami-exponent fluctuated without an obvious trend with respect to the deformation parameters. This variation was related to two facts. Firstly, the test matrix contained only a few data points for each condition. Hence, the number of fitting nodes for the variables was limited. Secondly, the

original assumptions of the JMAK equation, such as a homogeneous distribution of the nuclei, are not valid for DRX. This would explain the scatter in the data and the absence of trends with deformation parameters.

The stress-strain curves of the compression tests all showed a single recrystallisation peak after the elastic region which is a characteristic that only one recrystallisation cycle has taken place. In addition, samples tested at the lower strain rates of 0.01 and $1s^{-1}$ displayed a yield point drop after reaching the yield point and the subsequent rise to the peak strain. Based on the observed trends of the yield point drop with the forging parameters it was suggested, that the underlying mechanism was the rapid formation of dislocations. However, this hypothesis was solely based on flow curve values and microscopical analysis of specimens deformed well beyond the yield point.

7.1.3 Deformation twinning and η straining

Deformation twinning is commonly referred as a low temperature and/or high strain rate mechanism in low stacking fault ccp materials. However, in the present study twins were found in 718Plus at temperatures as high as 1025°C and strain rates as low as $0.01s^{-1}$. To understand the formation of deformation twins in 718Plus under the given conditions a TEM analysis has been undertaken.

Significant amounts of deformation twinning have been identified during the examination of the samples. Twin packs spanning throughout the grain appeared in heavily deformed grains. The effect of deformation parameters on the twinning propensity was difficult to measure. However, the samples deformed at 850°C had a distinctly higher density of deformation twins compared to all other temperatures above the γ' solvus. A weak trend of twin density with strain rate was found with more twins at higher strain rates.

It was assumed, that a low stacking fault energy of 718Plus resulted in the wide splitting of the partial dislocations enabling twinning. The SFE of 718Plus has not been measured yet, hence triple points of dislocations were utilised to estimate the stacking fault energy of the γ phase at high temperatures. The SFE was calculated to $\sim$15 mJ m^{-2} which could be a possible explanation of the propensity of 718Plus to deformation twinning even at high temperatures.

Overlapping stacking faults could be repeatably captured in recrystallised grains. It is argued, that they are precursors for the nucleation mechanism of deformation twinning. These features were all found in grains with an otherwise low dislocation density. Therefore it is concluded, that work-hardening is not a necessary prerequisite for deformation twins to form.

The onset of twinning and possible nucleation mechanisms were discussed in the light of the found stacking fault features. Common to all examples was the formation close to a

low angle grain boundary. Most were also seen in small diameter grain sections. However, a clear pattern in the nucleation events throughout all cases was not possible.

The η precipitates deformed in two particular ways: via breakage and realignment of the particles and by severe bending of the precipitates. The former was believed to include the local dissolution of η which weakens the structure until it eventually breaks. The latter was owing to the composite nature of η together with the ongoing recrystallisation and reorientation of the γ matrix.

7.2 Future work

Based on the results and conclusions drawn from the present analysis a non-comprehensive list of subsequent areas of interest evolved.

7.2.1 Kinetics of dynamic recrystallisation

Even though great care was taken in the testing procedure, all samples experienced some degree of meta-dynamic recrystallisation due to the delay in quench. Hence, a flawless examination of the kinetics of dynamic recrystallisation in 718Plus was not possible. Within the time frame of the present work several attempts were taken to perform tests with an instantaneous quench, unfortunately none of these produced satisfactory results. However, it remains surprising that only tests on 718Plus and a few more studies reported an increase in recrystallised fraction with strain rate. While the test equipment in other studies ranged from immediate quench within the system to manual transfer, the trends seemed consistent with a decrease in DRX with increasing strain rate. Hence, compression tests with equipment which provides an immediate quench would improve out understanding of the role of strain rate in DRX of 718Plus.

The influence of η on recrystallisation remained unclear because of the difference in initial grain size between η-containing and η-free samples. A change in recrystallisation kinetics can be detected with an η test series with varying initial grain sizes.

7.2.2 Recrystallisation model

The compression tests were performed on cylindrical samples which increased the amount of work and test pieces compared to double-cone shaped specimens. However, cylindrical samples offer the advantage of a well-defined deformation environment of the specimen. The results can therefore be further used to develop a physically-based material model. Together

with the microstructural observations a model can be built to help explaining the role of η or the formation of deformation twins during high temperature compression testing.

7.2.3 Yield point drop during compression testing of nickel-base superalloys

The yield point phenomena of 718Plus has been reported and a possible conclusion was drawn from the flow curve trends. However, to successfully prove this assumption microstructural investigations are essential. The samples in this study have been deformed well above the yield point and couldn't be used for this purpose. A new set of interrupted compression tests around the yield point could help to shed light on this phenomenon.

7.2.4 Deformation mechanisms

Deformation twinning in 718Plus is the first well documented study on twinning at high temperatures and low strain rates in a low stacking fault ccp material. It remained unclear though, if the γ' particles or the temperature decrease increased the volume of deformation twins in the samples deformed at 850°C. Similarly, a quantification of twinned grains with testing parameters was not possible due to the restricted field of view in TEM samples. Assuming twins form at an early stage of deformation, subsequent tests can be performed at lower strains to open up the analysis techniques to ECCI. This SEM technique can offer statistically valid results on the kinetics of deformation twinning. Additionally, early stages of twinning can be observed in a higher quantity to develop a nucleation model for deformation twinning at these conditions.

References

[1] R. C. Reed. *The Superalloys: Fundamentals and Applications*. Cambridge University Press, 2006.

[2] S. Antonov, M. Detrois, R. C. Helmink, and S. Tin. Precipitate phase stability and compositional dependence on alloying additions in γ-γ'-δ-η Ni-base superalloys. *Journal of Alloys and Compounds*, 626:76–86, 2015.

[3] O. M. Messé, J. S. Barnard, E. J. Pickering, P. A. Midgley, and C. M. F. Rae. On the precipitation of delta phase in ALLVAC® 718Plus. *Philosophical Magazine*, 94(10):1132–1152, 2014.

[4] K. Huang and R. E. Logé. A review of dynamic recrystallization phenomena in metallic materials. *Materials and Design*, 111:548–274, 2016.

[5] R. Guest. *The dynamic and meta-dynamic recrystallisation of the ni-base superalloy Inconel 718*. PhD thesis, University of Cambridge, 2011.

[6] Rolls-Royce. *The Jet Engine*. St Ives Westerham Ltd, Edenbridge, UK, 6 edition, 2005.

[7] J. C. L. Goddard. *A Framework for a Dual Alloy Disc Development*. PhD thesis, University of Cambridge, 2015.

[8] J.M Oblak, D.S Duvall, and D.F Paulonis. An estimate of the strengthening arising from coherent, tetragonally-distorted particles. *Materials Science and Engineering*, 13(1):51 – 56, 1974.

[9] S. C. Medeiros, Y. V. R. K. Prasad, W. G. Frazier, and R. Srinivasan. Modeling Grain Size During Hot Deformation of in 718. *Scripta Materialia*, 42:17–23, 2000.

[10] R. L. Kennedy. Allvac® 718Plus™, Superalloy for the Next Forty Years. *Superalloys 718, 625, 706 and Derivatives*, 2005.

[11] I. Dempster, W. D. Cao, R. Kennedy, B. Bond, J. Aurrecoechea, and M. Lipschutz. Structure and Property Comparison of Allvac ® 718Plus ™ Alloy and Waspaloy Forgings. *Superalloys 718, 625, 706 and Derivatives 2005*, pages 155–164, 2005.

[12] R. L. Kennedy, W. Cao, T. D. Bayha, and R. Jeniski. Developments in Wrought Nb Containing Superalloys (718 + 100°F). *Superalloys 2003*, 2003.

[13] W. D. Cao and R. Kennedy. Role of chemistry in 718-type alloys - Allvac 718Plus alloy development. 3:1–10, 2004.

[14] D. Srinivasan, L. U. Lawless, and E. A. Ott. Experimental determination of TTT diagram for ally 718PLUS®. *Superalloys 2012*, 3:759–768, 2012.

[15] K. Löhnert. *Einfluss der thermomechanischen Vorbehandlung auf die Eigenschaften der Nickelbasissuperlegierung A718Plus*. PhD thesis, Universität Erlangen-Nürnberg, 2011.

[16] A. Casanova. *CPGS*. PhD thesis, University of Cambridge, 2013.

[17] A. Casanova, M. Hardy, and C. M. F. Rae. Morphology and Kinetics of Grain Boundary Precipitation in Alloy ATI 718Plus®. *8th International Symposium on Superalloy 718 and Derivatives*, pages 573–586, 2014.

[18] P. M. Mignanelli, N. G. Jones, M. C. Hardy, and H. J. Stone. The influence of Al: Nb ratio on the microstructure and mechanical response of quaternary Ni-Cr-Al-Nb alloys. *Materials Science and Engineering A*, 612:179–186, 2014.

[19] W. D. Cao and R. L. Kennedy. Recommendations for Heat Treating Allvac® 718Plus® Alloy Parts. Technical report, 2006.

[20] L. Whitmore, H. Leitner, E. Povoden-Karadeniz, R. Radis, and M. Stockinger. Transmission electron microscopy of single and double aged 718Plus superalloy. *Materials Science and Engineering A*, 534:413–423, 2012.

[21] W. D. Cao. Solidification and Solid State Phase Transformation of Allvac® 718Plus Alloy™. *Superalloys 718, 625, 706 and Various Derivatives, 2005*, pages 165–177, 2005.

[22] E. J. Pickering, H. Mathur, A. Bhowmik, O. M. Messé, J. S. Barnard, M. C. Hardy, R. Krakow, K. Löhnert, H. J. Stone, and C. M. F. Rae. Grain-boundary precipitation in Allvac 718Plus. *Acta Materialia*, 60:2757–2769, 2012.

[23] C. Sommitsch, D. Huber, I. S. Fredrik, S. Mitsche, M. Stockinger, and B. Buchmayr. Recrystallization and grain growth in the nickel-based superalloy Allvac 718Plus. *International Journal of Materials Research*, 100(8):1088–1098, 2009.

[24] X. Xie, G. Wang, J. Dong, C. Xu, W. D. Cao, and R. Kennedy. Structure Stability Study on a Newly Developed Nickel-Base Superalloy - Allvac 718Plus. *Superalloys 718, 625, 706 and Various Derivatives (2005)*, pages 179–191, 2005.

[25] A. Casanova, K. Loehnert, D. Huenert, M. Hardy, and C. M. F. Rae. Systematic evaluation of microstructural and thermo-mechanical effects on the as-forged condition of alloy ATI 718Plus®. *Superalloys 2016*, pages 427–436, 2016.

[26] A. Casanova, N. Martín-Piris, M. Hardy, and C. M. F. Rae. Evolution of secondary phases in alloy ATI 718Plus® during processing. *Eurosuperalloys 2014*, 2014.

[27] L. Viskari and K. Stiller. Atom probe tomography of Ni-base superalloys Allvac 718Plus and Alloy 718. *Ultramicroscopy*, 111(6):652–658, 2011.

[28] K. A. Unocic, R. W. Hayes, M. J. Mills, and G. S. Daehn. Microstructural features leading to enhanced resistance to grain boundary creep cracking in ALLVAC 718Plus. *Metallurgical and Materials Transactions A*, 41(2):409–420, 2010.

[29] R. Krakow, D. N. Johnstone, A. S. Eggeman, D. Hünert, M. C. Hardy, C. M. F. Rae, and P. A. Midgley. On the crystallography and composition of topologically close-packed phases in ATI 718Plus ®. *Acta Materialia*, 130:271–280, 2017.

[30] R. Krakow. *Microstructure and Mechanical Properties of Subsolvus Forged ATI718Plus*. PhD thesis, University of Cambridge, 2016.

[31] F. Jones. The structural evolution of superallloy ingots during hot working. *JOM*, 51(1):27–33, 1999.

[32] C. A. Dandre, S. M. Roberts, R. W. Evans, and R. C. Reed. A model describing microstructural evolution for Ni-base superalloy forgings during the cogging process. *Journal De Physique. IV: JP*, 9(33-42), 1999.

[33] E. McDevitt. Effect of temperature and strain during forging and subsequent delta phase precipitation during solution anneal in ATI 718PLUS ® alloy. *7th International Symposium on Superalloy 718 and Derivatives*, pages 307–319, 2010.

[34] D. Huenert, M. Proebstle, A. Casanova, R. Schluetter, R. Krakow, M. Buescher, P. Randelzhofer, A. Evans, K. Loehnert, T. Witulski, S. Neumeier, and C. M. F. Rae. ATI 718Plus® - New Nickel Based Disc Alloy And Its Capability. *Superalloys 2016*, 2016.

[35] F. J. Humphreys and M. Hatherly. *Recrystallization and Related Annealing Phenomena*. Elsevier Science Ltd, Oxford, 2 edition, 1996.

[36] D. Raabe. *23 - Recovery and Recrystallization: Phenomena, Physics, Models, Simulation*. Elsevier B.V., fifth edit edition, 2014.

[37] R. W. Cahn. A New Theory of Recrystallization Nuclei. *Proceedings of the Physical Society*, 63(4):323–336, 1950.

[38] T. Sakai, A. Belyakov, R. Kaibyshev, H. Miura, and J. J. Jonas. Dynamic and post-dynamic recrystallization under hot, cold and severe plastic deformation conditions. *Progress in Materials Science*, 60:130–207, 2014.

[39] B. Li and S. Tin. The role of deformation temperature and strain on grain boundary engineering of Inconel 600. *Materials Science and Engineering A*, 603:104–113, 2014.

[40] G. Gottstein, E. Brunger, M. Frommert, M. Goerdeler, and M. Zeng. Prediction of the critical conditions for dynamic recrystallization in metals. *Zeitschrift Für Metallkunde*, 94(5):628–635, 2003.

[41] G. Gottstein, T. Lee, and U. Schmidt. Deformation temperature and recrystallization. *Materials Science and Engineering A*, 114(C):21–28, 1989.

[42] R. D. Doherty, D. A. Hughes, F. J. Humphreys, J. J. Jonas, D. J. Jensen, M. E. Kassner, W. E. King, T. R. McNelley, H.J. McQueen, and A.D. Rollett. Current issues in recrystallization: a review. *Materials Science and Engineering: A*, 238(2):219–274, 1997.

[43] S. Mitsche, C. Sommitsch, D. Huber, M. Stockinger, and P. Poelt. Influence of Temperature and Strain Rate on Dynamic Softening Processes in Allvac® 718Plus™. *Materials Science Forum*, 706-709:2440–2445, 2012.

[44] L. X. Zhou and T. N. Baker. Effects on dynamic and metadynamic recrystallization on microstructures of wrought IN-718 due to hot deformation. *Materials Science and Engineering: A*, 196(1-2):89–95, 1995.

[45] N. K. Park, I. S. Kim, Y. S. Na, and J. T. Yeom. Hot forging of a nickel-base superalloy. *Journal of Materials Processing Technology*, 111:98–102, 2001.

[46] C. Sommitsch, D. Huber, and M. Stockinger. Metadynamic Recrystallization of the Nickel-Based Superalloy Allvac 718PlusTM. *Materials Science Forum*, 638-642:2327–2332, 2010.

[47] P. Uranga, A. I. Fernández, B. López, and J. M. Rodriguez-Ibabe. Transition between static and metadynamic recrystallization kinetics in coarse Nb microalloyed austenite. *Materials Science and Engineering: A*, 345(1-2):319–327, 2003.

[48] L. P. Karjalainen and J. Perttula. Characteristics of Static and Metadynamic Recrystallization and Strain Accumulation in Hot-deformed Austenite as Revealed by the Stress Relaxation Method. *ISIJ International*, 36(6):729–736, 1996.

[49] C. Haase, M. Kühbach, L. A. Barrales-Mora, S. L. Wong, F. Roters, D. A. Molodov, and G. Gottstein. Recrystallization behavior of a high-manganese steel: Experiments and simulations. *Acta Materialia*, 100:155–168, 2015.

[50] W. Xu, M. Z. Quadir, and M. Ferry. A high-resolution three-dimensional electron backscatter diffraction study of the nucleation of recrystallization in cold-rolled extra-low-carbon steel. *Metallurgical and Materials Transactions A: Physical Metallurgy and Materials Science*, 40(7):1547–1556, 2009.

[51] H. Ahlborn, E. Hornbogen, and U. Köster. Recrystallisation mechanism and annealing texture in aluminium-copper alloys. *Journal of Materials Science*, 4(11):944–950, 1969.

[52] J. K. Solberg, H. J. McQueen, N. Ryum, and E. Nes. Influence of ultra-high strains at elevated temperatures on the microstructure of aluminium. Part I. *Philosophical Magazine A: Physics of Condensed Matter, Structure, Defects and Mechanical Properties*, 60(4):447–471, 1989.

[53] H. Liang, H. Guo, K. Tan, Y. Q. Ning, X. Luo, G. Cao, J. Wang, and P. Zhen. Correlation between grain size and flow stress during steady-state dynamic recrystallization. *Materials Science and Engineering A*, 638:357–362, 2015.

[54] G. Shen, S. L. Semiatin, and R. Shivpuri. Modeling microstructural development during the forging of Waspaloy. *Metallurgical and Materials Transactions A*, 26(7):1795–1803, 1995.

[55] E. I. Galindo-Nava and C. M. F. Rae. Microstructure evolution during dynamic recrystallisation in polycrystalline nickel superalloys. *Materials Science & Engineering A*, 636:434–445, 2015.

[56] J. J. Jonas, C. M. Sellars, and W. J. Tegart. Strength and structure under hot-working conditions. *International Metallurgical Reviews*, 14(1):1–24, 1969.

[57] A. Chamanfar, M. Jahazi, J. Gholipour, P. Wanjara, and S. Yue. Evolution of flow stress and microstructure during isothermal compression of Waspaloy. *Materials Science and Engineering A*, 615:497–510, 2014.

[58] S. Mitsche, P. Poelt, and C. Sommitsch. Recrystallization behaviour of the nickel-based alloy 80 A during hot forming. *Journal of Microscopy*, 227(3):267–274, 2007.

[59] H. Jiang, J. Dong, M. Zhang, and Z. Yao. Evolution of twins and substructures during low strain rate hot deformation and contribution to dynamic recrystallization in alloy 617B. *Materials Science and Engineering A*, 649:369–381, 2016.

[60] H. Zhang, K. Zhang, H. Zhou, Z. Lu, C. Zhao, and X. Yang. Effect of strain rate on microstructure evolution of a nickel-based superalloy during hot deformation. *Materials & Design*, 80:51–62, 2015.

[61] M. Azarbarmas, M. Aghaie-Khafri, J. M. Cabrera, and J. Calvo. Microstructural evolution and constitutive equations of Inconel 718 alloy under quasi-static and quasi-dynamic conditions. *Materials and Design*, 94:28–38, 2016.

[62] S. S. Kumar, T. Raghu, P. P. Bhattacharjee, G. A. Rao, and U. Borah. Strain rate dependent microstructural evolution during hot deformation of a hot isostatically processed nickel base superalloy. *Journal of Alloys and Compounds*, 2016.

[63] A. Momeni, S. M. Abbasi, M. Morakabati, and H. Badri. A Comparative Study on the Hot Working Behavior of Inconel 718 and ALLVAC 718 Plus. *Metallurgical and Materials Transactions A*, 48(3):1216–1229, 2017.

[64] S. Mitsche, C. Sommitsch, D. Huber, M. Stockinger, and P. Poelt. Assessment of dynamic softening mechanisms in Allvac® 718Plus™ by EBSD analysis. *Materials Science and Engineering: A*, 528(10-11):3754–3760, 2011.

[65] E. I. Poliak and J. J. Jonas. Initiation of Dynamic Recrystallization in Constant Strain Rate Hot Deformation. *ISIJ International*, 43(5):684–691, 2003.

[66] T. Sakai and J. J. Jonas. Overview no. 35 Dynamic recrystallization: Mechanical and microstructural considerations. *Acta Metallurgica*, 32(2):189–209, 1984.

[67] C. Zhang, L. Zhang, W. Shen, C. Liu, and Y. Xia. The Kinetics of Metadynamic Recrystallization in a Ni-Cr-Mo-Based Superalloy Hastelloy C-276. *Journal of Materials Engineering and Performance*, 25(2):545–552, 2016.

[68] M. Aghaie-Khafri and N. Golarzi. Dynamic and metadynamic recrystallization of Hastelloy X superalloy. *Journal of Materials Science*, 43(10):3717–3724, 2008.

[69] R. A. P. Djaic and J. J. Jonas. Recrystallization of high carbon steel between intervals of high temperature deformation. *Metallurgical Transactions*, 4(2):621–624, 1973.

[70] P. R. Rios, F. Siciliano Jr, H. R. Zschommler Sandim, R. L. Plaut, and A. F. Padilha. Nucleation and growth during recrystallization. *Materials Research*, 8(3):225–238, 2005.

[71] A. H. Cottrell. Theory of dislocations. *Progress in Metal Physics*, 4:205–264, 1953.

[72] H. N. Mathur, N. Jones, and C. M. F. Rae. A study on the effect of composition, and the mechanisms of recrystallisation in single crystal Ni-based superalloys. *MATEC Web of Conferences*, 14:07003, 2014.

[73] G. Herrmann, H. Gleiter, and G. Baero. Investigation of low energy grain boundaries in metals by a sintering technique. *Acta Metallurgica*, 24(4):353–359, 1976.

[74] D. Molodov, L. Barrales-Mora, and J. Brandenburg. Grain boundary motion and grain rotation in aluminum bicrystals: recent experiments and simulations. *IOP Conference Series: Materials Science and Engineering*, 89:012008, 2015.

[75] W. Wang, F. Brisset, A. L. Helbert, D. Solas, I. Drouelle, M. H. Mathon, and T. Baudin. Influence of stored energy on twin formation during primary recrystallization. *Materials Science and Engineering A*, 589:112–118, 2014.

[76] D. Li, Q. Guo, S. Guo, H. Peng, and Z. Wu. The microstructure evolution and nucleation mechanisms of dynamic recrystallization in hot-deformed Inconel 625 superalloy. *Materials & Design*, 32(2):696–705, 2011.

[77] Q. Guo, D. Li, H. Peng, S. Guo, J. Hu, and P. Du. Nucleation mechanisms of dynamic recrystallization in Inconel 625 superalloy deformed with different strain rates. *Rare Metals*, 31(3):215–220, 2012.

[78] A. Belyakov, H. Miura, and T. Sakai. Dynamic recrystallization under warm deformation of a 304 type austenitic stainless steel. *Materials Science & Engineering A*, 255:139–147, 1998.

[79] S. Mahajan. Critique of mechanisms of formation of deformation, annealing and growth twins: Face-centered cubic metals and alloys. *Scripta Materialia*, 68(2):95–99, 2013.

[80] H. Gleiter. The formation of annealing twins. *Acta Metallurgica*, 17(12):1421–1428, 1969.

[81] C. S. Pande, M. Imam, and B. B. Rath. Study of annealing twins in fcc metals and alloys. *Metallurgical Transactions A*, 21(11):2891–2896, 1990.

[82] C. M. F Rae, C. R. M. Grovenor, and K. M. Knowles. Multiple twinning and recrystallisation. *Zeitschrift füer Metallkunde*, 72(11):798–802, 1981.

[83] P. W. Davies, A. P. Greenough, and B. Wilshire. The ledge theory of recrystallization in polycrystalline metals. *Philosophical Magazine*, 6(66):795–799, 1961.

[84] K. Huang, K. Marthinsen, Q. Zhao, and R. E. Logé. The double-edge effect of second-phase particles on the recrystallization behaviour and associated mechanical properties of metallic materials. *Progress in Materials Science*, 92:284–359, 2018.

[85] I. Baker and J. W. Martin. The effect of particle size and spacing on the retardation of recrystallization in two-phase copper crystals. *Journal of Materials Science*, 15(6):1533–1538, 1980.

[86] F. J. Humphreys and J. W. Martin. The effect of dispersed silica particles on the recovery and recrystallization of deformed copper crystals. *Acta Metallurgica*, 14(6):775–781, 1966.

[87] C. S. Smith. *Grains, Phases, and Interfaces: An Interpretation of Microstructure*, volume 175. 1948.

[88] N. Hansen and B. Bay. The effect of particle content, particle distribution and cold deformation on the recrystallization of low oxide Al-Al2O3 products. *Journal of Materials Science*, 7(12):1351–1362, 1972.

[89] E. Z. Silva, H. Kestler, and H. R.Z. Sandim. Particle-stimulated nucleation of recrystallization in the hot-deformed molybdenum alloy MZ-17. *International Journal of Refractory Metals and Hard Materials*, 73(January):74–78, 2018.

[90] Elena V. Pereloma, Parvez Mannan, Gilberto Casillas, and Ahmed A. Saleh. Particle stimulated nucleation during dynamic and metadynamic recrystallisation of Ni-30%Fe-Nb-C alloy. *Materials Characterization*, 125:94–98, 2017.

[91] S. L. Semiatin, D. S. Weaver, P. N. Fagin, M. G. Glavicic, R. L. Goetz, N. D. Frey, R. C. Kramb, and M. M. Antony. Deformation and recrystallization behavior during hot working of a coarse-grain, nickel-base superalloy ingot material. *Metallurgical and Materials Transactions A: Physical Metallurgy and Materials Science*, 35 A(2):679–693, 2004.

[92] R. L. Goetz. Particle stimulated nucleation during dynamic recrystallization using a cellular automata model. *Scripta Materialia*, 52(9):851–856, 2005.

[93] M. Pérez. Microstructural evolution of Nimonic 80a during hot forging under non-isothermal conditions of screw press. *Journal of Materials Processing Technology*, 252(February 2017):45–57, 2018.

[94] M. J. Donachie and S. J. Donachie. *Superalloys - A Technical Guide - 2nd edition*. ASM International, Ohio, 2002.

[95] H. M. Lalvani and J. W. Brooks. Hot Forging of IN718 with Solution-Treated and Delta-Containing Initial Microstructures. *Metallography, Microstructure, and Analysis*, 5(5):392–401, 2016.

[96] Y. Wang, W. Z. Shao, L. Zhen, and B. Y. Zhang. Hot deformation behavior of delta-processed superalloy 718. *Materials Science and Engineering A*, 528(7-8):3218–3227, 2011.

[97] H. Zhang, H. Zhou, S. Qin, J. Liu, and X. Xu. Effect of deformation parameters on twinning evolution during hot deformation in a typical nickel-based superalloy. *Materials Science & Engineering A*, 696(April):290–298, 2017.

[98] H. Lalvani, M. Rist, and J. W. Brooks. Effect of Delta Phase on the Hot Deformation Behaviour and Microstructural Evolution of Inconel 718. 91(January):313–318, 2010.

[99] M. Detrois, R. C. Helmink, and S. Tin. Hot deformation characteristics of a polycrystalline γ-γ'-δ ternary eutectic Ni-base superalloy. *Materials Science and Engineering A*, 586:236–244, 2013.

[100] M. A. Charpagne, T. Billot, J. M. Franchet, and N. Bozzolo. Heteroepitaxial recrystallization: A new mechanism discovered in a polycrystalline γ-γ' nickel based superalloy. *Journal of Alloys and Compounds*, 688:685–694, 2016.

[101] M. A. Charpagne, P. Vennéguès, T. Billot, J. M. Franchet, and N. Bozzolo. Evidence of multimicrometric coherent γ' precipitates in a hot-forged γ-γ' nickel-based superalloy. *Journal of Microscopy*, 263(1):106–112, 2016.

[102] M. Charpagne, T. Billot, J. Franchet, and N. Bozzolo. Heteroepitaxial Recrystallization Observed in René 65™ and Udimet 720™: a New Recrystallization Mechanism Possibly Occurring in All Low Lattice Mismatch $\gamma - \gamma$' superalloys? *Superalloys 2016*, pages 417–426, 2016.

[103] V. M. Miller, E. J. Payton, and A. L. Pilchak. Reduction in the thermodynamic nucleation barrier via the heteroepitaxial recrystallization mechanism. *Scripta Materialia*, 136:128–131, 2017.

[104] K. Song and M. Aindow. Grain growth and particle pinning in a model Ni-based superalloy. *Materials Science and Engineering A*, 479:365–372, 2008.

[105] Y. Jin, B. Lin, M. Bernacki, G. S. Rohrer, A. D. Rollett, and N. Bozzolo. Annealing twin development during recrystallization and grain growth in pure nickel. *Materials Science and Engineering A*, 597:295–303, 2014.

[106] Kochmann Research group Caltech. From atoms to macroscale: the nonlocal quasicontinuum method. http://www.kochmann.caltech.edu/research_QC.html. last accessed 26-01-2017.

[107] F. R. N. Nabarro and H. L. de Villiers. *The Physics of Creep*. Taylor&Francis, London, UK, 1995.

[108] Y. Cao, H. Di, J. Zhang, J. Zhang, T. Ma, and R. Misra. An electron backscattered diffraction study on the dynamic recrystallization behavior of a nickel-chromium alloy (800H) during hot deformation. *Materials Science and Engineering A*, 585:71–85, 2013.

[109] J. S. Perttula and L. P. Karjalainen. Recrystallisation rates in austenite measured by double compression and stress relaxation methods. *Materials Science and Technology*, 14(7):626–630, 1998.

[110] X. Zhao, R. P. Guest, S. Tin, D. Cole, J. W. Brooks, and M. Peers. Modelling hot deformation of Inconel 718 using state variables. *Materials Science and Technology*, 20(11):1414–1420, 2004.

[111] M. Avrami. Kinetics of Phase Change. II Transformation-Time Relations for Random Distribution of Nuclei. *The Journal of Chemical Physics*, 8:212–224, 1940.

[112] B. Radhakrishnan, G. B. Sarma, and T. Zacharia. Modeling the kinetics and microstructural evolution during static recrystallizationð monte carlo simulation of recrystallization. *Acta Metallurgica*, 46(12):4415–4433, 1998.

[113] D. Huang, W. T. Wu, D. Lambert, and S. L. Semiatin. Computer Simulation of Microstructure Evolution during Hot Forging of Waspaloy and Nickel Alloy 718. *Microstructure Modeling and Prediction During Thermomechanical processing*, pages 137–146, 2001.

[114] W. Roberts and B. Ahlblom. A nucleation criterion for dynamic recrystallization during hot working. *Acta Metallurgica*, 26:801–813, 1978.

[115] E. I. Galindo-Nava and P. E. J. Rivera-Díaz-Del-Castillo. Grain size evolution during discontinuous dynamic recrystallization. *Scripta Materialia*, 2013.

[116] H. Hallberg. Approaches to Modeling of Recrystallization. *Metals*, 1:16–48, 2011.

[117] M. Kühbach and G. Gottstein. A statistical ensemble cellular automaton microstructure model for primary recrystallization. *Acta Materialia*, 107:366–376, 2016.

[118] J. De Jaeger, D. Solas, O. Fandeur, J. Schmitt, and C. Rey. 3D numerical modeling of dynamic recrystallization under hot working: Application to Inconel 718. *Materials Science and Engineering: A*, 646:33–44, oct 2015.

[119] Y. Jin, N. Bozzolo, A. D. Rollett, and M. Bernacki. 2D finite element modeling of misorientation dependent anisotropic grain growth in polycrystalline materials: Level set versus multi-phase-field method. *Computational Materials Science*, 104:108–123, 2015.

[120] B. Scholtes, M. Shakoor, A. Settefrati, P. Bouchard, N. Bozzolo, and M. Bernacki. New finite element developments for the full field modeling of microstructural evolutions using the level-set method. *Computational Materials Science*, 109:388–398, 2015.

[121] A. Agnoli, N. Bozzolo, R. Logé, J. Franchet, J. Laigo, and M. Bernacki. Development of a level set methodology to simulate grain growth in the presence of real secondary phase particles and stored energy - Application to a nickel-base superalloy. *Computational Materials Science*, 89:233–241, 2014.

[122] N. Moelans, A. Godfrey, Y. Zhang, and D. J. Jensen. Phase-field simulation study of the migration of recrystallization boundaries. *Physical Review B*, 88(054103), 2013.

[123] N. Moelans, B. Blanpain, and P. Wollants. Quantitative analysis of grain boundary properties in a generalized phase field model for grain growth in anisotropic systems. *Physical Review B*, 78(024113), 2008.

[124] N. Provatas and K. Elder. *Phase-Field Methods in Material Science and Engineering*. 2010.

[125] C. A. Schneider, W. S. Rasband, and K. W. Eliceiri. NIH Image to ImageJ: 25 years of Image Analysis HHS Public Access. *Nature Methods*, 9(7):671–675, 2012.

[126] A. Winkelmann, G. Nolze, M. Vos, F. Salvat-Pujol, and W. Werner. Physics-based Simulation Models for EBSD: Advances and Challenges. 2015.

[127] F. Bachmann, Ralf Hielscher, and Helmut Schaeben. Texture Analysis with MTEX – Free and Open Source Software Toolbox. *Solid State Phenomena*, 160:63–68, 2010.

[128] Oxford Instruments HKL. *Channel 5*. Oxford Instruments HKL, Denmark, 2007.

[129] D. G. Brandon. The Structure of High-Angle Grain Boundaries. *Acta Metallurgica*, 14:1479–1484, 1966.

[130] D. B. Williams and C. B. Carter. *Transmission Electron Microscopy*. Springer, New York, 2009.

[131] Scientific Forming Technologies Corporation. *DEFORM™ 2D Version 8*. SF, Ohio, USA.

[132] ATI Allvac. 718Plus Data Sourcebook. pages 1–71, 2008.

[133] A. A. Gazder, M. Sánchez-Araiza, J. J. Jonas, and E. V. Pereloma. Evolution of recrystallization texture in a 0.78 wt.% Cr extra-low-carbon steel after warm and cold rolling. *Acta Materialia*, 59(12):4847–4865, 2011.

[134] M. Zouari, N. Bozzolo, and Roland E. Logé. Mean field modelling of dynamic and post-dynamic recrystallization during hot deformation of Inconel 718 in the absence of δ phase particles. *Materials Science and Engineering A*, 655:408–424, 2016.

[135] M. Azarbarmas, M. Aghaie-Khafri, J. M. Cabrera, and J. Calvo. Dynamic recrystallization mechanisms and twining evolution during hot deformation of Inconel 718. *Materials Science and Engineering A*, 678(September):137–152, 2016.

[136] A. Nicolaÿ, J.M. Franchet, J. Cormier, H. Mansour, M. De Graef, A. Seret, and N. Bozzolo. Discrimination of dynamically and post-dynamically recrystallized grains based on ebsd data: application to inconel 718. *Journal of Microscopy*, 273(2):135–147, 2019.

[137] W. Wang, S. Lartigue-Korinek, F. Brisset, A. L. Helbert, J. Bourgon, and T. Baudin. Formation of annealing twins during primary recrystallization of two low stacking fault energy Ni-based alloys. *Journal of Materials Science*, 50(5):2167–2177, 2015.

[138] M. L. Brogdon. *The effect of as-large-as (ALA) grains on the high-temperature fatigue of Waspaloy*. PhD thesis, University of Dayton Research Insitute, 2006.

[139] S. C. Medeiros, Y. V. R. K Prasad, W. G. Frazier, and R. Srinivasan. Microstructural modeling of metadynamic recrystallization in hot working of IN 718 superalloy. *Materials Science and Engineering: A*, 293(1-2):198–207, 2000.

[140] ASTM Standard E209-00. *Standard Practice for Compression Tests of Metallic Materials at Elevated Temperatures with Conventional or Rapid Heating Rates and Strain Rates*. West Conshohocken, PA, 2010.

[141] B. Roebuck, J. D. Lord, M. Brooks, M. S. Loveday, C. M. Sellars, R. W. Evans, J. D. Lord, M. Brooks, M. S. Loveday, C. M. Sellars, and R. W. Evans. Materials at High Temperatures Measurement of flow stress in hot axisymmetric compression tests Measurement of flow stress in hot axisymmetric compression tests. 3409, 2014.

[142] M. C. Mataya and V. E. Sackschewsky. Effect of internal heating during hot compression on the stress-strain behavior of alloy 304l. *Metallurgical and Materials Transactions A*, 25(12):2737, Dec 1994.

[143] D. Zhao. Temperature correction in compression tests. *Journal of Materials Processing Technology*, 36(4):467 – 471, 1993.

[144] R. Ebrahimi and A. Najafizadeh. A new method for evaluation of friction in bulk metal forming. *Journal of Materials Processing Technology*, 152(2):136 – 143, 2004.

[145] S. Solhjoo. A note on "barrel compression test": A method for evaluation of friction. *Computational Materials Science*, 49(2):435 – 438, 2010.

[146] P. Dadras and J. F. Thomas. Characterization and modeling for forging deformation of ti-6ai-2sn-4zr-2mo-0.1 si. *Metallurgical Transactions A*, 12(11):1867–1876, Nov 1981.

[147] R. L. Goetz and S. L. Semiatin. The adiabatic correction factor for deformation heating during the uniaxial compression test. *Journal of Materials Engineering and Performance*, 10(6):710–717, Dec 2001.

[148] R.W. Evans and P.J. Scharning. Axisymmetric compression test and hot working properties of alloys. *Materials Science and Technology*, 17(8):995–1004, 2001.

[149] W. F. Smith and J. Hashemi. *Foundation of Material Science and Engineering*. McGraw-Hill, PA, USA, 2006.

[150] A. A. Guimaraes and J. J. Jonas. Recrystallization and aging effects associated with the high temperature deformation of waspaloy and inconel 718. *Metallurgical Transactions A*, 12(9):1655–1666, 1981.

[151] H. Monajati, M. Jahazi, S. Yue, and A. K. Taheri. Deformation characteristics of isothermally forged UDIMET 720 nickel-base superalloy. *Metallurgical and Materials Transactions a-Physical Metallurgy and Materials Science*, 36A(4):895–905, 2005.

[152] A. H. Cottrell and B. A. Bilby. Dislocation theory of yielding and strain ageing of iron. *Proceedings of the Physical Society. Section A*, 62(1):49–62, jan 1949.

[153] G-M. Han, C-G. Tian, C-Y Cui, and Sun X-F. Portevin-Le Chatelier Effect in Nimonic 263 Superalloy. *Acta Metallurgica Sinica(English Letters)*, 5(28):542–549, 2015.

[154] A. K Jena, K. P. M. G. S Gupta, and Murthy V. S. R. *Structure and Properties of Engineering Materials*. Tata McGraw-Hill, India, 2003.

[155] Y. C. Lin, M-S. Chen, and J. Zhong. Constitutive modeling for elevated temperature flow behavior of 42CrMo steel. *Computational Materials Science*, 42(3):470–477, 2008.

[156] C. M. Sellars and W. J. M. Tegart. Hot Workability. *International Metallurgical Reviews*, 17(1):1–24, 1972.

[157] A. Momeni, K. Dehghani, G. R. Ebrahimi, and H. Keshmiri. Modeling the flow curve characteristics of 410 martensitic stainless steel under hot working condition. *Metallurgical and Materials Transactions A: Physical Metallurgy and Materials Science*, 41(11):2898–2904, 2010.

[158] D. Huber, C. Sommitsch, S. Mitsche, P. Poelt, B. Buchmayr, and M. Stockinger. Microstructure modeling of the dynamic recrystallization kinetics during turbine disc forging of the nickel based superalloy Allvac 718Plus. *Superalloys 2008*, 2008.

[159] R. Abbaschian. *Physical metallurgy principles.* Cengage Learning, Stamford, Conn., 4th ed., si [ed.] / reza abbaschian, lara abbaschian, robert e. reed-hill. edition, 2010.

[160] Dong Xu, Miaoyong Zhu, Zhengyou Tang, and Chao Sun. Determination of the dynamic recrystallization kinetics model for SCM435 steel. *Journal Wuhan University of Technology, Materials Science Edition*, 28(4):819–824, 2013.

[161] S-H. Cho and Y-C. Yoo. Metadynamic recrystallization of austenitic stainless steel. *Journal of Materials Science*, 36(17):4279–4284, Sep 2001.

[162] A. Momeni, S.M. Abbasi, and A. Shokuhfar. Dynamic and metadynamic recrystallization of a martensitic precipitation hardenable stainless steel. *Canadian Metallurgical Quarterly*, 46(2):189–193, 2007.

[163] U. Ozturk, J. M. Cabrera, and J. Calvo. High temperature deformation of Inconel 718Plus. *Proceedings of ASME Turbo Expo 2016: Turbomachinery Technical Conference and Exposition*, pages 1–10, 2016.

[164] P. Páramo-Kañetas, U. Özturk, J. Calvo, J. M. Cabrera, and M. Guerrero-Mata. High-temperature deformation of delta-processed Inconel 718. *Journal of Materials Processing Technology*, 255(March 2017):204–211, 2018.

[165] Y-S. Na, J-T. Yeom, N-K. Park, and J-Y. Lee. Simulation of microstructures for alloy 718 blade forging using 3d fem simulator. *Journal of Materials Processing Technology*, 141(3):337 – 342, 2003.

[166] ASTM Standard E1382-97. *Standard Test Methods for Determining Average Grain Size Using Semiautomatic and Automatic Image Analysis*. West Conshohocken, PA, 2015.

[167] J. W. Cahn. The kinetics of grain boundary nucleated reactions. *Acta Metallurgica*, 4(5):449 – 459, 1956.

[168] G. Gottstein, M. Frommert, M. Goerdeler, and N. Schäfer. Prediction of the critical conditions for dynamic recrystallization in the austenitic steel 800H. *Materials Science and Engineering A*, 387-389(1-2 SPEC. ISS.):604–608, 2004.

[169] A Kelly and K. M. Knowles. *Crystallography and Crystal Defects*, chapter Twinning, pages 335–361. John Wiley & Sons, Ltd, 2012.

[170] B. C. De Cooman, Y. Estrin, and S. K. Kim. Twinning-induced plasticity (twip) steels. *Acta Materialia*, 142:283 – 362, 2018.

[171] S. Mahajan and G. Y. Chin. Formation of deformatin twins in f.c.c. crystals. *Acta Metallurgica*, 21:1353–1363, 1973.

[172] C. Haase and L. A. Barrales-Mora. Influence of deformation and annealing twinning on the microstructure and texture evolution of face-centered cubic high-entropy alloys. *Acta Materialia*, 150:88–103, 2018.

[173] D. Zhang, L. Jiang, B. Zheng, J. M. Schoenung, S. Mahajan, E. J. Lavernia, I. J. Beyerlein, J. M. Schoenung, and E. J. Lavernia. *Deformation Twinning (Update)*. Number December. Elsevier Ltd., 2016.

[174] T. M. Smith, M. S. Hooshmand, B. D. Esser, F. Otto, D. W. McComb, E. P. George, M. Ghazisaeidi, and M. J. Mills. Atomic-scale characterization and modeling of 60° dislocations in a high-entropy alloy. *Acta Materialia*, 110:352–363, 2016.

[175] J. J. Moverare, S. J., and R. C. Reed. Deformation and damage mechanisms during thermal–mechanical fatigue of a single-crystal superalloy. *Acta Materialia*, 57(7):2266 – 2276, 2009.

[176] H.U. Hong, J.G. Kang, B.G. Choi, I.S. Kim, Y.S. Yoo, and C.Y. Jo. A comparative study on thermomechanical and low cycle fatigue failures of a single crystal nickel-based superalloy. *International Journal of Fatigue*, 33(12):1592 – 1599, 2011.

[177] J. Nordström, R. Siriki, J. Moverare, and G. Chai. Deformation Twinning Behavior in High Ni-Austenitic Materials. *Materials Science Forum*, 941:1591–1596, 2018.

[178] E. Pu, W. Zheng, Z. Song, H. Feng, and H. Dong. Hot deformation characterization of nickel-based superalloy UNS10276 through processing map and microstructural studies. *Journal of Alloys and Compounds*, 694:617–631, 2017.

[179] M. Eskandari, A. Zarei-Hanzaki, J.A. Szpunar, M.A. Mohtadi-Bonab, A.R. Kamali, and M. Nazarian-Samani. Microstructure evolution and mechanical behavior of a new microalloyed high mn austenitic steel during compressive deformation. *Materials Science and Engineering: A*, 615:424 – 435, 2014.

[180] T. E. J. Edwards, F. Di Gioacchino, G. Mohanty, J. Wehrs, J. Michler, and W. J. Clegg. Longitudinal twinning in a TiAl alloy at high temperature by in situ microcompression. *Acta Materialia*, 148:202–215, 2018.

[181] S. Mahajan. Formation of Deformation Twins in Metallic Crystals. *Acta Metallurgica*, 49:2005, 2005.

[182] I. J. Beyerlein, X. Zhang, and A. Misra. Growth Twins and Deformation Twins in Metals. *Annual Review of Materials Research*, 44(1):329–363, 2014.

[183] F. Diologent and P. Caron. On the creep behavior at 1033k of new generation single-crystal superalloys. *Materials Science and Engineering: A*, 385(1):245 – 257, 2004.

[184] S. Ma, L. Carroll, and T.M. Pollock. Development of γ phase stacking faults during high temperature creep of ru-containing single crystal superalloys. *Acta Materialia*, 55(17):5802 – 5812, 2007.

[185] Y. Yuan, Y.F. Gu, C.Y. Cui, T. Osada, T. Tetsui, T. Yokokawa, and H. Harada. Creep mechanisms of u720li disc superalloy at intermediate temperature. *Materials Science and Engineering: A*, 528(15):5106 – 5111, 2011.

[186] D. Hull and D. J. Bacon. *Introduction to Dislocations*. Elsevier Ltd., 5 edition, 2011.

[187] S. K. Pradhan, S. Mandal, C. N. Athreya, K. A. Babu, B. de Boer, and V. S. Sarma. Influence of processing parameters on dynamic recrystallization and the associated annealing twin boundary evolution in a nickel base superalloy. *Materials Science and Engineering A*, 700, 2017.

[188] H. Idrissi, K. Renard, L. Ryelandt, D. Schryvers, and P. J. Jacques. On the mechanism of twin formation in fe–mn–c twip steels. *Acta Materialia*, 58(7):2464 – 2476, 2010.

[189] I. Gutierrez-Urrutia, S. Zaefferer, and D. Raabe. The effect of grain size and grain orientation on deformation twinning in a fe–22wt.*Materials Science and Engineering: A*, 527(15):3552 – 3560, 2010.

[190] S. S. Cai, X. W. Li, and N. R. Tao. Orientation dependence of deformatin twinning in cu single crystals. *Journal of Materials Science & Technology*, 34:1364–1370, 2018.

[191] L. Kovarik, R. R. Unocic, Ju Li, P. Sarosi, C. Shen, Y. Wang, and M. J. Mills. Microtwinning and other shearing mechanisms at intermediate temperatures in Ni-based superalloys. *Progress in Materials Science*, 54(6):839–873, 2009.

[192] M. Kolbe. The high temperature decrease of the critical resolved shear stress in nickel-base superalloys. *Materials Science and Engineering: A*, 319-321:383 – 387, 2001.

[193] Xi Zhang, Blazej Grabowski, Fritz Körmann, Andrei V Ruban, Yilun Gong, and Roger C Reed. Temperature dependence of the stacking-fault Gibbs energy for Al , Cu , and Ni. *Phys. Rev. B*, 224106, 2018.

[194] S. L. Shang, D. E. Kim, C. L. Zacherl, Y. Wang, Y. Du, and Z. K. Liu. Effects of alloying elements and temperature on the elastic properties of dilute Ni-base superalloys from first-principles calculations. *Journal of Applied Physics*, 112(5), 2012.

[195] L. Rémy, A. Pineau, and B. Thomas. Temperature dependence of stacking fault energy in close-packed metals and alloys. *Materials Science and Engineering*, 36(1):47 – 63, 1978.

[196] S. Mahajan, C. S. Pande, M. A. Imam, and B. B. Rath. Formation of annealing twins in f.c.c. crystals. *Acta Metallurgica*, 45(6):2633–2638, 1997.

[197] T. M. Smith, B. D. Esser, B. Good, M. S. Hooshmand, G. B. Viswanathan, C. M. F. Rae, M. Ghazisaeidi, D. W. McComb, and M. J. Mills. Segregation and Phase Transformations Along Superlattice Intrinsic Stacking Faults in Ni-Based Superalloys. *Metallurgical and Materials Transactions A*, (June), 2018.

[198] T. M. Smith, B. D. Esser, N. Antolin, G. B. Viswanathan, T. Hanlon, A. Wessman, D. Mourer, W. Windl, D. W. Mccomb, and M. J. Mills. Segregation and Î· phase formation along stacking faults during creep at intermediate temperatures in a Ni-based superalloy. *Acta Materialia*, 100:19–31, 2015.

[199] Y. T. Zhu. Deformation Twinning in Nanocrystalline Metals. *Journal of Materials Engineering and Performance*, 14(August):467–472, 2005.

[200] J. A. Venables. Deformation twinning in face-centred cubic metals. *The Philosophical Magazine: A Journal of Theoretical Experimental and Applied Physics*, 6(63):379–396, 1961.

[201] S. Miura, J. Takamura, and N. Narita. Orientation dependence of the flow stress for twinning in silver crystals. pages 555–562, 1967. cited By 12.

[202] A. H. Cottrell. The formation of immobile dislocations during slip. *The London, Edinburgh, and Dublin Philosophical Magazine and Journal of Science*, 43(341):645–647, 1952.

[203] J. B. Cohen and J. Weertman. A dislocation model for twinning in f.c.c. metals. *Acta Metallurgica*, 11:996, 1963.

[204] T. Mori and H. Fujita. Dislocation reactions during deformation twinning in Cu-11at.% Al single crystals. *Acta Metallurgica*, 28(6):771–776, 1980.

[205] C. T. Rueden, J. Schindelin, M. C. Hiner, B. E. DeZonia, A. E. Walter, E. T. Arena, and K. W. Eliceiri. Imagej2: Imagej for the next generation of scientific image data. *BMC Bioinformatics*, 18(1):529, Nov 2017.

[206] H. Y. Zhang, S. H. Zhang, M. Cheng, and Z. X. Li. Deformation characteristics of δ phase in the delta-processed Inconel 718 alloy. *Materials Characterization*, 61(1):49–53, 2010.

[207] G. Sharma, R.V. Ramanujan, and G.P. Tiwari. Instability mechanisms in lamellar microstructures. *Acta Materialia*, 48(4):875–889, 2000. cited By 124.

[208] Y. L. Tian and R. W. Kraft. Mechanisms of pearlite spheroidization. *Metallurgical Transactions A*, 18(8):1403–1414, Aug 1987.

[209] M. Jackson, R. J. Dashwood, L. Christodoulou, and H. M. Flower. Isothermal subtransus forging of ti–6al–2sn–4zr–6mo. *Journal of Light Metals*, 2(3):185 – 195, 2002. Modelling of Light Metals.